Large-scale and Microphysical Controls on Water Isotopes in the Atmosphere

by

Robert D. Field

A thesis submitted in conformity with the requirements
for the degree of Doctor of Philosophy

Graduate Department of Physics
University of Toronto

Large-scale and Microphysical Controls on Water Isotopes in the Atmosphere

Robert D. Field

Doctor of Philosophy

Graduate Department of Physics
University of Toronto

2010

Abstract

The isotopic composition of water in the atmosphere is influenced by how the water evaporated, how it was transported, and how it formed in the cloud before falling. Because these processes are temperature dependent, the isotopic ratios stored in glacial ice and other proxy sources have been used as an indicator of pre-instrumental climate. There is uncertainty, however, as to whether isotopic ratios should be interpreted as a proxy of local temperature, or as a broader indicator of changes in how the vapor was transported. To better understand these processes, the NASA GISS general circulation model (GCM) was used to examine two different types of controls on the isotopic composition of moisture.

The first control was the large-scale circulation of the atmosphere. Over Europe, it was found that $\delta^{18}O$ is strongly controlled by a Northern Annular Mode-like pattern, detected in both the GCM and for Europe's high-quality precipitation $\delta^{18}O$ data. Over the southwest Yukon, it was found that higher $\delta^{18}O$ was associated with moisture transport from the south, which led to a re-interpretation of the large mid-19th century $\delta^{18}O$ shift seen in the ice cores from Mt. Logan.

The second type of control was microphysical, relating to the way precipitation interacts with vapor after it has formed. Using a GCM sensitivity experiment, the effects of 'post-condensation

exchange' were found to depend primarily on the proportion between the amount of upstream precipitation that fell as rain and the amount that fell as snow, and at low latitudes, on the strength of atmospheric moisture recycling. This led to a partitioning of the well-observed correlation between temperature and precipitation $\delta^{18}O$ into its initial and post-condensation components, and a GCM-based interpretation of satellite measurements of the isotopic composition of water vapor in the troposphere.

Acknowledgements

This work was supported by the Canadian Foundation for Climate and Atmospheric Sciences through the Polar Climate Stability Network, and by a graduate scholarship from the Natural Sciences and Engineering Research Council of Canada.

I am grateful to my supervisor Dylan Jones for many things, but for his optimism most of all. Ted Shepherd provided helpful guidance towards the end of my program, and I thank Kaley Walker, Dick Peltier, Paul Kushner and Tom Edwards for their support and critical assessment of my work. Ana Sousa and Krystyna Biel routinely made life easier over the past five years.

Thanks go to Kent Moore for initiating this research and for providing me with the opportunity to do field work in the Yukon, an incredible experience. I greatly enjoyed my time there with Gerald Holdsworth, who also kept me safe. In that regard, I am also grateful to the pilots, staff and guides at the Kluane Lakes Research Station.

I also thank Shunli Zhang, Heather Andres and John Worden for helpful comments on different sections of the dissertation, Joe Galewsky and Derek Brown for generously providing data, Gavin Schmidt, Allegra LeGrande and Sophie Lewis provided modeling guidance, and Guido van der Werf and Sam Shen for their enthusiasm during various diversions.

I am grateful to my parents for supporting me in whatever I wanted to do, to my sister for making me always question my assumptions, and to Norah and William for providing me with so much happiness.

Table of Contents

List of Tables

List of Figures

Chapter 1
Introduction

1.1 Motivation

The first systematic measurements of oxygen isotope ratios in freshwater were made by *Friedman* [1953] and *Dansgaard* [1954]. Even from sources as varied as stream water and tap water, basic geographic differences could be seen in the measurements, such as the isotopic depletion in high-latitude and monsoonal climates relative to warm Mediterranean climates. To interpret the measurements, *Dansgaard* [1954] also identified the evaporative and moisture transport processes that control the isotopic composition of precipitation. The subsequent global-scale analysis of *Craig* [1961] emphasized the strong linear relationship between the hydrogen and oxygen isotopic compositions of precipitation at different locations across the globe.

It was from these analyses that terrestrial isotope paleoclimatology grew. The best-known proxy sources are ice cores from Greenland and Antarctica, which were first extracted in the late 1960s and early 1970s [*Dansgaard et al.*, 1969; *Johnsen et al.*, 1972], with the longest core from Antarctica now providing an 800-kyr climate record over eight glacial cycles [*Jouzel et al.*, 2007]. The isotopic composition of water in the ice cores provides a primary means of temperature reconstruction, with continually improving temporal resolution. At millennial timescales, recent emphasis has been placed on understanding the rapid Greenland warming during Dansgaard-Oeschger events coincident with the onset of slow cooling in Antarctica [*Blunier and Brook*, 2001; *EPICA*, 2006]. Ice cores have also been extracted at low latitudes from the Andes [*Thompson et al.*, 1984] and the Tibetan Plateau [*Thompson et al.*, 1989]. In Canada, ice cores have been taken from the eastern Arctic on the Devon ice cap on Devon island [*Paterson et al.*, 1977] and in western Canada, from Mt. Logan [*Holdsworth et al.*, 1992; *Moore et al.*, 2002; *Fisher et al.*, 2004; *Rupper et al.*, 2004].

Ice cores are the best known isotopic archives, but there are many other natural terrestrial archives that are useful for paleoclimatic reconstruction. Tree-ring cellulose was first used as a natural isotopic archive in the 1970s [*Epstein and Yapp*, 1976; *Gray and Thompson*, 1976; *DeNiro and Epstein*, 1979], and has since been used for mid-latitude climate reconstructions for the late Holocene [*McCarroll and Loader*, 2004], showing, for example, the wet 20th-century conditions over South Asia relative to the last millennium [*Treydte et al.*, 2006]. The oxygen isotope ratios in calcite deposits in cave formations were first used as an isotopic archive by *Hendy and Wilson* [1968], and are still widely collected [*McDermott*, 2004]. These provide an important long-term terrestrial climate proxy in non-glaciated regions (eg. *Wang et al.* [2001]). With continual improvements in sampling resolution, there is also growing potential for annual and sub-annual reconstructions of climate over shorter timescales [*Mattey et al.*, 2008]. These records, together with those from ice cores having high accumulation rates, offer significant opportunity for high-resolution, late Holocene reconstructions of climate, particularly for more regional, non-local phenomena [*Jones et al.*, 2009].

For all terrestrial sources, the isotopic composition of precipitation strongly influences that of the isotopic archive. As such, a central topic of isotope paleoclimatology has been to identify controls on the isotopic composition of precipitation. To first order, and over longer time-scales in particular, variability in precipitation isotopes has been interpreted as a temperature proxy, explained physically by Rayleigh distillation processes discussed in Section 1.4. There remains considerable uncertainty, however, surrounding the extent to which this distillation is controlled by the atmospheric circulation [*Hoffmann et al.*, 2006] and influenced by moisture recycling [*Gat*, 2000]. Stable water isotopes are also recognized as having considerable potential as a general diagnostic of moist processes in the atmosphere, although such application remains in its infancy [*Sherwood et al.*, 2010].

The goal of my PhD research was to better understand controls on the stable isotopes of water using an atmospheric general circulation model, focusing on the influence of the atmospheric circulation and one specific microphysical process, namely, post-condensation exchange between condensate and vapor. This chapter provides an overview of isotopic definitions, fractionation processes, simple analytical models of

isotopic depletion, numerical climate models, and the specific objectives of the dissertation.

1.2 Stable water isotopes in the hydrological cycle

There are two stable isotopes of hydrogen (^{1}H and ^{2}H, or D) and three stable isotopes of oxygen (^{16}O, ^{17}O, ^{18}O) that exist naturally, with the lightest isotope of each element being the most abundant. Molecules composed of different combinations of isotopes are called isotopologues. Of the nine possible isotopologues of water, $H_2{}^{16}O$ is the most common (99.73098%), with $HD^{16}O$ and $H_2{}^{18}O$ existing in much smaller, but still measurable quantities (0.199978% and 0.031460%, respectively) [*Sharp*, 2007]. Following convention in the geophysical literature, the term isotope is used in place of isotopologue throughout this work.

Isotopic quantities are expressed as a ratio R of concentrations of the heavy, rare isotope to the abundant, light isotope. Global average isotopic ratios for the two main rare isotopes are D/H = 155.95 x 10^{-6} and $^{18}O/^{16}O$ = 2005.2 x 10^{-6}, respectively [*Araguas-Araguas et al.*, 2000]. The stable isotope composition of water is now measured against the International Atomic Energy Agency's (IAEA) Vienna Standard Mean Ocean Water (VSMOW), which is in fact based on freshwater, and expressed as the normalized difference between the measured and VSMOW ratios using δ-notation in units of permil (‰). The oxygen isotope composition of a sample, for example, is expressed as:

$$\delta^{18}O = \left(\frac{R_{SAMP} - R_{VSMOW}}{R_{VSMOW}} \right) \times 10^{3} \qquad \textbf{(1-1).}$$

Samples with lower, more negative $\delta^{18}O$ or δD values have fewer of the heavy isotopes, and are referred to as being more "depleted". Occasionally, samples with higher, less negative $\delta^{18}O$ values are referred to as being more "enriched", although the term "less depleted" is usually more appropriate.

The systematic collection of $\delta^{18}O$ and δD data in precipitation began in the early 1960s under the IAEA's Global Network of Isotopes in Precipitation (GNIP) programme,

described in Chapter 2. Mean seasonal precipitation $\delta^{18}O$ values are shown in Figure 1-1 for GNIP stations having at least five years of data. Several well-known features of the global $\delta^{18}O$ distribution can be seen immediately, which were surveyed regionally by *Rozanski et al.* [1993]. There is a poleward tendency towards lower $\delta^{18}O$, down to -30 ‰ on the coasts of Antarctica and Greenland during their respective winters. There are also continental gradients over Eurasia and North America, with lower values farther inland. Over Europe, the predominant westerly flow from the Atlantic Ocean results in a more unidirectional, eastward decrease in $\delta^{18}O$ compared to North America, with its more variable moisture source regions. These gradients are reduced during the summer, owing to the contribution of moisture recycling by vegetation. Such continental gradients can also be seen at low latitudes, for example in South America, where, even under tropical conditions, there are lower values moving from the northeast coast on the Atlantic inland to southwest, but where the effects of land-surface moisture recycling are even more pronounced.

1.3 Evaporation, condensation and isotopic fractionation

Much of the observed precipitation $\delta^{18}O$ distribution in Figure 1-1 can be explained by the differences in how the light and heavy isotopes of water evaporate and condense, and how these differences manifest themselves during the transport of moisture. Thorough reviews of the these processes are provided by *Clark and Fritz* [1997], *Mook* [2001], *Faure and Mensing* [2005], *Sharp* [2007] and *Horita et al.* [2008].

Molecules within a liquid or vapor will have a distribution of speeds, and therefore of kinetic energies. In a liquid, molecules having sufficient kinetic energy will break through the surface tension of the liquid, moving across the liquid's boundary layer into the free air, constituting evaporation. Molecules in a gas will also have a distribution of kinetic energies, and those with lower kinetic energy will get trapped by the surface tension of liquid, constituting condensation. In a closed system with constant temperature, dynamic equilibrium is reached when the rate of evaporation from the liquid equals the rate of condensation from the vapor. In an open system, net evaporation occurs when the rate of condensation from the vapor is exceeded by the evaporation rate from

the reservoir, for example from an open jar in a room with unsaturated air, or when an unsaturated air mass is advected over a body of open water.

Evaporation and condensation are mass-dependent processes, which influences how different isotopes of a substance change phase. In a liquid, water molecules with heavy oxygen or hydrogen isotopes will have greater binding energies and lower diffusive velocities, which causes them to evaporate less readily. As a result, when evaporation takes place, the resulting vapor has fewer, by proportion, of the heavy isotopes than the reservoir and a lower isotopic ratio R_v. Conversely, the isotopic ratio R_l of the reservoir will increase due to the preferential escape of the light isotopes. At short time-scales, the increase in the liquid is not significant for large reservoirs such as the ocean, but can be significant for smaller lakes [*Sharp*, 2007]. Similarly, when net condensation occurs from a vapor reservoir, there is a preferential transfer of the heavy isotope to the condensate, resulting in fewer of the heavy isotopes in the vapor and more of the heavy isotopes in the condensate.

This separation of the different isotopes during a phase change is called isotopic fractionation. The extent of fractionation that takes place during evaporation from liquid to vapor is expressed as the fractionation factor α_v^l

$$\alpha_v^l = \frac{R_l}{R_v} \qquad \textbf{(1-2)}$$

where R_l is the isotopic ratio of the liquid, and R_v the isotopic ratio of the vapor in equilibrium with the liquid. Under equilibrium conditions, the fractionation factor for vapor condensing to liquid is simply the inverse of that for liquid to vapor:

$$\alpha_l^v = \frac{1}{\alpha_v^l} \qquad \textbf{(1-3).}$$

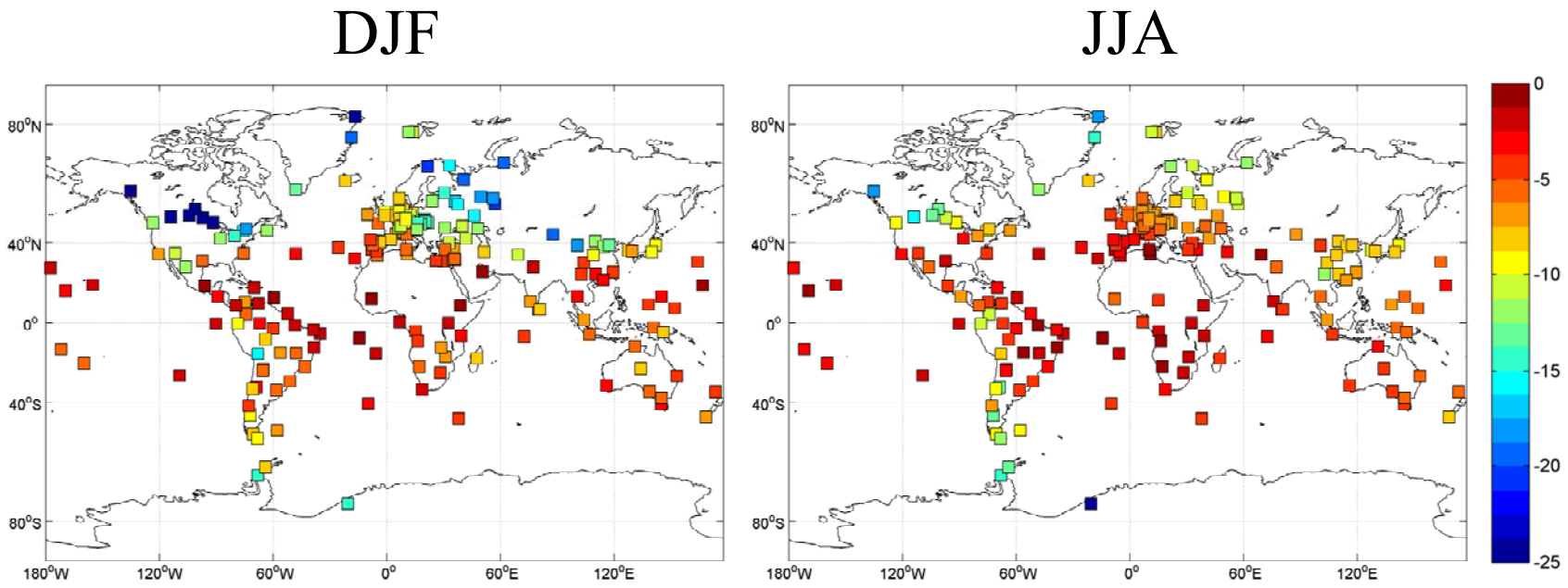

Figure 1-1. Seasonal precipitation $\delta^{18}O$ (‰) for all GNIP stations with at least five years of data. Seasonal $\delta^{18}O$ means have been arithmetically-weighted by precipitation amount.

In practice, fractionation factors are determined empirically from experiment and are temperature dependent, with fractionation decreasing as temperature increases Stemming from the seminal work of Craig and Gordon's [*Craig and Gordon*, 1965], adjustments to the equilibrium fractionation factors can be made for non-equilibrium conditions, namely the evaporation of ocean water into unsaturated air [*Merlivat and Jouzel*, 1979] or the deposition of vapor to ice in supersaturated conditions [*Jouzel and Merlivat*, 1984]. Further details of all isotopic fractionation processes are discussed in Chapter 2. The Rayleigh model of isotopic distillation

Based on ideas presented a decade earlier, *Dansgaard* [1964] developed the first model of isotopic composition of atmospheric moisture in terms of the progressive loss of heavy isotopes through fractionation, as water is lost to condensation. Along the path of an idealized, precipitating air parcel, the ratio R_r of heavy to light isotope in the vapor reservoir is described by

$$R_r = R_o f^{(\alpha-1)} \qquad \textbf{(1-4)}$$

where R_o is the initial isotopic ratio of the vapor, f is the fraction of original vapor remaining, and α is the fractionation factor between phases [*Gat*, 1996; *Mook*, 2001].

Equation (1-4 is referred to as the Rayleigh distillation model of isotopic evolution, and is the most important concept in isotope hydrometeorology. It can be derived by considering a vapor reservoir that loses mass with the preferential removal of the heavy isotope. Following *Mook* [2001], consider a reservoir with isotopic composition R_r

$$R_r = \frac{q_i}{q} \qquad \textbf{(1-5)}$$

where q_i is the abundance of the heavy isotope species ($H_2{}^{18}O$ or HDO), and q is the abundance of the light isotope ($H_2{}^{16}O$). Assuming $q >> q_i$, the contribution of q_i to the total reservoir mass can be neglected. If small quantities dq_i of the heavy isotope and dq of the light isotope are removed, the isotopic composition of this condensate is given by

$$R_c = \frac{dq_i}{dq} \tag{1-6}$$

subject to the fractionation

$$\alpha = \frac{R_c}{R_r} \tag{1-7}$$

where α is known.

Beginning with an initial isotopic composition R_0 and moisture content q_0, we wish to know the isotopic composition R_r of the reservoir when a fraction q/q_0 of the original moisture remains. The change in isotopic composition dR_r of the reservoir as moisture dq is lost is given by

$$\frac{dR_r}{dq} = \frac{d\left(\frac{q_i}{q}\right)}{dq} = \frac{\frac{dq_i}{dq}q - \frac{dq}{dq}q_i}{q^2} = \frac{1}{q}\left(\alpha\frac{q_i}{q} - \frac{q_i}{q}\right) = \frac{R_r}{q}(\alpha - 1) \tag{1-8}$$

which can be expressed as the initial value problem:

$$\frac{dR_r}{R_r} = \frac{dq}{q}(\alpha - 1). \tag{1-9}$$

Integrating Eq. 1-9 from R_0 to R_r and q_0 to q gives:

$$\ln\left(\frac{R_r}{R_0}\right) = (\alpha - 1)\ln\left(\frac{q}{q_0}\right) \tag{1-10}$$

which is solved for R_r:

$$R_r = R_0\left(\frac{q}{q_0}\right)^{(\alpha-1)} = R_0 f^{(\alpha-1)} \tag{1-11}$$

where $f = \frac{q}{q_0}$ is the fraction of the initial moisture remaining.

Figure 1-2 shows the Rayleigh distillation of a cooling, precipitating moisture mass with an initial vapor composition of $\delta^{18}O$ = -10 ‰, typical of fresh evaporate from the ocean. When condensate forms as liquid from the vapor reservoir, there is a ~ 10 ‰ enrichment that occurs as a result of the heavy isotope condensing preferentially, indicated by the difference between the black (vapor) and grey (condensate) distillation curves. As rainout occurs with decreasing *f*, this preferential removal leads to a progressive depletion of heavy isotopes in the vapor and also the subsequent condensate forming from it. When the precipitation changes from rainfall to snow at $T = 0$ °C, the fractionation factor increases, resulting in a further offset between vapor and condensate. Over the remaining moisture loss from snowfall, one can see that the increase in fractionation factor results in more rapid depletion of the vapor reservoir and of subsequent condensate.

In interpreting modern isotopic observations with the Rayleigh model, a common approach is to initialize the vapor composition R_0 from the precipitation at the coastal boundary from which moisture over the continent is thought to originate, estimate the moisture loss from observed vapor fields across a continental gradient, and finally, estimate the isotopic composition of vapor and precipitation at a given measurement location. This technique has been applied, for example, in interpreting observations over Europe [*Sonntag and Schoch-Fischer*, 1985], Russia [*Kurita et al.*, 2004] and China [*Araguas-Araguas et al.*, 1998]. Extending this approach, *Salati et al.* [1979] and *Rozanski et al.* [1982] included an additional continental source from evapotranspiration over the Amazon and Europe, respectively. At their most sophisticated, Rayleigh models have been implemented in Lagrangian trajectory models driven by meteorological observations from atmospheric reanalyses, which allows one to identify mean transport pathways or atmospheric circulation features associated with enhanced isotopic depletion [*Helsen et al.*, 2004; *Helsen et al.*, 2007; *Sodemann et al.*, 2008].

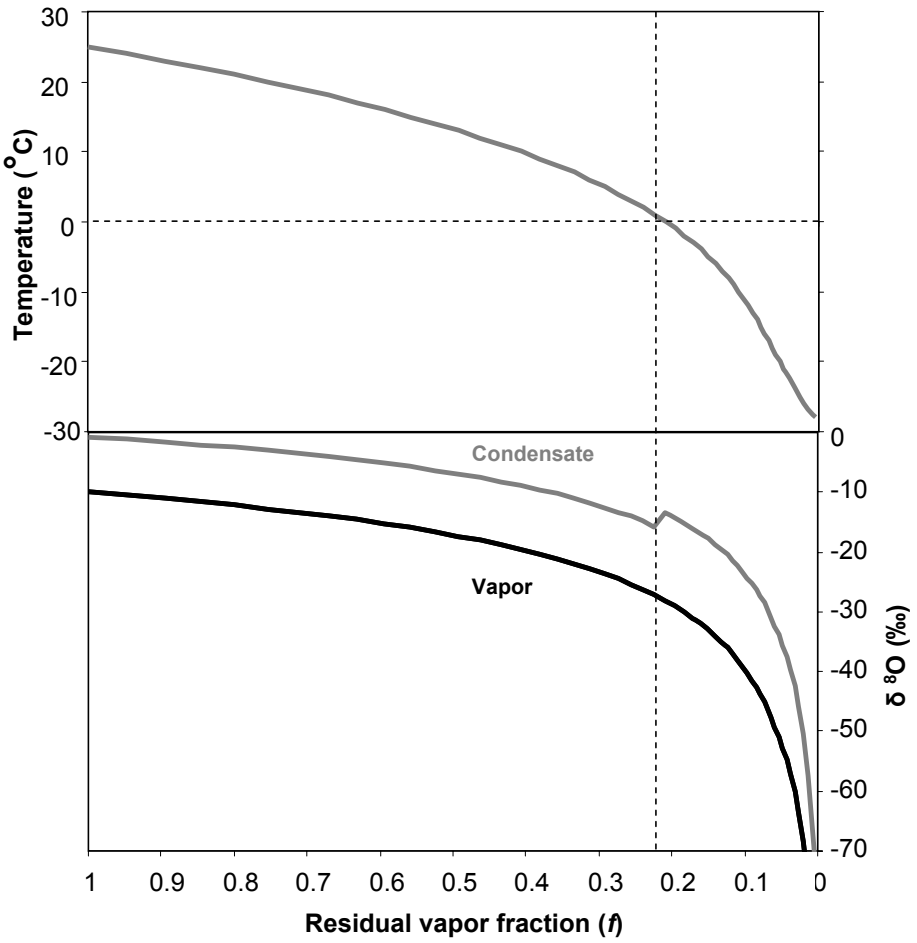

Figure 1-2. Isotopic composition of a precipitating air mass with vapor depleting according to the Rayleigh model of Eq. 1-4, with an initial vapor composition of -10 ‰ at T = 25 °C, following *Clark and Fritz* [1997].

The Rayleigh model also provides a physical basis for the isotopic 'temperature effect' [*Dansgaard*, 1964; *Sonntag and Schoch-Fischer*, 1985], the observed relationship between mean annual precipitation $\delta^{18}O$ and surface air temperature. Physically, precipitation $\delta^{18}O$ and temperature are positively associated primarily through the latter's control of the saturation vapor pressure of water, and hence the f-term in the Rayleigh model. The temperature effect was first described by *Dansgaard* [1964] in terms of the positive relationship between mean annual precipitation $\delta^{18}O$ and surface temperature at different locations. With the availability of two decades worth of data from the GNIP

network, *Rozanski et al.* [1992] were the first to examine the temperature effect in its temporal sense, by examining the relationship between monthly anomalies of precipitation $\delta^{18}O$ and surface air temperature for individual locations. Of the stations considered, positive correlations were found over Europe, where the observation network was most dense, and in Argentine Island off of the tip of South America at 65°S. Many studies have subsequently examined the temporal relationship between precipitation $\delta^{18}O$ and local temperature, along with other meteorological variables. Notably, *Kurita et al.* [2004] conducted a 5-year sampling across Russia, which filled a major spatial gap in the GNIP database, noted earlier by *Rozanski et al.* [1993]. Even for this short length of record, they found a strong T-$\delta^{18}O$ relationship across pooled observations, outside of the boreal summer.

One can see from Eq. 1-4 that the isotopic composition of precipitation reflects the entire history (via f) of an air mass, and not just condensation conditions over the precipitation site. While this complicates the use of $\delta^{18}O$ as a local temperature proxy, it also allows for the possibility of isotopic evidence for broader circulation signatures. The first examinations of circulation control on precipitation $\delta^{18}O$ focused on high-latitude regions, specifically over Greenland. *Barlow et al.* [1993] found that over central Greenland, higher δD was linked with the negative phase of the North Atlantic Oscillation (NAO), which is associated with warmer, more southerly moisture transport towards the ice core site, and therefore less isotopic distillation. This control was also identified by *Rogers et al.* [1998] and recently re-examined [*Vinther et al.*, 2003; *Sodemann et al.*, 2008].

Circulation controls on precipitation isotopes have also been examined at low latitudes. Over the Asian Monsoon region, numerous observational studies have identified a reverse isotopic seasonality, with lower precipitation $\delta^{18}O$ during the summer monsoon despite warmer temperatures [*Araguas-Araguas et al.*, 1998; *Johnson and Ingram*, 2004], which is attributed to the strength of the monsoon via enhanced Rayleigh distillation. As summarized by *Vimeux et al.* [2009], the Andean ice cores record El Niño-Southern Oscillation (ENSO) variability, with higher precipitation $\delta^{18}O$ associated with El Niño conditions, but through an indirect mechanism. El Niño conditions are associated with a

weaker South American Summer Monsoon, which results in weaker upstream convective rainout, and, consequently, the arrival of a less depleted vapor reservoir over the Andes.

1.4 Factors not accounted for in the Rayleigh model

Irrespective of their complexity, Rayleigh-based models assume the immediate removal of condensate once it has formed, locking in the isotopic composition of the cloud water [*Jouzel et al.*, 1997]. In reality, there will be post-condensation exchange as raindrops fall through layers below. Raindrops falling into unsaturated air will partially re-evaporate, enriching the raindrop, but depleting the surrounding vapor [*Dansgaard*, 1954; *Friedman et al.*, 1962; *Stewart*, 1975]. Re-evaporation is often invoked as a possible cause of disagreement between $\delta^{18}O$ observations and simple model predictions [*Brown et al.*, 2008; *Feng et al.*, 2009], or to explain uncertainty in a relationship between a climatic variable of interest and precipitation $\delta^{18}O$ [*Etien et al.*, 2008]. Also, droplet re-evaporation was suggested as a possible cause of higher precipitation $\delta^{18}O$ under low humidity conditions in mid-latitudes [*Araguas-Araguas et al.*, 1998; *Gat*, 2000; *Stern and Blisniuk*, 2002; *Danis et al.*, 2006]. Although the condensate will be enriched, the evaporated vapor will be depleted relative to the surrounding vapor [*Gedzelman and Arnold*, 1994]. As a result, subsequent rainfall from this air mass can be depleted, and can result in lower precipitation $\delta^{18}O$ [*Brown et al.*, 2008; *Risi et al.*, 2008].

Raindrops falling into saturated layers will tend to equilibrate isotopically with the surrounding vapor, which may be isotopically different than the vapor from which the raindrops originally formed [*Kavanaugh and Cuffey*, 2003]. This is especially the case over land during summer, when evapotranspiration from plants acts as a non-fractionated, relatively un-depleted moisture source compared to open water. *Gat* [2000] suggests, for example, that post-condensation exchange between precipitation and vapor, particularly from the land surface, may effectively erase the isotopic signature of the original condensate.

1.5 Isotopic tracers in numerical climate models

Simple Rayleigh distillation models are limited in their ability to explain precipitation $\delta^{18}O$ variability due to the absence of air mass mixing, post-condensation exchange, and evaporative recharge [*Hoffmann et al.*, 2000]. To better account for these processes, efforts have been made to equip general circulation models (GCMs) of the atmosphere with stable water isotope physics, recently reviewed by *Sturm et al.* [2010] and *Noone and Sturm* [2010]. A list of such GCMs is provided in Table 1-1.

Stable isotope tracers were first incorporated into the Laboratoire de Météorologie Dynamique (LMD) atmospheric GCM by *Joussaume et al.* [1984], who reproduced the main global geographic patterns observed in precipitation $\delta^{18}O$, and the 'spatial slope' relationship between precipitation $\delta^{18}O$ and surface temperature at different locations. This was followed by inclusion of isotopic tracers in the NASA Goddard Institute for Space Studies (GISS) II GCM by *Jouzel et al.'s* [1987]. Subsequently, the first forward-modeling studies of precipitation $\delta^{18}O$ under Last Glacial Maximum (LGM) conditions were conducted [*Joussaume and Jouzel*, 1993; *Jouzel et al.*, 1994], showing that simulated differences between modern and glacial climates agreed reasonably well with ice core data from Antarctica and Greenland. Using the GISS II GCM, but with the addition of moisture source tagging, *Charles et al.* [1994] showed that in addition to temperature, changes in atmospheric circulation could also induce an isotopic response. For Greenland, they found that the relative contribution of high $\delta^{18}O$ moisture from the Atlantic increased under LGM conditions, which offset the decrease in $\delta^{18}O$ due to colder temperatures. *Cole et al.* [1999] used the same model to identify the local temperature effect, identifying a positive correlation between surface air temperature and precipitation $\delta^{18}O$ anomalies over the extra-tropical continental interiors.

Table 1-1. Summary of numerical climate models equipped with stable water isotope tracers. Horizontal resolution is specified either in grid-point resolution (latitude × longitude) or spectral truncation (with approximate grid-point resolution). Biases discussed are all for annual mean precipitation $\delta^{18}O$.

Base model	Reference	Horizontal resolution	Vertical levels
LMD	*Joussaume et al.* [1984]	3.75° × 11.24°	11
GISS II	*Jouzel et al.* [1987]	8° × 10°	9
ECHAM3	*Hoffman et al.* [1998]	T42 (2.8° × 2.8°)	19
		T21 (5.6° × 5.6°)	
ECHAM4	*Werner et al.* [2001]	T30 (3.75 × 3.75)	19
Melbourne	*Noone and Simmonds* [2002]	3.25° × 5.625°	9
GENESIS	*Mathieu et al.* [2002]	T31 (3.75° ×3.75°)	18
GISS ModelE	*Schmidt et al.* [2005]	4° × 5°	20
MPI REMO	*Sturm et al.* [2005]	0.5° × 0.5°	19
ModelE-R	*Schmidt et al.* [2007]	4° × 5°	20
NCAR CAM2	*Lee et al.* [2007]	T42 (2.8° × 2.8°)	26
Scripps GSM	*Yoshimura et al.* [2008]	2.5 × 2.5	17
HadCM3	*Tindall et al.* [2009]	2.5° × 3.75°	19
LMDz	*Risi et al.* [2010]	2.5° × 3.75°	19

The next generation of isotopically-equipped GCMs consisted of the ECHAM-3 [*Hoffmann et al.*, 1998], ECHAM-4 [*Werner et al.*, 2001], GENESIS [*Mathieu et al.*, 2002], GISS ModelE [*Schmidt et al.*, 2005] and Melbourne University (MU) [*Noone and Simmonds*, 2002], all distinguished from previous GCMs by their more sophisticated cloud physics and generally higher resolution. With these higher-resolution models, there was also increased effort to better understand the influence of atmospheric circulation on

precipitation $\delta^{18}O$. One important application was to resolve the difference between Greenland LGM temperatures reconstructed from boreholes and from a classical, spatially-calibrated $\delta^{18}O$ thermometer, which indicated temperatures 10K warmer than from boreholes. Using ECHAM-4, *Werner et al.* [2000] found that a more zonal winter flow under LGM conditions reduced the relative contribution of winter precipitation over Greenland, leading to a 'warmer', more summer like signal in the ice core. Under modern conditions, *Werner and Heimann* [2002] also found that lower $\delta^{18}O$ values were associated with a positive NAO phase, consistent with the observational studies described in Section 1.4. These types of circulation controls have also been identified at lower latitudes using GCMs; signatures of the El Niño-Southern Oscillation (ENSO) were found over South America by *Vuille and Werner* [2005] and across the tropics by *Brown et al.* [2006] and *Tindall et al.* [2009], the influence of the strength of the Asian Monsoon on $\delta^{18}O$ values over the Tibetan Plateau was examined by *Vuille et al.* [2005b], and the Indian Ocean Zonal Mode over East Africa was identified by *Vuille et al.* [2005a].

Arguably, the most state-of-the art application of GCMs to paleo-proxy interpretation is the work of *LeGrande and Schmidt* [2009] using the GISS ModelE-R of *Schmidt et al.* [2007], the first fully coupled atmosphere-ocean to be equipped with stable isotope tracers. Previous comparisons of modeled precipitation isotopes between climatic states compared single time-slice runs between modern and paleo conditions, typically LGM. *LeGrande and Schmidt* [2009], conversely, conducted time-slice runs roughly every 1000 years apart from 9000 b.p. to present, showing good agreement with transient changes in Asian speleothem $\delta^{18}O$.

With incremental development of isotopically-equipped GCMs now spanning twenty-five years, it is instructive to see how model performance has changed over time, focusing on Greenland given its ubiquity in the literature. In the pioneering work of *Joussaume et al.* [1984], pronounced biases were present for Greenland, where a modeled January minimum of –22 ‰ for $\delta^{18}O$ was much greater than the observed winter minimum of -40 ‰. Using the GISS II GCM, *Jouzel et al.* [1987] found that modeled $\delta^{18}O$ at Summit 3 ‰ was too high over Greenland, but nevertheless was a considerable improvement, due, in part, to their examination of all months of the year. Given the similar resolution of GISS

II GCM and the LMD GCM of *Joussaume et al.* [1984], and in the similarities in isotopic parameterizations between models noted by *Jouzel et al.* [1987], the improvement was likely attributable to differences in the underlying physics of the two models.

Using ECHAM-3, *Hoffmann et al.* [1998] found that the modeled $\delta^{18}O$ was 8 ‰ too high for Greenland at a spectral resolution of T21 (approximately 5.6° × 5.6°), which was reduced to 2 ‰ for T42 (2.8° × 2.8°). Interestingly, *Werner et al.* [2002] found using ECHAM-4 that an intermediate T30 (3.75 × 3.75) resolution produced bias of 5 ‰, as might be expected with successive versions of the same GCM. This was also comparable to the results of *Mathieu et al.* [2002], who found a 4 ‰ bias with a similar resolution of T31 (3.75° ×3.75°). Using the HadCM3 model at 2.5° × 3.75° resolution, *Tindall et al.* [2009] found that positive biases over Greenland and Antarctica were no more than 3 ‰, but remained higher at other ice core sites with more complex topography not as well resolved by the GCM, namely the Andes and the St. Elias Mountains in Yukon and Alaska. Although no direct, quantitative comparison was provided over Greenland, S*chmidt et al.* [2005] showed that their small bias over Summit was not sensitive (typically less than 1 ‰) to different configurations of the GCM, ranging from the inclusion of a gravity-wave drag scheme to different surface fractionation schemes.

Based on the studies discussed above, it may be tempting to infer that the accuracy of modeled isotope values will be controlled primarily by model resolution, but the relatively high-resolution simulation (T42, 2.8° × 2.8°) of *Lee et al.* [2007] still produced a 5-10 ‰ bias over Greenland, and the 2.5° × 3.75° simulation with the LMDz model of *Risi et al.* [2010] had a ~10 ‰ bias. These two studies are interesting because they included more sophisticated schemes for the equilibration strength between falling condensate and the surrounding vapor (discussed in detail in Section 2.2.6 and Chapter 5) compared to previous models. In the case of *Risi et al.* [2010], the bias is comparable to the original, much lower resolution LMD version of *Joussaume et al.* [1984]. This illustrates the trade-off that arises in developing more sophisticated parameterizations for subgrid processes, isotopic or otherwise. Such development is necessary however. It is important to note that, as pointed out by *Sturm et al.* [2010], despite the variety of GCMs

which have been equipped with isotope tracers, their isotopic parameterizations are similar, and do not, in a sense, represent entirely independent models.

1.6 Dissertation goals

This dissertation had two main goals. The first was to examine circulation controls on precipitation $\delta^{18}O$ at mid-latitudes, for interpreting paleoisotopic archives and validating the GCM. The second was to better understand the effects of post-condensation exchange. The GISS ModelE GCM has been used for the work described here, the most important aspects of which are discussed in Section 2.2.

1.6.1 Circulation controls on $\delta^{18}O$ at mid-latitudes

Studies examining atmospheric circulation controls on precipitation $\delta^{18}O$ have focused on either high- or low-latitudes, with little consideration of the mid-latitudes. The few studies on the mid-latitude have been exclusively observational, such as that of *Baldini et al.* [2008], which analyzed NAO controls over European precipitation $\delta^{18}O$, or that of *Birks and Edwards* [2009], which probed the influence of the Pacific North America pattern (PNA) over precipitation $\delta^{18}O$ in western Canada. The analysis of circulation controls using GCMs at mid-latitudes remains to be done, particularly given the increasing availability of non-ice core isotopic archives with high temporal resolution, such as speleothems and tree-ring cellulose $\delta^{18}O$. Successful modeling of present-day controls is the first step towards more mechanistic attribution of isotopic variability to different causes.

To this end, Chapter 3 of this dissertation was an examination of atmospheric circulation controls on precipitation $\delta^{18}O$ over Europe. Europe has what is likely the world's most active speleothem and tree-ring isotope research communities, such as the European Union's ISONET network and Millennium projects (K. Treydte, pers. comm.). An improved understanding of controls on precipitation $\delta^{18}O$ over Europe contributes to interpretation of these new isotopic archives. Europe also has the world's most dense and longest running network of precipitation isotope collection sites under GNIP: Figure 1-3 shows that of the 56 GNIP stations worldwide having at least 20 years of data, 27 are in Europe. The GNIP station density of Europe therefore provides the best possible means

with which to validate the mid-latitude atmospheric circulation controls on precipitation $\delta^{18}O$ identified in a GCM. The material from this chapter is published in *Field* [*Field*].

The comparison in Chapter 3 of controls over European precipitation $\delta^{18}O$ between observations and the GCM served to assess the accuracy of the latter. Having shown that controls identified in the GCM over Europe are realistic, Chapter 4 is an application of the GISS ModelE GCM to better understand controls on precipitation $\delta^{18}O$ over the Southwest Yukon. This region is at a higher latitude than the European domain, but is also at the end of a major oceanic storm track, and would presumably have similar isotopic controls. Of particular interest are the $\delta^{18}O$ records from the Mt. Logan ice cores.

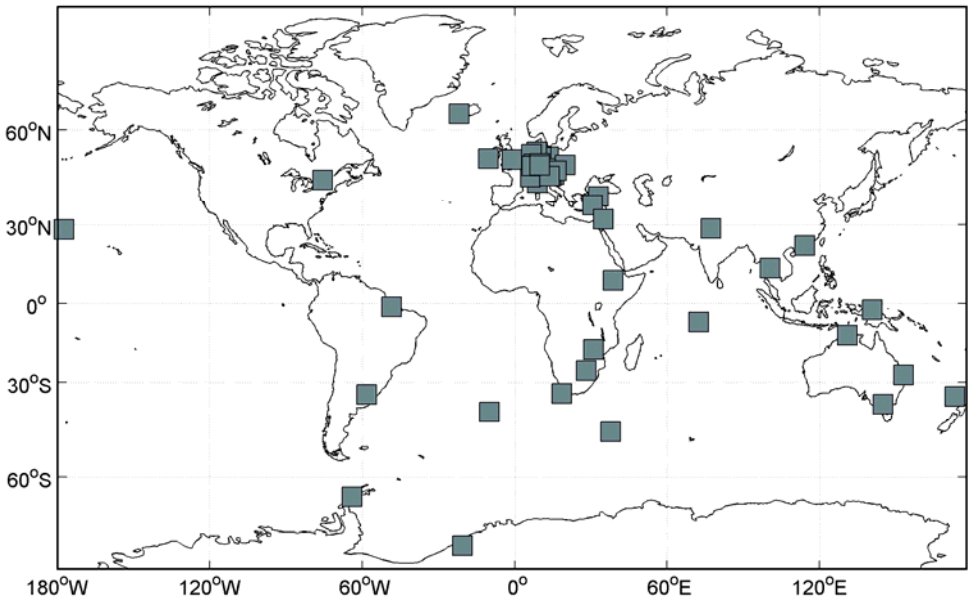

Figure 1-3. GNIP stations with at least 20 years of data.

The snow accumulation record from the Northwest (NW) Col ice core [*Holdsworth et al.*, 1992] has been used in reconstructions of past variability in the Pacific-North America (PNA) pattern [*Moore et al.*, 2002], and high snow accumulation years are associated with more southerly moisture transport [*Rupper et al.*, 2004]. The $\delta^{18}O$ record from the ice core is also thought to be controlled primarily by changes in atmospheric circulation. With the addition of a second ice core at the same elevation, *Fisher et al.* [2004] interpreted a large mid-19th century shift towards lower $\delta^{18}O$ as indicating a more

southerly moisture source. Using an analytical model with prescribed zonal and meridional moisture source contributions, they proposed that lower $\delta^{18}O$ was associated with a deeper Aleutian Low (AL) pressure system and more southerly moisture transport. Owing to the greater moisture transport distance, a deeper AL would result in enhanced isotopic depletion.

Although possible, any $\delta^{18}O$ drop caused by such a shift might be offset by warmer source evaporation conditions and air mass pathways, both of which would be associated with higher precipitation $\delta^{18}O$. Furthermore, there is recent, independent proxy evidence suggesting an opposite shift in circulation. *D'Arrigo et al.* [2005] used tree-ring data from the Pacific Northwest, the Yukon, Alaska and Siberia to reconstruct the North Pacific Index (NPI) of *Trenberth and Hurrell* [1994]. Their analysis showed an 1850 increase in the NPI, that is associated with a weaker AL, a switch opposite in direction to the hypothesis of *Fisher et al.* Chapter 4 describes a GCM-analysis to better understand if there are significant atmospheric controls on precipitation $\delta^{18}O$ in this region. This chapter is published in *Field et al.* [2010].

1.6.2 The effects of post-condensation exchange

The contribution of post-condensation exchange to precipitation $\delta^{18}O$ variability is universally acknowledged as being important, but has not been quantified. It is still not known at a global scale, for example, whether exchange between falling condensate and ambient vapor tends to enrich or deplete precipitation, or how post-condensation exchange affects climatic controls on precipitation $\delta^{18}O$. In GCM studies, the modeled temperature effect is attributed in a general sense to Rayleigh distillation [*Hoffmann et al.*, 1998], but, beyond that, little mechanistic understanding of this process is described, including possible contributions from post-condensation exchange.

Indeed, as *Helsen et al.* [2007] and *Masson-Delmotte* [2008] stated, an inherent disadvantage of isotopically-equipped GCMs is that their complexity makes it difficult to isolate different fractionation processes. This is partly true, but it could be argued that this reflects the way in which these GCMs have been used. The predominant approach in GCM studies is to conduct a control simulation and identify any relationships between

the modeled isotopes and a meteorological variable of interest. This approach is very useful, and forms the basis for Chapters 3 and 4 of the dissertation. In terms of understanding mechanistic controls on the isotopic composition of moisture, however, it is not experimental in the sense of systematically controlling different processes. Even at their most sophisticated (e.g. *Lee et al.* [2007]), a control identified through diagnosis of a control simulation could be confounded with a more direct, underlying physical control. It could be argued that the only way of determining the importance of a given process or meteorological control is to run the model with its influence removed. *Wright et al.* [2009], in contrast to previous studies, did take this experimental approach, conducting sensitivity analyses with certain microphysical processes disabled, to determine the influence of post-condensation exchange on the isotopic composition of vapor δD. Chapter 5 of the dissertation is a GCM-based analysis of post-condensation exchange on precipitation and vapor isotopes, following the approach of *Wright et al.* [2009]. A key motivation for this work was the improved interpretation of new satellite-based measurements of vapor isotopes in the troposphere [*Worden et al.*, 2007; *Brown et al.*, 2008; *Frankenberg et al.*, 2009]. This chapter has been accepted for publication in the Journal of Geophysical Research - Atmospheres as *Field et al.* [in press].

Chapter 2
Data and model description

2.1 Data

2.1.1 The Global Network of Isotopes in Precipitation

The Global Network of Isotopes in Precipitation (GNIP) was initiated in 1958 by the International Atomic Energy Agency (IAEA) in cooperation with the World Meteorological Organization (WMO), and became operational in 1961 [*Aggarwal et al.*, 2005]. The initiation of GNIP was originally motivated by the potential for using radioactive tritium (^{3}H) as an environmental tracer following its excess supply produced during atomic weapons testing. Subsequently, the systematic collection of the stable isotopes of water was also recognized as being valuable for water resource management, and for the interpretation of paleo-isotopic proxies.

The original GNIP was composed of 151 stations, growing to 220 in 1964, followed by a steady decline through the 1970s, and a resurgence in the 1980s.. Most GNIP stations are run in conjunction with WMO-level meteorological stations. The majority of data in the GNIP database consists of monthly averages of ^{3}H, D and ^{18}O concentrations in precipitation, with limited event-based precipitation and vapor isotope data. Records also include precipitation amount, surface air temperature, and humidity. The majority of stations in the current GNIP database have between four and eight years worth of data.

Initially, isotopic samples from across the network were analyzed at a small number of laboratories in the US and at the University of Copenhagen. Currently, 30-40% of samples are analyzed at the IAEA's Hydrology Section, with the remainder analyzed at laboratories in contributing countries. Data analyzed at contributing countries are

submitted to the IAEA and distributed through the Water Isotope System for Data Analysis, Visualization, and Electronic Retrieval (WISER)[1].

Sampling procedures are reviewed in *Mook* [2001] and *IAEA* [2006]. Precipitation is sampled directly from the rain gauges at the meteorological stations. It is collected in large (5 L) sealed collection containers, from which a 50 mL sample is taken at the end of each month for analysis. The most important factor during sampling is that precipitation from the gauge is transferred immediately to the collection containers and sealed to prevent evaporation, which will lead to an enrichment bias in the precipitation sample. It is also important that at the end of each month collection and sampling containers are cleaned and dried to prevent isotopic contamination from month to month. Glass bottles are ideal, but for samples that require transport to other laboratories, high-density polyethylene containers are sufficient to prevent evaporative enrichment or exchange.

The isotopic composition of the samples is primarily determined using mass spectrometry. Water samples are not analyzed directly in the mass spectrometer due to the adhesion of water to the metal, which contaminates the analysis. For ^{18}O analysis, the sample is equilibrated with CO_2. A portion of the equilibrated CO_2 is then transferred to the mass spectrometer, ionized, and accelerated through a magnetic field. The isotopically different ions will have circular paths with different radii. Because the ions have the same charge, the difference in radii is attributable solely to the difference in mass between ions. Ion collectors at different radii measure the abundance of isotopically distinct ions, and hence the isotopic composition of the sample.

Long-term precision of samples at the IAEA is ± 0.1 ‰ for $\delta^{18}O$ and ± 1 ‰ for δD [*IAEA*, 2006]. Contributing laboratories are responsible for the accuracy of their measurements, but intercomparisons between laboratories are conducted regularly to ensure consistency of measurements. A thorough quality-control analysis of the GNIP database was conducted in 1992, including the removal of records where errors in

[1] http://www-naweb.iaea.org/napc/ih/IHS_resources_isohis.html

collection procedures were suspected. Currently, records are regularly examined for consistency and screened for errors [*IAEA*, 2006].

2.1.2 Tropospheric Emission Spectrometer

To date, most observational isotope studies have focused on precipitation, owing to its availability through the GNIP and its well-established measurement procedures. The GNIP database contains vapor isotope data for only a small number of locations, however, and upper-air vapor isotope data is limited to short-term and geographically-limited aircraft campaigns [*Ehhalt and Heidt*, 1974; *Rozanski and Sonntag*, 1982; *Gedzelman et al.*, 2003]. Space-based techniques for measuring vapor isotopes were first developed for the upper-troposphere and lower-stratosphere (UTLS), proving useful in characterizing the water composition and exchange pathways in that region [*Kuang et al.*, 2003; *Nassar et al.*, 2007; *Steinwagner et al.*, 2007].

A major step was made recently with the development of HDO retrievals from the Tropospheric Emission Spectrometer (TES) [*Worden et al.*, 2006; *Worden et al.*, 2007], which represented the first satellite-based measurements of vapor isotopes throughout the depth of the free troposphere. A preliminary comparison between the GCM and selected TES measurements is performed in Chapter 5. The TES instrument is a Fourier transform spectrometer measuring infrared emissions over the range 650-3050 cm^{-1} [*Beer et al.*, 2001; *Worden et al.*, 2006]. It was launched on board the Aura spacecraft in July 2004 and is in a sun-synchronous orbit with a 16-day repeating orbit track. The TES instrument has a 5.3 x 8.4 km horizontal footprint at nadir, upon which HDO analyses to-date have been based.

The TES HDO retrieval is based on lines in the 1150-1350 cm^{-1} range, and has peak sensitivity at 700 hPa, with a precision of 1% to 2%, which decreases at higher latitudes [*Worden et al.*, 2006]. The TES retrievals are performed using an optimal estimation approach [*Rodgers*, 2000]. Given an estimate of the actual HDO profile, a forward radiative transfer model can be used to generate the radiances as would be observed by the instrument. In the TES retrieval, the actual atmospheric state is estimated such that the difference between the radiances observed by TES and modeled radiance is

minimized according to a least squares criteria. In the retrieval, a priori information is provided by isotope fields generated by a version of the NCAR CAM equipped with isotopic tracers using the approach of *Noone and Simmonds* [2002]. Due to a systematic bias in line strength, a -5% correction is applied to the HDO concentrations, which results in an additional δD depletion of ~40-50 ‰. The TES HDO estimates are now being used to characterize tropospheric hydrology, including rainfall evaporation rates and moisture attribution between land and ocean sources [*Worden et al.*, 2007], upstream moisture recycling [*Brown et al.*, 2008], and long-range transport in the upper troposphere [*Liu et al.*, 2009]. ExampleδD fields are shown in Figure 2-1, which shows the basic southward migration of higher δD during the boreal winter.

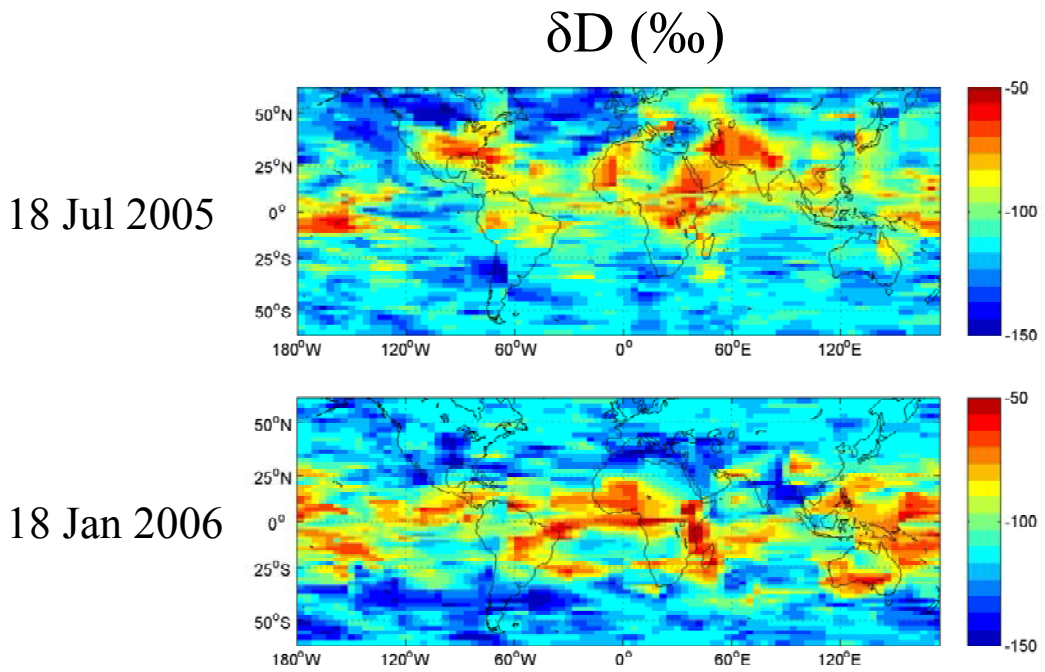

Figure 2-1. TES δD estimates at 825 hPa for 18 July 2005 and 18 Jan 2006. These are from the Version 003 product, and have been spatially-interpolated.

2.2 Stable isotope tracers in GISS ModelE

2.2.1 Overview of ModelE cloud physics

Isotopic processes in ModelE are computed in parallel to the model's core moist processes, and are therefore sensitive to their parameterization, which is reviewed in

Schmidt et al. [2005]. A brief summary of ModelE's cloud parameterization is provided in this section to better understand implementation of the isotopic tracers, and, in particular, the post-condensation exchange study in Chapter 5.

In ModelE, convective and stratiform cloud processes are modeled separately, but with moisture exchange between the two. The convective scheme is described by *Del Genio and Yao* [1993]. Convection occurs when a parcel at a given level is buoyant relative to the layer above, with respect to a moist static energy criteria. At each level, there are two updrafting plumes: one that remains undiluted, which is meant to represent the core of a convective cell, and one that entrains environmental air. The amount of vertical mass flux is determined iteratively such that neutral buoyancy at the cloud base is achieved, rather than an assumed 50% of mass, as was the case in the earlier Model II [*Hansen et al.*, 1983].

At each level after lifting and cooling, any excess moisture with respect to saturation vapor pressure is condensed out of the vapor reservoir. In convective clouds, a fraction of this condensate falls as precipitation, and a fraction is detrained into the large-scale condensate reservoir, based on a separation of the condensate mass according to an assumed Marshall-Palmer droplet size distribution and a critical droplet diameter above which the droplet will fall out. Further details on this partitioning can be found in *Del Genio et al.* [2005]. The convective scheme also includes explicit parameterization of downdrafting plumes. Downdrafting is driven by mid-tropospheric entrainment of dry and cool environmental air into the convective column, with condensate evaporation into the unsaturated air causing further cooling. In ModelE, downdrafts are produced for parcels rising more than one model level, at the first level for which an equal mixture of plume and environmental air is negatively buoyant. The plume descends until neutral buoyancy is achieved through warming. The downdrafts are assumed to have one third of the mass of the combined mass flux of the updrafting plumes.

Large-scale clouds are modeled using the approach of *Sundqvist* [1978], where condensation is driven by moisture convergence above a tunable relative humidity threshold. Cells are divided into a clear and cloudy fraction, and presumed subgrid-scale

mixing between the two reservoirs can result in condensate evaporation. Given the uncertainty in the proportion of cloud areal fraction, downdrafting mass, and simplifications inherent in representing droplet-size distributions, the condensate evaporation rate is not well constrained [*Del Genio et al.*, 1996], which is an ongoing issue in cloud physics parameterizations in general (e.g. *Bacmeister et al.* [2006]; *Maloney* [2009]; *Misra* [2009]).

The isotopic tracers follow all moist cloud processes. The light $H_2{}^{16}O$ tracer follows the prognostic water exactly. The heavy $H_2{}^{18}O$ and HDO tracers also follow the prognostic water, but subject to fractionation processes, primarily during phase changes. The isotopic parameterizations in ModelE are based on experimentally-obtained fractionation factors, and reflect the evolution of isotopically-equipped GCMs in earlier versions of the NASA GCM Model II [*Jouzel et al.*, 1987] and also the MPI-Hamburg ECHAM4 [*Hoffmann et al.*, 1998].

In the following sections, a description of ModelE's isotopic processes is given that is meant to be applicable across different cloud parameterizations.

2.2.2 Equilibrium fractionation

Common to many fractionation processes in ModelE, at the surface and in the cloud, are the equilibrium fractionation factors between liquid and vapor and between solid and vapor. *Majoube* [1971a; b] provided what are still standard equilibrium fractionation curves for phase changes between liquid and vapor and between solid and vapor. For $H_2{}^{18}O$, the equilibrium fractionation factor α_v^l between vapor and liquid is given by

$$\ln \alpha_v^l = 1.137 \times 10^3 / T^2 - 0.4156 / T - 2.20667 \times 10^{-3} \qquad \textbf{(2-1)}$$

and between vapor and ice by

$$\ln \alpha_v^s = 11.839 / T - 0.028244 \qquad \textbf{(2-2)}$$

where T is temperature in K. At 10 °C, for example, the fractionation factor between liquid and vapor is $\alpha_v^l = 1.01056262$, and at -10 °C, the fractionation factor between solid and vapor is slightly greater at $\alpha_v^s = 1.016018006$.

For HDO, the equilibrium fractionation factor between vapor and liquid is given by

$$\ln \alpha_v^l = 24.844 \times 10^3 / T^2 - 76.248 / T - 52.61 \times 10^{-3} \quad \textbf{(2-3)}$$

and between vapor and ice by

$$\ln \alpha_v^s = 16.288 \times 10^3 / T^2 - 0.0934 \times 10^{-3}. \quad \textbf{(2-4)}$$

Fractionation between liquid and solid during freezing or melting in ocean or lake water occurs at equilibrium and is not temperature-dependent [*Gat*, 1996], with

$$\alpha_l^s = 1.0035 \text{ for } {}^{18}\text{O and } \alpha_l^s = 1.0208 \text{ for D.} \quad \textbf{(2-5)}$$

2.2.3 Isotopic exchange at the surface

Isotopic exchange occurs at the surface between the atmosphere and soil, vegetation, land ice, sea ice, lakes and the ocean. Evaporation from open water is parameterized in ModelE using a bulk transfer method (see *Brutsaert* [1975], for example) whereby the evaporation rate is proportional to the diffusivity of the evaporating substance, the ventilation, and the humidity gradient between the thin layer of vapor directly above the surface of the open water and that above in the free atmosphere. Specifically, the evaporation rate E (in kg/m^2·s) is given by

$$E = D\rho U(q_s - q_a) \quad \textbf{(2-6)}$$

where D is a dimensionless diffusivity coefficient, ρ is density of moist air (kg /m^3), U is wind speed in the free atmosphere (m/s), q_s is the specific humidity of a thin, saturated

vapor layer at the liquid surface (g/kg), and q_a is the specific humidity in the free atmosphere (g/kg).

For the case of a heavy stable isotope, Eq. 2-6 is modified using the approach of *Jouzel et al.* [1987] and *Hoffmann et al.* [1998], where the isotopic composition of the evaporate is modeled as a separate tracer, but following the the same bulk transfer approach and subject to different stages of isotopic fractionation. Using this approach, the evaporation rate E_i of the given isotopic species is given by

$$E_i = D_i \rho U (q_{i,s} - q_{i,a}) \qquad \textbf{(2-7)}$$

where D_i is the diffusivity coefficient specific to the isotopic species, $q_{i,s}$ is the isotopic tracer concentration of the thin saturated vapor layer, and $q_{i,a}$ is the tracer concentration in the free-atmosphere.

This approach, whereby different water species are modeled using separate tracers, is typical of isotopic GCM implementations. It is important to note, however, that it is equivalent to the *Craig and Gordon* [1965] model, which captures the isotopic evolution of surface evaporate. First, the isotopic concentration $q_{i,a}$ in Eq. 2-7 is expressed in terms of the specific humidity q_a and the known isotopic ratio of the vapor R_v:

$$q_{i,a} = R_v q_a \,.$$

Similarly, the isotopic concentration in the saturated layer $q_{i,s}$ can be expressed in terms of the isotopic concentration of the liquid reservoir R_l and the equilibrium fractionation factor through

$$\alpha_{eq} = \frac{R_l}{R_s} = \frac{R_l}{\frac{q_{i,s}}{q_s}}$$

yielding

$$q_{i,s} = \frac{R_l q_s}{\alpha_{eq}}.$$

Substituting these into Eq. 2-7 gives

$$E_i = D_i \rho U (\frac{R_l q_s}{\alpha_{eq}} - R_v q_a)$$

The expresion for the isotopic composition of evaporate R_e is obtained by taking the ratio of the abundant and isotopic fluxes:

$$R_e = \frac{E_i}{E} = \frac{D_i (\frac{R_l q_s}{\alpha_{eq}} - R_v q_a)}{D(q_s - q_a)}.$$

The ratio D_i / D represents the kinetic fractionation factor $\alpha_k = D_i / D$. In the context of the Craig-Gordon model, rather than specific humidity q_a, it is more common to use the relative humidity h, given by $h = q_a / q_s$. This leads to the simplified expression

$$R_e = \alpha_k \frac{\frac{R_l}{\alpha_{eq}} - R_v h}{(1-h)}$$

which is found in *Yoshimura et al.* [2008], and equivalent to Eq. (15) in *Horita et al.* [2008]. In ModelE, α_{eq} is given by Eq. 2-1 and Eq. 2-3 depending on the isotopic species. For the kinetic fractionation factor $\alpha_{kin}(WS)$, the two-regime approximation of *Merlivat and Jouzel* [1979] (adopted in the iso-GCM work of *Jouzel et al.* [1987] and *Hoffman et al.* [1998]) was used for $\alpha_{kin}(WS)$. For $H_2{}^{18}O$, for $\alpha_{kin}(WS)$ is given by:

$$\alpha_{kin}(WS) = \begin{cases} 0.994 & WS < 7m/s \\ 1 - (WS \times 0.285 \times 10^{-3} + 0.82 \times 10^{-3}) & WS \geq 7m/s \end{cases} \quad \textbf{(2-8)}$$

and for HDO, $\alpha_{kin}(WS)$ is given by

$$\alpha_{kin}(WS) = \begin{cases} 0.99472 & WS < 7m/s \\ 1-(WS \times 0.2508 \times 10^{-3} + 0.7216 \times 10^{-3}) & WS \geq 7m/s \end{cases}. \quad \textbf{(2-9)}$$

Evaporation from bare soil and from the surface of vegetation (for example, a wet tree canopy) is computed similarly to open water, but without kinetic fractionation, based on the assumption that the surfaces are too rough or un-ventilated for kinetic fractionation to be a significant factor. Transpiration from vegetation occurs for all water tracers, but undergoes no fractionation, as has been well-observed experimentally [*Zimmerman et al.*, 1967; *Gat and Matsui*, 1991; *Strong et al.*, 2007]. Isotopic tracers are conserved during all surface exchanges, except for the ocean, which is considered as an infinite reservoir.In the opposite direction, isotopic transfer during dew and frost formation occurs under equilibrium, and is given by the fractionation factors in Eq. 2-1 through Eq. 2-4. Isotopic exchange between water and overlying lake or sea ice also occurs under equilibrium conditions, with fractionation factors given by Eq. 2-5.

2.2.4 Condensation

In ModelE, evaporation from the ocean is assumed to occur from a reservoir sufficiently large that its mass remains unchanged. In the atmosphere, by contrast, condensation is modeled explicitly as a transfer of mass between the vapor reservoir and the condensate. The condensation rates are dependent on microphysics parameterizations and will vary between GCMs, but in general can presumably be described by such a transfer of mass.

Fractionation during this condensation is implemented in ModelE as a Rayleigh distillation occurring over a single time-step by computing the fraction of isotopic tracer transferred from the vapor reservoir. Given the fraction of prognostic (isotopically light) vapor fq transferred from the vapor reservoir to condensate, it is straightforward to show from Eq. 1-4 that the fraction fq_i of heavy isotope tracer transferred out of the vapor reservoir to condensate is given by:

$$fq_i = 1-(1-fq)^{\alpha}. \quad \textbf{(2-10)}$$

To do this, let $R_0 = v_{i0}/v_0$ be the initial composition of the vapor where v_{i0} is the initial vapor isotope mass and v_0 is the initial prognostic vapor mass, and $R_v = v_i/v$ be the isotopic composition of the vapor after the condensate is removed. We express R_v as the result of a Rayleigh distillation, as in Eq. 1-4:

$$R_v = R_0 f^{\alpha-1} = \frac{v_{i0}}{v_0}\left(\frac{v}{v_0}\right)^{\alpha-1} = \frac{\frac{v_{i0}}{v_0}\left(\frac{v}{v_0}\right)^{\alpha}}{\frac{v}{v_0}} = \frac{v_{i0}}{v}\left(\frac{v}{v_0}\right)^{\alpha}$$

so that with $R_v = \frac{v_i}{v}$

$$v_i = v_{i0}\left(\frac{v}{v_0}\right)^{\alpha} .$$

Using this expression for v_i, we calculate the fraction fq_i of isotopic tracer removed:

$$fq_i = \frac{v_{i0} - v_i}{v_{i0}} = \frac{v_{i0} - v_{i0}\left(\frac{v}{v_0}\right)^{\alpha}}{v_{i0}} = 1 - \left(\frac{v}{v_0}\right)^{\alpha} = 1 - (1 - fq)^{\alpha} .$$

Vapor to liquid condensation occurs under equilibrium conditions, and α is given by the equilibrium fractionation factors in Eq. 2-1 and 2-3.

Vapor lost to deposition during ice crystal formation is also modeled as a Rayleigh distillation, but with a further, kinetic effect due to the lower diffusivity of the heavy isotopes. This effect is present only during supersaturation [*Jouzel and Merlivat*, 1984], which is negligible under warm conditions [*Jouzel et al.*, 1987]. As in *Jouzel et al.* [1987] and *Hoffman et al.* [1998], the combined effective fractionation factor α is given by

$$\alpha = \alpha_{eq}\alpha_{kin} . \qquad \textbf{(2-11)}$$

The equilibrium fractionation factor α_{eq} is given by Eq. 2-2 or Eq. 2-4 . The kinetic fractionation factor α_{kin} is given by

$$\alpha_{kin} = \frac{S}{\alpha_{eq}\left(\frac{D}{D'}\right)(S-1)+1} \qquad \textbf{(2-12)}$$

where *D/D'* is the ratio of isotopic diffusivities for the light (*D*) and heavy (*D'*) isotope species, obtained from experiment [*Merlivat*, 1978]. For $H_2{}^{18}O$, *D/D'* = 1.0285 and for HDO, *D/D'* = 1.0251. The supersaturation factor S is given by $S = 1 - 0.003*T$, with *T* in °C following *Hoffman et al.* [1998].

ModelE allows for either liquid or solid-phase precipitation in a grid cell, but not simultaneously. As such, the mixed-phase isotopic model of *Ciais and Jouzel* [1994] is not implemented in ModelE, representing one specific instance in which representation of isotopic processes is limited by the GCM's cloud physics parameterizations.

2.2.5 Condensate evaporation

The isotopic composition of condensate will be modified during descent by re-evaporation and equilibration. Re-evaporation is possible whenever condensate is exposed to unsaturated air, which for ModelE can occur in both convective and large scale clouds. In convective clouds, entrainment of dry environmental air into the convective column will lead to unsaturated conditions and condensate evaporation. The resultant evaporative cooling is also the primary driver of downdrafting and downward transport of vapor. Re-evaporation can also occur in the unsaturated layer below convective clouds. In large-scale clouds, sub-grid scale diffusion of cloudy air into clear air also results in unsaturated conditions and condensate evaporation [*Del Genio et al.*, 2005]. The effects of condensate evaporation are parameterized, to varying degrees, in most GCMs [*Gaffen et al.*, 1997].

Fractionation will occur during condensate evaporation, with the evaporate being lower in the heavy isotope, similar to what occurs during evaporation from the ocean. As with condensation itself, condensate re-evaporation rates are parameterization-dependent, but

can be described generally by a transfer of tracer from the condensate to the vapor reservoir. The fraction fq_i of isotopic tracer evaporated from the condensate is determined from the fraction fq of prognostic condensate that evaporates, analogous to condensation Eq. 2-10, but with fractionation in the opposite direction:

$$fq_i = 1 - (1 - fq)^{1/\alpha}. \tag{2-13}$$

The fractionation factor α includes an equilibrium effect, and also a kinetic effect. The effective fractionation is given by

$$\alpha_{eff} = \alpha_{eq}\alpha_{kin} \tag{2-14}$$

. The α_{kin} term accounts for the different vapor-phase diffusivities of the heavy and light isotopes across the humidity gradient between the saturated surface of the raindrop and the surrounding air, and is given by:

$$\alpha_{kin} = \frac{\alpha_{eq} RH}{\alpha_{eq} D(RH - 1) + 1} \tag{2-15}$$

where RH is the prognostic relative humidity expressed as a fraction, and D is the diffusivity ratio between heavy and light isotope. For $H_2{}^{18}O$, D = 1.0164 and for HDO, D = 1.0145, following from Table 2 of *Stewart* [1975], and discussed in *Hoffman et al.* [1998].

2.2.6 Condensate-vapor equilibration

Isotopic equilibration will occur between liquid raindrops and ambient vapor in saturated conditions. Re-evaporation represents a net one-way transfer from the condensate to vapor reservoir, with the heavy isotope subject to fractionation. Isotopic equilibration, in contrast, represents a two-way isotopic exchange between vapor and liquid condensate. Let $R_{c0} = c_{i0}/c_0$ be the isotopic composition of the condensate falling into vapor with isotopic composition $R_{v0} = v_{i0}/v_0$. Given the prognostic vapor mass v and condensate mass c of the light water, we need to obtain the new masses c_i and v_i of the heavy isotope,

such that isotopic equilibrium is achieved. Under equilibrium conditions, we have the fractionation constraint, similar to Eq. 1-7

$$\alpha_{eq} = \frac{c_i/c}{v_i/v} = \frac{c_i}{v_i}\frac{v}{c} = \frac{c_i}{v_i}k \qquad \textbf{(2-16)}$$

where $k = v/c$. Throughout equilibration, the isotopic mass is conserved

$$c_i + v_i = c_{i0} + v_{i0}\,. \qquad \textbf{(2-17)}$$

Using Eq. 2-16, we can express v_i in terms of c_i and known quantities

$$c_i + \frac{c_i}{\alpha_{eq}}k = c_{i0} + v_{i0} \qquad \textbf{(2-18)}$$

and solve for c_i

$$c_i = \frac{c_{i0} + v_{i0}}{1 + k/\alpha_{eq}}\,. \qquad \textbf{(2-19)}$$

Similarly for v_i , we can obtain

$$v_i = \frac{c_{i0} + v_{i0}}{1 + \alpha_{eq}/k}\,. \qquad \textbf{(2-20)}$$

Equilibration is a time-sensitive process, dependent upon the time for which a raindrop is exposed to a given vapor layer, and on the size of the raindrop. Following *Hoffmann et al* .[1998], it is assumed in ModelE that full equilibration occurs for large-scale condensate and that 50% equilibration occurs for convective condensate, reflecting larger-diameter raindrops in the latter [*Schmidt et al.*, 2005]. This reduced equilibration for convective condensate is different from *Jouzel et al.* [1987], in which full equilibration was assumed for both large-scale and convective condensate. While less sophiscated than the equilibration schemes of *Lee et al.* [2007] and *Risi et al.* [2010] (as noted in Section 1.6),

these fixed equilibration rates have been tested across several GCMS and produce reasonably accurate results.

Chapter 3
Observed and modeled controls on precipitation $\delta^{18}O$ over Europe: from local temperature to the Northern Annular Mode

3.1 Introduction

Stable water isotopes provide an important means paleoclimate reconstruction from many different sources such as ice cores, tree-cellulose, speleothems, and lake sediment carbonate [*Jones et al.*, 2009]. Across different proxy material, $\delta^{18}O$ composition is influenced strongly by precipitation falling over the region [*Sonntag and Schoch-Fischer*, 1985; *Leng and Marshall*, 2004; *Lachniet*, 2009], and a better understanding of the controls on precipitation $\delta^{18}O$ can improve interpretation of natural $\delta^{18}O$ archives influenced by the hydrological cycle.

The GNIP network is the primary means through which these controls have been identified, and is most dense over central Europe (Figure 1-3), allowing for uniquely detailed analyses of controls on regional $\delta^{18}O$ over multiple decades. Pioneering studies of controls on European $\delta^{18}O$ focused on the temperature effect [*Rozanski et al.*, 1992]. The $\delta^{18}O$ composition of precipitation, however, reflects the entire history of an air mass and so will also be influenced by non-local effects such as changes in transport pathway, and, ultimately, changes in atmospheric circulation [*Sonntag and Schoch-Fischer*, 1985; *Jouzel et al.*, 1997; *Araguas-Araguas et al.*, 2000]. Recently, the NAO was found to have considerable influence on European precipitation $\delta^{18}O$ during winter, with the positive NAO phase being associated with higher precipitation $\delta^{18}O$ [*Baldini et al.*, 2008]. There were also characteristic $\delta^{18}O$ signatures over Europe associated with the more general NAM, identified through analyses with isotopically-equipped general circulation models [*Schmidt et al.*, 2007; *Yoshimura et al.*, 2008]. Indeed, given its dominance of the NH climate, considerable effort has gone into reconstruction of the NAO, but this has been based largely on ice core $\delta^{18}O$ from Greenland [*Rogers et al.*, 1998; *Werner and Heimann*, 2002; *Vinther et al.*, 2003], or on non-isotopic proxies over Europe such as

tree-ring widths [*Cook et al.*, 2002], speleothem band counting [*Proctor et al.*, 2000], or on combinations thereof [*Trouet et al.*, 2009]. Much of this non-ice core proxy material also contains a $\delta^{18}O$ record, providing a complementary source of reconstruction information [*McDermott*, 2004; *Saurer et al.*, 2008; *Lachniet*, 2009].

The goal of this study was to better understand controls on European precipitation $\delta^{18}O$, motivated by an interest in improving interpretation of European $\delta^{18}O$ paleoclimate archives, and in assessing the performance of an isotopically-equipped GCM. There were three key differences from previous analyses. Firstly, the differences in isotope-climate relationships between seasons were considered explicitly. Many previous studies have focused on the season for which controls are expected to be strongest or on annual data [*Rozanski et al.*, 1992; *Vuille and Werner*, 2005]. Examination of seasonally-selected data is useful in identifying the strongest controls, but not all isotopic archives are available with sub-annual resolution, and so it is important to understand what, if anything, controls $\delta^{18}O$ over all months of the year during which precipitation occurs. Second, the spatial structure of controls on $\delta^{18}O$ was examined, for comparison to local temperature or pre-defined indices of circulation, such as those for the NAO, which may not in fact be the primary control of precipitation $\delta^{18}O$ composition over a given region. Lastly, any controls on European $\delta^{18}O$ identified in the GNIP observations were compared to those identified using the GISS ModelE GCM.

3.2 Data and model configuration

Isotopic data were obtained from the GNIP dataset. As noted above, compared to other areas in the world, the GNIP network is considerably more dense over central Europe, particularly over Germany, Austria and Switzerland. Only stations with at least 20 years of data were included in the analysis here, similar to criteria used previously [*Rozanski et al.*, 1992]. There were 23 stations in the GNIP database that met these criteria (Table 3-1), which represented half of all such stations in the GNIP database. Figure 3-1 shows the stations used in the analysis, with labels for selected stations.

Table 3-1. Names and locations for GNIP stations used in the analysis. Latitude and longitude are in decimal degrees.

Station Name	Latitude	Longitude	Elevation (m)	Number of observations
BAD SALZUFLEN	52.1	8.7	100	199
BERLIN	52.5	13.4	50	261
BERN	46.9	7.5	511	276
BRAUNSCHWEIG	52.3	10.5	88	198
CUXHAVEN	53.9	8.7	12	200
EMMERICH	51.8	6.6	43	198
GARMISCH-PARTENKIRCHEN	47.5	11.1	720	201
GRIMSEL	46.6	8.3	1950	269
GRONINGEN	53.2	6.6	1	408
GUTTANNEN	46.7	8.3	1055	268
HOHENPEISSENBERG	47.8	11.0	977	257
KARLSRUHE	49.0	8.4	120	201
KOBLENZ	50.4	7.6	97	197
KONSTANZ	47.7	9.2	447	279
KRAKOW (WOLA JUSTOWSKA)	50.1	19.9	205	334
MEIRINGEN	46.7	8.2	632	269
REGENSBURG	49.0	12.1	377	190
STUTTGART (CANNSTATT)	48.8	9.2	315	378
THONON-LES-BAINS	46.2	6.3	385	416
TRIER	49.8	6.7	273	200
VIENNA (HOHE WARTE)	48.3	16.4	203	516
WASSERKUPPE RHOEN	50.5	10.0	921	201
WUERZBURG	49.8	9.9	259	200

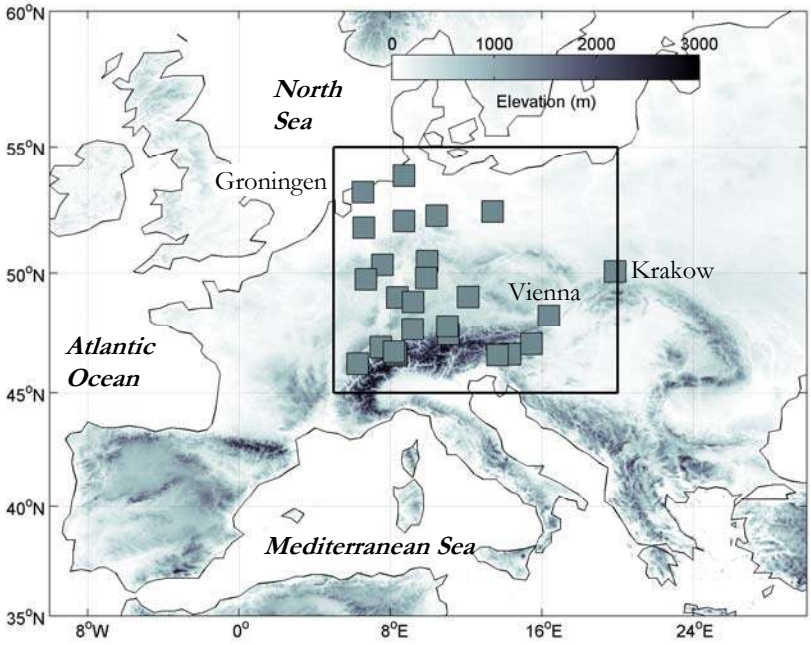

Figure 3-1. Map of GNIP stations used in the analysis, with labels for selected stations. The black rectangle shows the analysis domain.

Relationships between $\delta^{18}O$ and climate were examined for individual stations, and also for a regionally-averaged European $\delta^{18}O$ record, following *Rozanski et al.* [1992]. To construct the regional average, precipitation $\delta^{18}O$ values for reporting stations were interpolated linearly to a $1^o \times 1^o$ grid each month, and a regional mean $\delta^{18}O$ was computed by weighting each grid cell by its interpolated precipitation amount. This way, the regional $\delta^{18}O$ estimate accounted for the uneven spatial distribution of stations, and also for variation in precipitation, to avoid bias towards drier locations, similar to temporal precipitation-weighting used in calculating seasonal means [*Vuille et al.*, 2003b]. Confidence intervals (CIs) for all estimated parameters were computed at a 95% level using bootstrap re-sampling [*Efron and Gong*, 1983].

The spatial structure of atmospheric circulation controls on regional $\delta^{18}O$ was identified by computing correlation maps from the NCEP/NCAR Reanalysis [*Kalnay et al.*, 1996] for several meteorological fields at the surface and in the mid-troposphere. Reanalysis data were available at a $2.5^o \times 2.5^o$ horizontal resolution, with 17 vertical levels at

standard pressure levels. This approach followed the observational analyses of circulation controls over Greenland $\delta^{18}O$ [*Rogers et al.*, 1998], Himalayan $\delta^{18}O$ [*Vuille et al.*, 2005b] and western North American $\delta^{18}O$ [*Birks and Edwards*, 2009].

These observational results were compared to those modeled using the NASA GISS ModelE GCM [*Schmidt et al.*, 2005]. The GCM has been shown to realistically simulate $\delta^{18}O$ seasonality over representative European GNIP stations, and the main features of variability at a global scale [*Schmidt et al.*, 2005]. The model was run at a $4^{o} \times 5^{o}$ horizontal resolution with 20 vertical levels for 45 years starting in 1954, forced with interannually-varying sea-surface temperature (SST) and sea-ice fields from the HadISST 1.1 dataset [*Rayner et al.*, 2003], but with fixed greenhouse gas (GHG) concentrations, similar to previous GCM studies [*Vuille et al.*, 2003b]. The SSTs were prescribed from observations to induce realistic interannual variability, but a free-running, un-nudged atmosphere produces a somewhat independent realization from the data-constrained reanalysis. This precludes direct comparison to observed $\delta^{18}O$ trends and interannual variability, but guards against the results being overly sensitive to the choice of period analyzed.

3.3 Results

3.3.1 Mean climatologies

The GCM has been compared to observations at a global scale for basic climate diagnostics [*Schmidt et al.*, 2006] and isotopic quantities [*Schmidt et al.*, 2005]. Focusing more closely on Europe, we also compared spatial patterns of temperature, precipitation, and precipitation $\delta^{18}O$. For temperature (Figure 3-2), there were slight continental and topographic gradients in the GNIP observations during DJF, with cooler temperatures at greater distances from the North Sea eastward and into the Alps. There was some indication of this cooling gradient in the GCM, but with temperatures near the North Sea underestimated, which led to a cold bias of -2.3 ^{o}C in the GCM during DJF across the domain (Table 3-2). Temperatures during JJA were generally overestimated in the GCM, with an average bias of 2.5 °C across the domain. In both cases, this difference appeared to be statistically significant, given that the estimated GCM means fell outside the 95%

CI of the GNIP mean, and vice-versa. The GCM tended, therefore, to overestimate the temperature seasonality observed in the GNIP data. In part, this reflects the paucity of observations in the eastern region of the domain, which exhibited the greatest seasonality in the GCM.

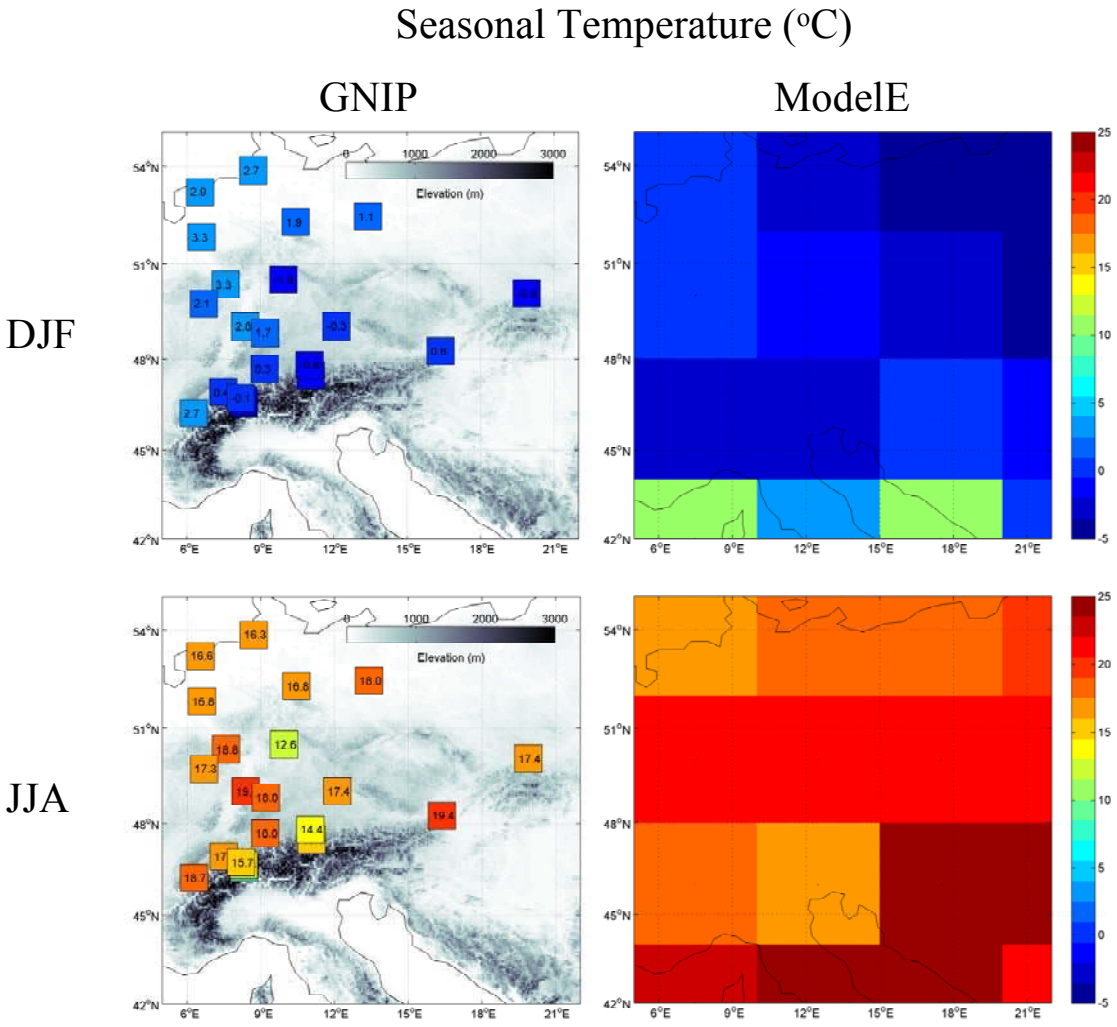

Figure 3-2. Seasonal temperatures (°C) at GNIP stations (left) and ModelE (right).

The main feature of the precipitation during both seasons is the increase from the northern European plain from rates of ~2 mm/day to values double that in the Alps (Figure 3-3). During DJF, there was a continental effect, with reduced precipitation moving inland from 1.9 mm/day at Groningen to a minimum value of 1.1 mm/day in Krakow. There was some indication of this continentality in the GCM, and also of the

Table 3-2. Regional means for GNIP observations and ModelE GCM. Values in parentheses are 95% confidence intervals.

	Months	Temperature (°C)	95% CI	Precipitation (mm/day)		$\delta^{18}O$ (‰)	95% CI	Years
GNIP	All	9.3	(8.7 , 9.9)	2.2	(2.1 , 2.3)	-9.1	(-9.3 8.8)	37
	DJF	1.0	(0.5 , 1.4)	1.9	(1.8 , 2.1)	-11.5	(-11.9 11.1)	36
	JJA	17.4	(17.2 , 17.7)	2.7	(2.6 , 2.9)	-7.0	(-7.2 6.8)	39
ModelE	All	9.0	(8.3 , 9.7)	1.8	(1.8 , 1.9)	-8.6	(-8.9 8.3)	45
	DJF	-1.3	(-1.7 0.9)	1.8	(1.8 , 1.9)	-12.6	(-12.8 12.3)	45
	JJA	19.9	(19.6 , 20.2)	1.8	(1.7 , 1.9)	-4.6	(-4.8 4.5)	45
Bias (ModelE - GNIP)	All	-0.3		-0.4		0.5		
	DJF	-2.3		-0.1		-1.1		
	JJA	2.5		-0.9		2.4		

increasing precipitation of up to 3.0 mm/day in the Alps, and good agreement across the domain as a whole, with a bias of only -0.1 mm/day in the GCM (Table 3-2). On average, there were wetter conditions in JJA (2.7 mm/day), particularly in the Alps, which were not captured across the domain in the GCM (1.8 mm/day). There was some increase in precipitation in the northeast region of the domain, but the GCM failed to capture the magnitude of the JJA increase in the Alps.

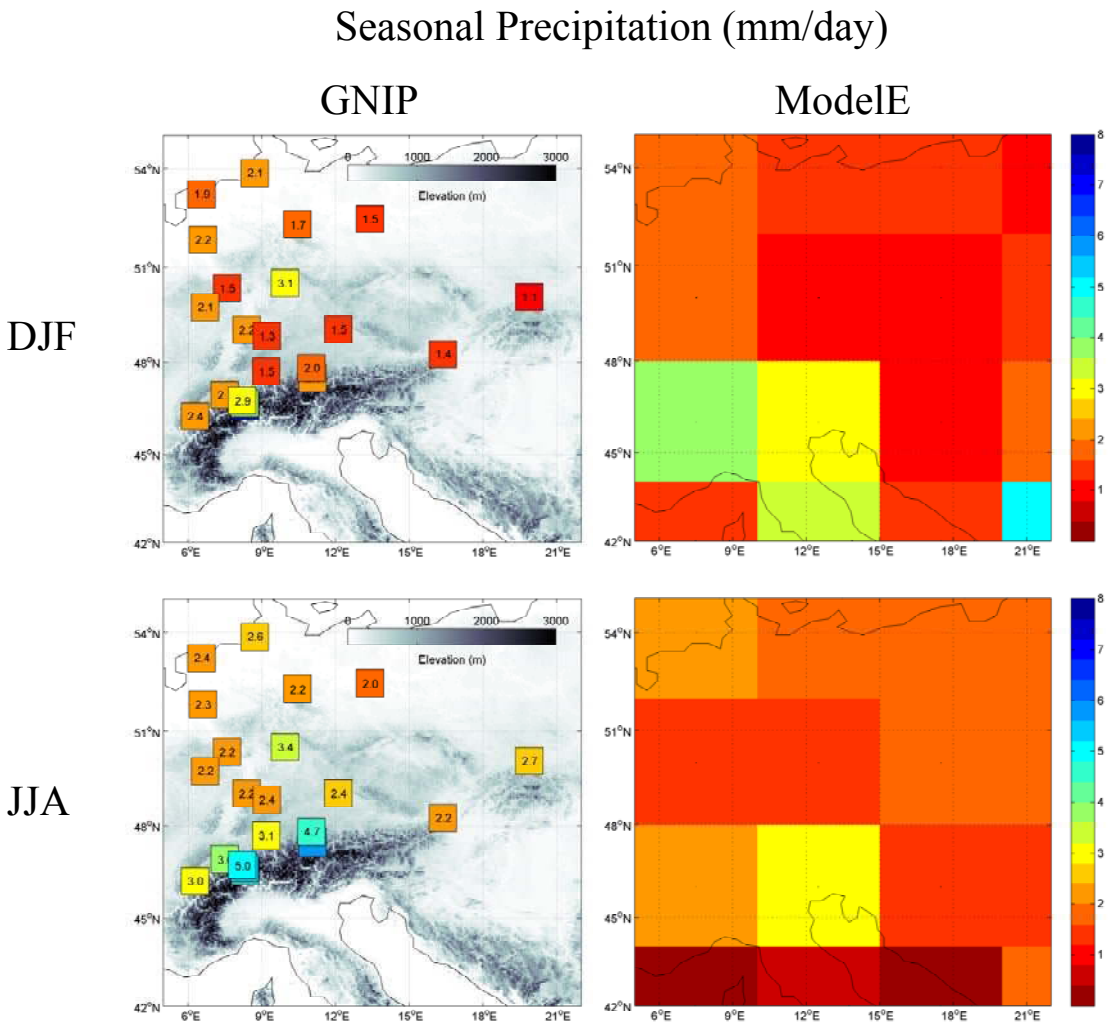

Figure 3-3. Seasonal precipitation (mm/day) at GNIP stations (left) and ModelE (right).

As with temperature, there were considerable spatial differences in precipitation $\delta^{18}O$ seasonality (Figure 3-4). The DJF values ranged from -8 ‰ in the coastal Netherlands to -13 ‰ in Krakow, and -15 ‰ at the high-elevation Swiss sites. In general, there was a

sharp depleting effect with topography moving southward from the northern European plain to the Alps. These continental and orographic gradients during DJF were captured by the GCM, but with the precipitation $\delta^{18}O$ overestimated near the coast in the northwest. Precipitation $\delta^{18}O$ was higher during JJA, particularly at the inland and high-elevation stations, and with a more even spatial distribution. In Groningen, for example, the mean JJA $\delta^{18}O$ of -6.5 ‰ was 2.6 ‰ greater than the DJF value, compared to a JJA mean of -7.2 ‰ in Krakow, which was -5.8 ‰ greater than the DJF $\delta^{18}O$. The GCM captured this seasonal difference, but almost universally overestimated the JJA $\delta^{18}O$, regardless of distance from the coast or elevation. As with temperature, the GCM tended to overestimate the seasonality of precipitation $\delta^{18}O$, but this could be related to the paucity of GNIP data in the northeast region of the domain.

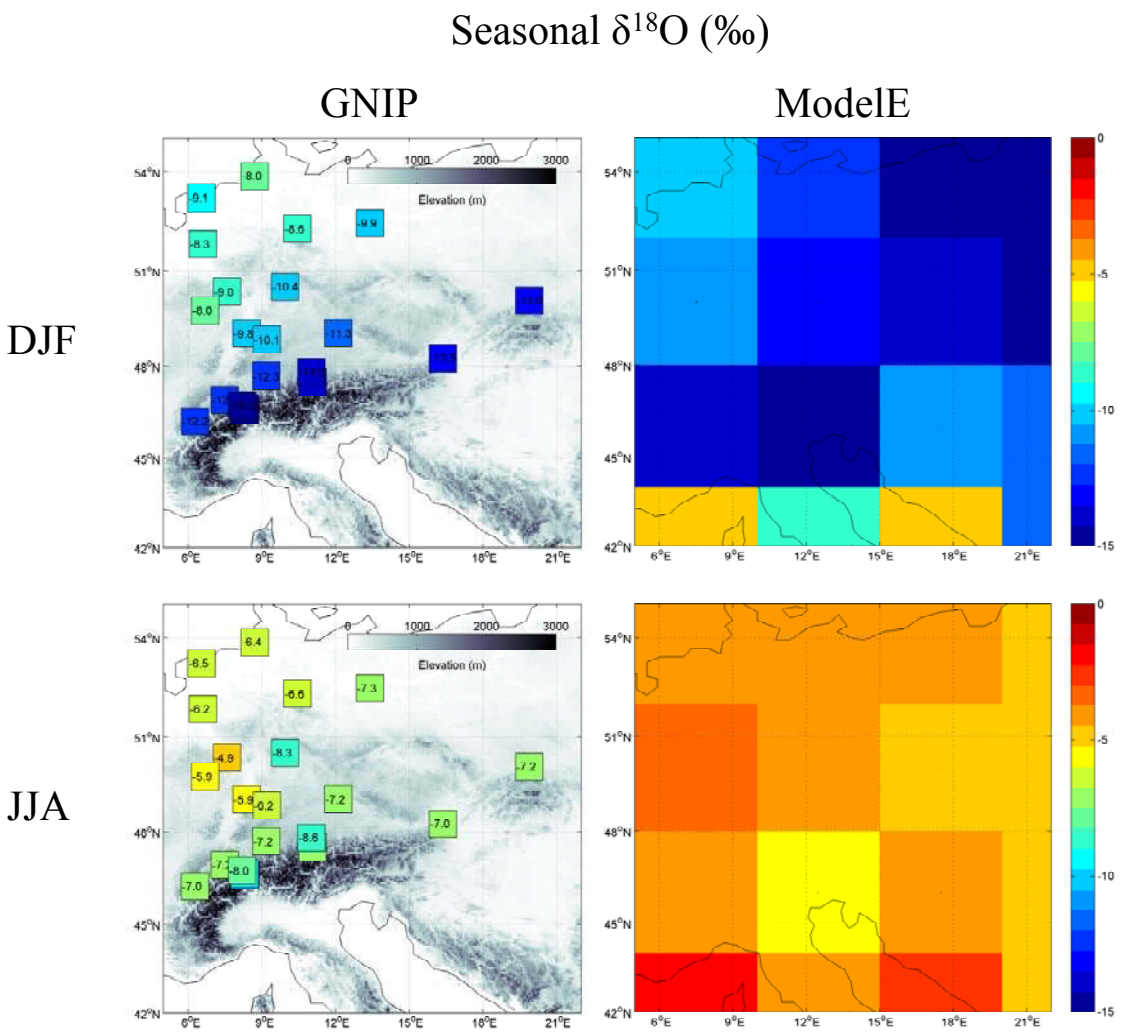

Figure 3-4. Seasonal precipitation $\delta^{18}O$ (‰) at GNIP stations (left) and ModelE (right).

3.3.2 Local temperature controls on $\delta^{18}O$

The correlations between local temperature anomalies and $\delta^{18}O$ anomalies are shown in Figure 3-5, at each station for the GNIP data, and in each grid cell for the GCM. There were significant differences for correlations computed separately for each season. During DJF, the strongest correlation in GNIP data of $r = 0.63$ was at Vienna, with a median of $r = 0.38$ across all stations, and six stations with correlations of $r \geq 0.50$.

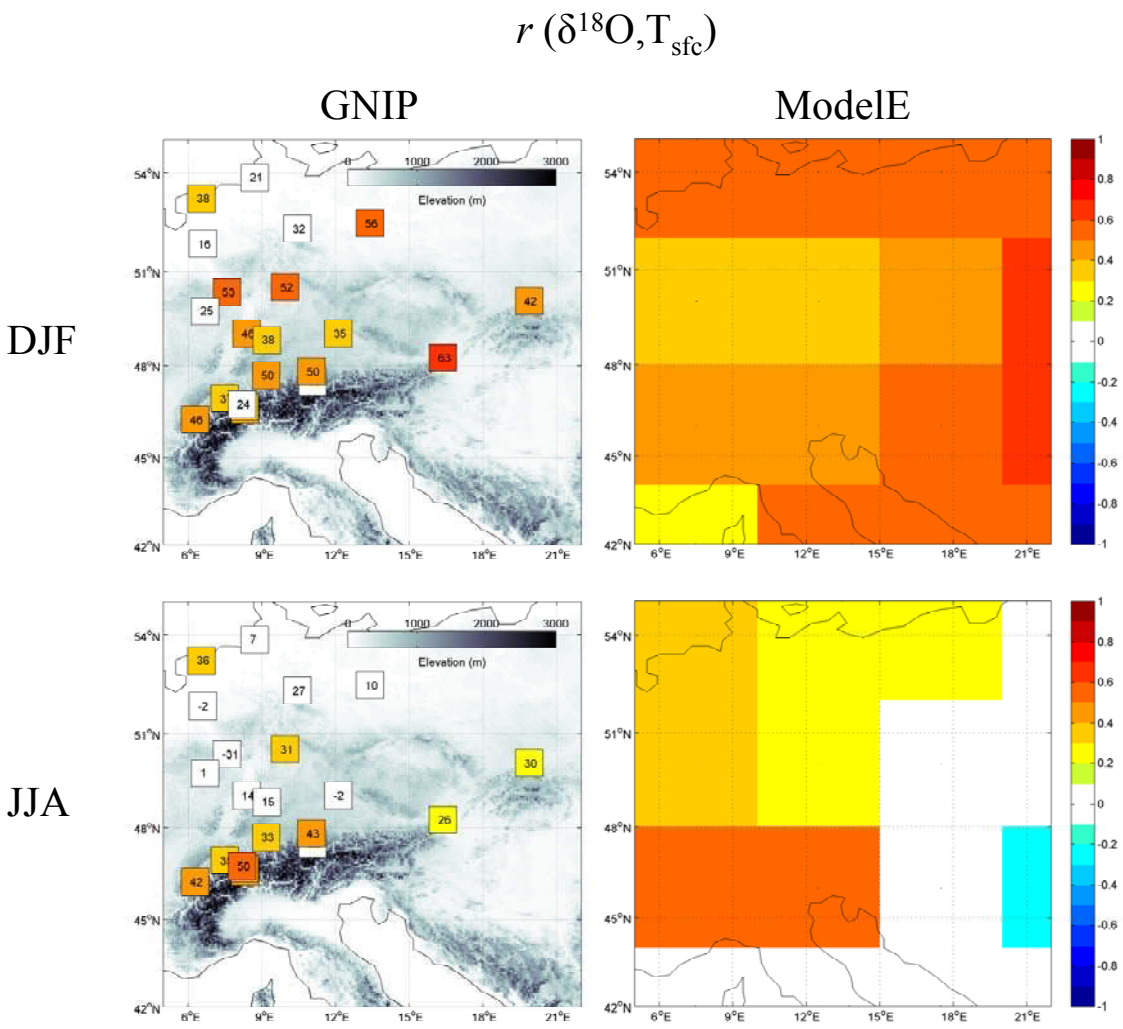

Figure 3-5. Correlation between monthly temperature and precipitation $\delta^{18}O$ anomalies for GNIP stations (left) and ModelE (right). Numbers in GNIP boxes are *r* x 100. White shading indicates *p* > 0.05. GNIP correlations are for 1963-2001, with the record for each station varying within that period.

There was also a general, if uneven, tendency towards a stronger temperature effect moving inland from the coast, which was better captured by the GCM compared to when all months were considered (not shown). Correlations weakened during JJA, with maximum correlation of $r = 0.50$ and median across stations of $r = 0.27$. The greatest decrease in correlation with temperature occurred over the Netherlands and Germany, but there were persistent positive correlations in Vienna and Krakow to the east, and over the Alps to the south, the latter pattern being fairly well represented in the GCM.

3.3.3 Spatial temperature controls on European $\delta^{18}O$

The high density of GNIP stations allowed for the analysis of the relationships between regional average $\delta^{18}O$ and temperature inside and outside of Europe. Figure 3-6 shows the linear relationship between the European $\delta^{18}O$ and temperature anomalies. As with the individual station correlations, these regional relationships were dependent on season, with a stronger correlation during DJF (r = 0.56) than JJA (r = 0.39). Whereas each seasonal correlation fell outside of the other's 95% confidence interval, this was not the case for the regression slopes, which would not be considered statistically distinct.

Precipitation $\delta^{18}O$ reflects the entire history of the air parcel from which the condensate originated, and, in particular, the proportion of original moisture that rained out during transit. This will in part be determined by cooling during sloped, cyclonic ascent, and therefore by the temperature along the air parcel's entire trajectory. To determine if the temperature correlation extended outside of the European domain, correlation maps were constructed between average European $\delta^{18}O$ and cell-by-cell surface temperature anomalies for the observations and GCM (Figure 3-7). During DJF, there is an area of strong positive correlation west of the analysis region with a southwest to northeast orientation, with that in the observations extending further southward, and that in the GCM more northward. At their strongest, the maximum values in the correlation field are higher than those for strictly European temperature for both the observations (r = 0.67 compared to r = 0.57) and particularly for the GCM (r = 0.74 compared to r = 0.58). In the case of the observations, this could partly be a function of the more heavily-assimilated nature of the reanalysis data compared to the simple temperature averaging across GNIP stations. But for the GCM, the temperature fields used for the local and regional GCM correlations are the same, and so the stronger regional correlation likely indicates a stronger, physical upstream influence.

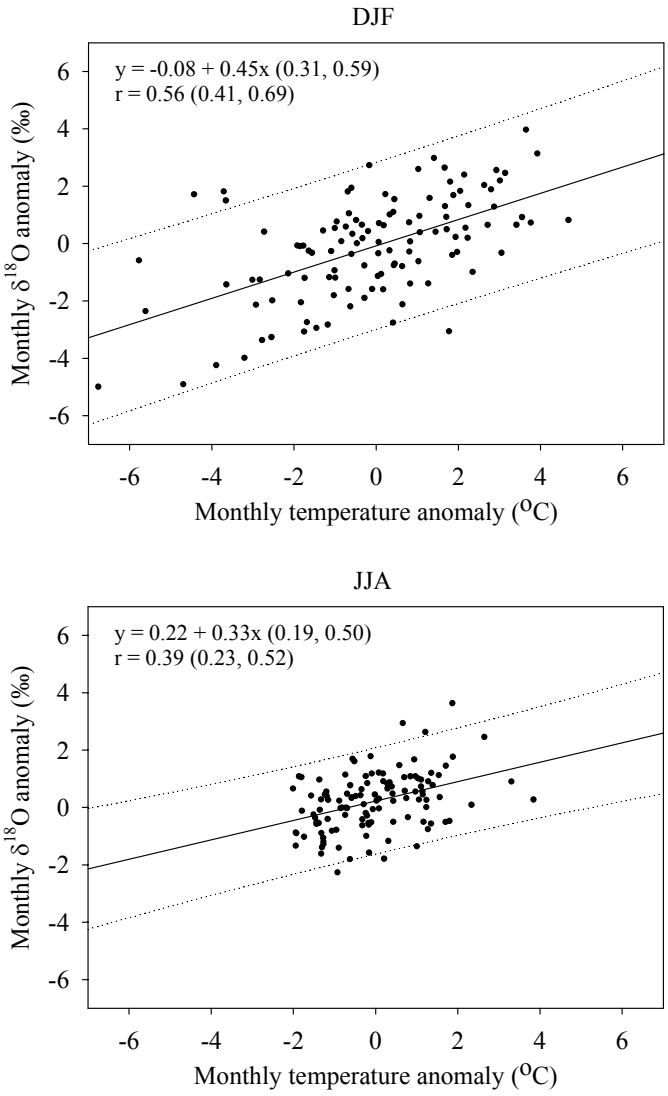

Figure 3-6. Regionally averaged temperature and $\delta^{18}O$ anomalies over central European GNIP stations, with estimated line of best-fit and 95% prediction intervals. Values in parentheses are 95% bootstrap confidence intervals for slope and correlation.

The centre of positive temperature correlation over Europe formed the northern centre of a dipole, with a corresponding centre of negative correlation over eastern North Africa. The strength of this negative pole was surprisingly strong in the observations (r = -0.63), nearly as strong as the main centre of positive correlation. There were also secondary centres of negative correlation over Greenland and positive correlation over Siberia and

the western Pacific, which were weaker in magnitude but robust in their spatial coherence.

During JJA, the regions of positive correlation had contracted, and were weaker at their strongest point. These maximum JJA correlations in the spatial field were still stronger, however, than the JJA correlations between European $\delta^{18}O$ and temperature strictly over Europe, with maxima of $r = 0.51$ in the observations and $r = 0.63$ in the GCM. The centres of negative correlation have also weakened and contracted during JJA, and the northern pole has also shifted eastward, with good agreement in these changes between GNIP and the GCM. Annual maps were also constructed (not shown), and as might be expected, appeared as weakened versions of the DJF maps.

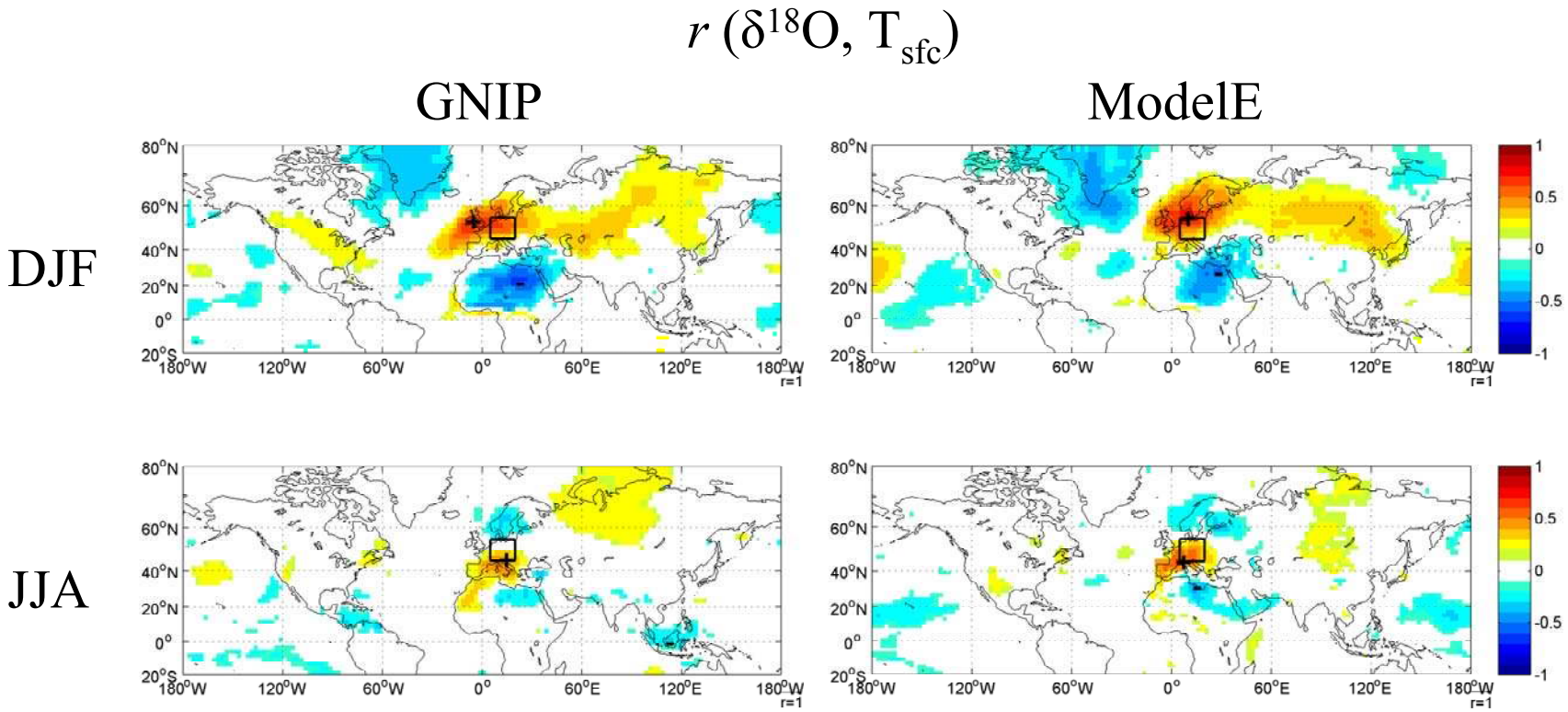

Figure 3-7. Correlation between European $\delta^{18}O$ (in the black rectangle) and surface temperature for GNIP/Reanalysis (left) and ModelE (right). Only correlations significant at the 95% level are shown. The '+' sign indicates the location of maximum positive correlation, and the '-' sign indicates the location of minimum negative correlation.

3.3.4 Atmospheric circulation controls on $\delta^{18}O$

The spatial extent and multi-centred structure of T-$\delta^{18}O$ correlations in Figure 3-7 suggests the influence of broad, circulation controls on $\delta^{18}O$. Following *Baldini et al.* [2008], Figure 3-8 shows the correlation between the NAO index [*Jones et al.*, 1997] and the monthly $\delta^{18}O$ anomalies at each station for different seasons. There were pronounced correlations during DJF between NAO and $\delta^{18}O$ anomalies, with maximum and median correlations across stations of $r = 0.77$ and $r = 0.37$, respectively. Statistically significant correlations were largely absent during JJA, with a maximum of only $r = 0.32$ and a median of $r = 0.15$. Of particular significance is the absence of significant positive correlation across the high-elevation sites in the Alps, where significant temperature correlations were found even during JJA. This suggests more local, exclusively orographic mechanisms for the JJA temperature effect in the Alps, or, if one should exist, a dominant circulation control other than the NAO. Similar seasonal changes were seen for NAO and regional $\delta^{18}O$ compared to individual stations. With all months, there was a correlation of $r = 0.34$ between the NAO and regional $\delta^{18}O$, with correlations of $r = 0.56$ during DJF and $r = 0.21$ for JJA. This lower summer correlation likely reflects the absence of any NAO influence on the high-elevation locations, in contrast to the temperature effects present at the high-elevation sites during the summer.

It is unsurprising that such relationships exist, given that the NAO significantly influences climate over Europe [*Hurrell et al.*, 2003]. There is no a priori reason why the NAO need be *the* dominant circulation control over European precipitation $\delta^{18}O$, however, given the complex set of factors that influence precipitation $\delta^{18}O$. It is possible that other, distinct, circulation features more strongly influence European precipitation $\delta^{18}O$ than the NAO. To assess whether this was the case, correlation maps were constructed between regional European $\delta^{18}O$ and various meteorological fields characterizing atmospheric circulation, similar to previous studies of $\delta^{18}O$ controls over Greenland and Antarctica [*Werner and Heimann*, 2002; *Schmidt et al.*, 2007], and low-latitude ice core sites [*Vuille and Werner*, 2005; *Vuille et al.*, 2005b].

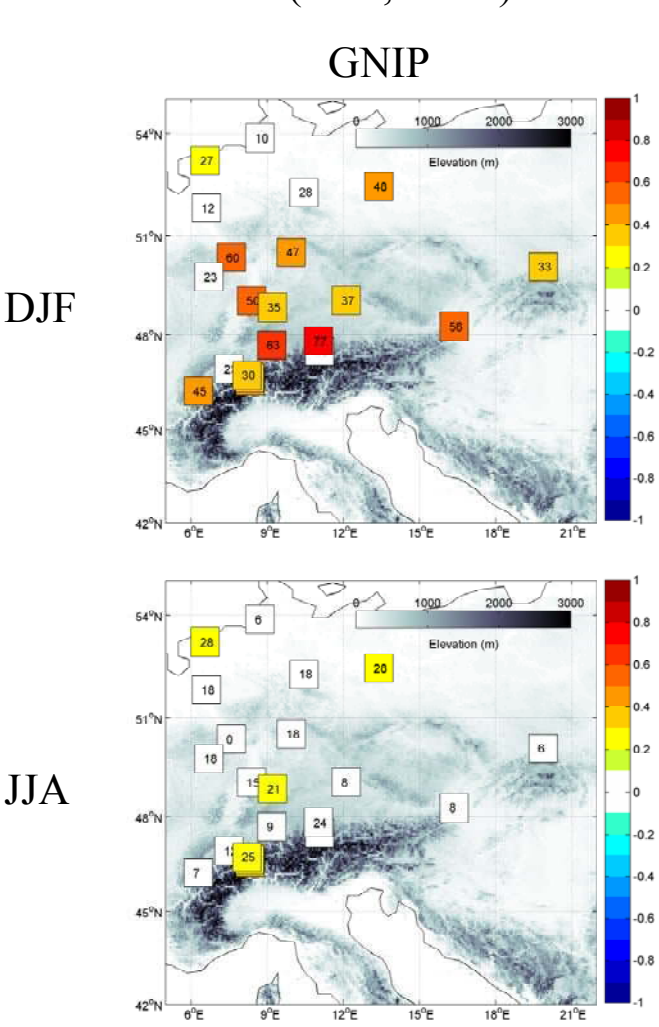

Figure 3-8. Correlations between the *Jones et al.* [1997] NAO index and monthly anomalies of $\delta^{18}O$ at GNIP stations, for different seasons. Numbers in GNIP boxes are *r* x 100. White shading indicates $p > 0.05$.

Figure 3-9 shows correlation maps between monthly anomalies of the regional European $\delta^{18}O$ and spatial fields of sea-level pressure (SLP) and surface winds. During DJF, there were clear circulation controls over GNIP $\delta^{18}O$, characterized by a north-south dipole centred over the analysis region. The dipole was NAO-like, but with centres of action different than in standard NAO definitions, a point to which we return below. The centre of the negative correlation pole has a minimum correlation of r = -0.58 and is centred over eastern Scandinavia, arcing from Iceland to central Asia, and the centre of positive

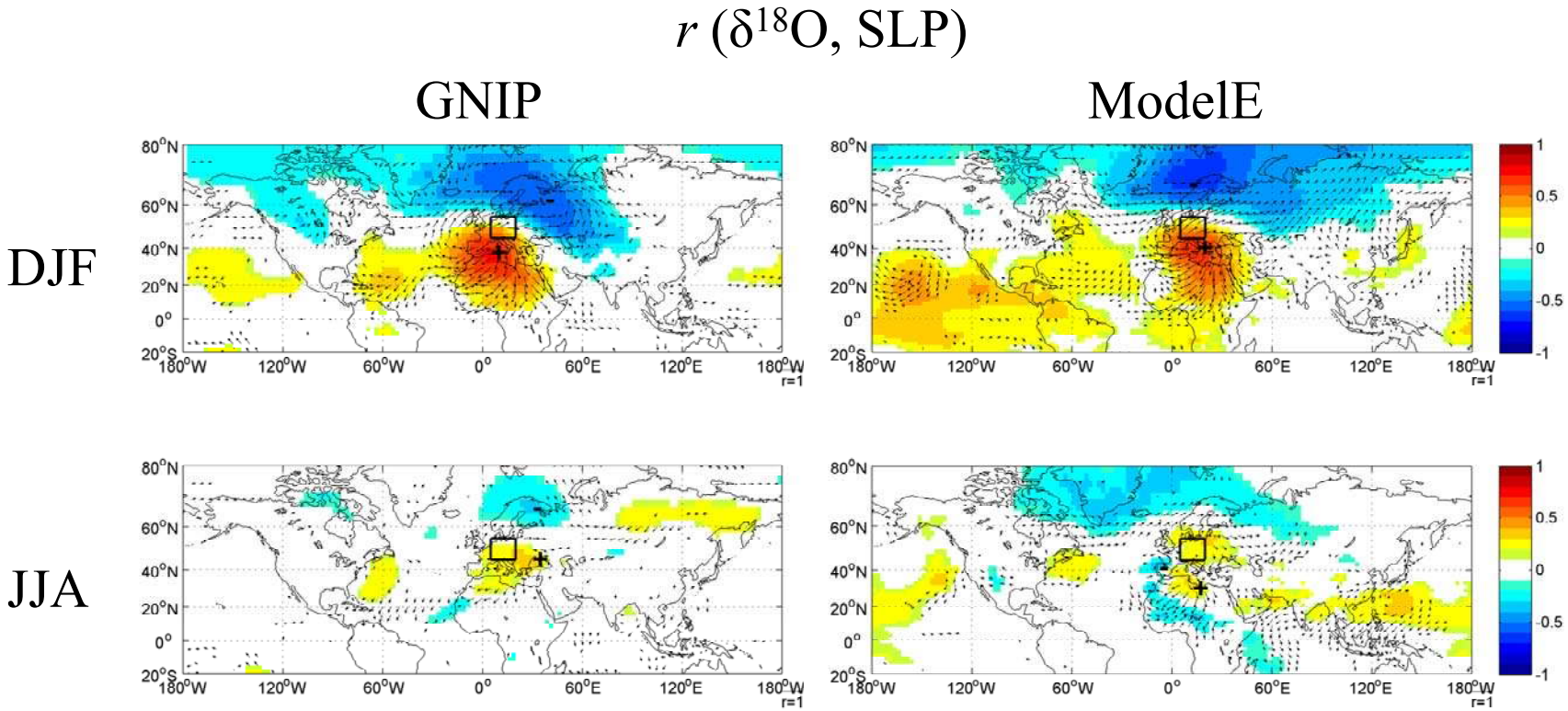

Figure 3-9. Surface circulation controls over European precipitation $\delta^{18}O$ for GNIP/Reanalysis (left) and ModelE (right). The colored shading shows the correlation between monthly anomalies in precipitation $\delta^{18}O$ in the boxed region and SLP anomalies. The arrows show the correlation between precipitation $\delta^{18}O$ and the *u* and *v* wind components, plotted as a vector.

correlation has a magnitude of $r = 0.72$, and was located over the central Mediterranean Sea. Thus, higher $\delta^{18}O$ over Europe is associated with a broad low-pressure anomaly to the north and a high-pressure anomaly to the south. Associated with the SLP dipole were pronounced controls in surface flow indicated by the correlation vectors. There was a positive correlation between $\delta^{18}O$ and southwesterly flow into the region, which formed part of the anticyclonic flow around the positive centre and cyclonic flow around the negative centre

This dipole structure was well captured in the GCM. The centre of the negative correlation region was over the Norwegian Sea, west of that in the observations, but with the same arc stretching from Iceland to Central Asia with a minimum correlation of $r = -0.67$. The main positive correlation centre was located in an identical position over the Mediterranean as for observations, with a maximum correlation of $r = 0.69$. The southwesterly flow into the analysis region was also apparent, along with the cyclonic and anticyclonic flow around the negative and positive correlation centres, respectively. In both observations and the GCM, there were also correlation centres appearing outside of the European sector, with negative correlation over much of the Arctic and extending into Canada, and positive correlation centres over Bermuda and Hawaii.

As with the temperature controls, there were weaker circulation controls during JJA. The maximum positive SLP correlation over the Mediterranean, for example, dropped to $r = 0.38$ and $r = 0.36$ for observations and GCM, respectively, with the signatures of all DJF correlation patterns contracting. Correlation maps were also constructed for all months of the year (not shown), and, as would be expected, were simply weakened versions of the DJF correlation maps.

During DJF, the main centre of positive Z_{500} correlation in the observations was centred identically to that in the SLP fields, with a maximum correlation of $r = 0.75$ (Figure 3-10). The region of negative correlation was centred in the high north Atlantic, and had a more wave-like quality than the SLP correlation field, arcing around the positive correlation centre to North Africa. The positive correlation centres over the Bermuda and Hawaiian subtropical highs seen in the SLP correlations were also apparent in the Z_{500}

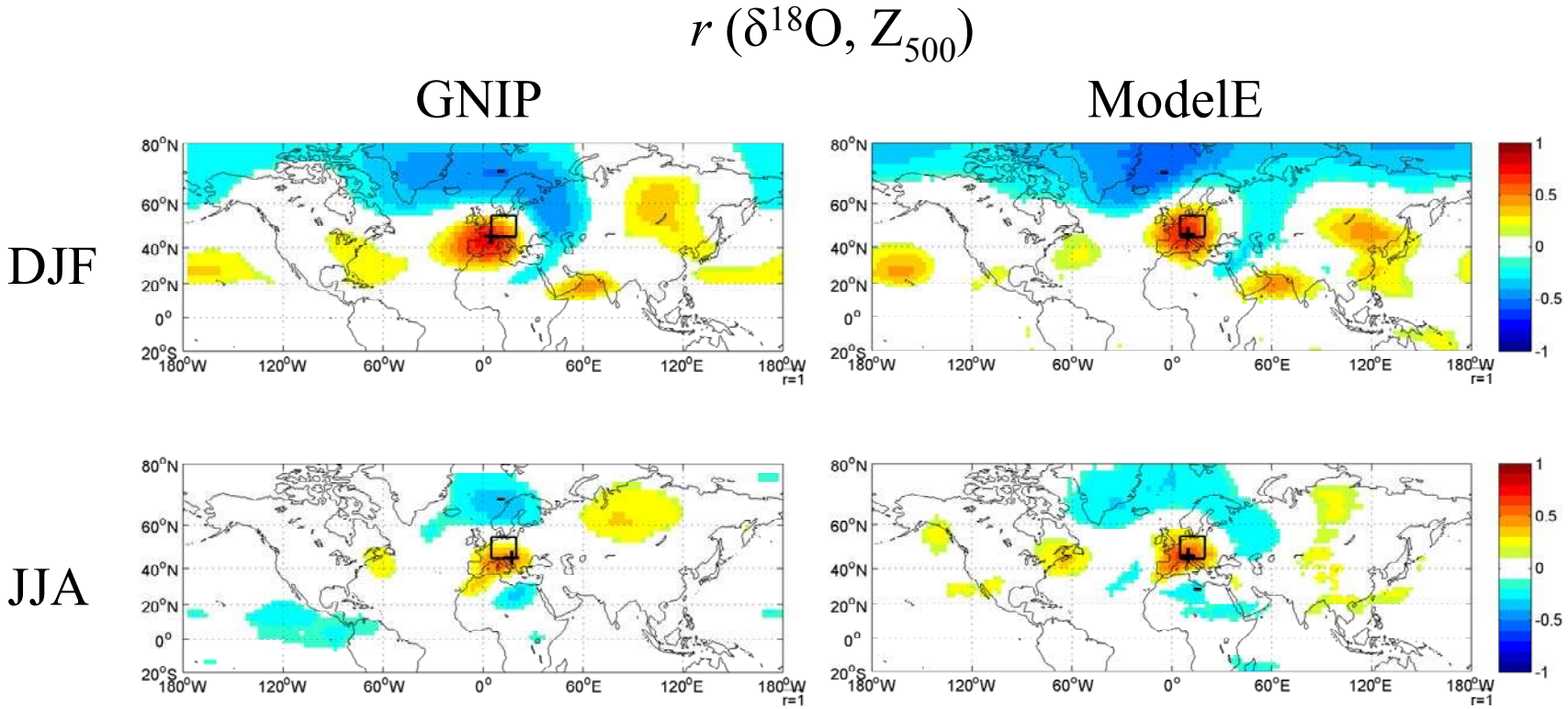

Figure 3-10. Mid-tropospheric circulation controls over European precipitation $\delta^{18}O$ for GNIP/Reanalysis (left) and ModelE (right). The colored shading shows the correlation between monthly anomalies in precipitation $\delta^{18}O$ in the boxed region and Z_{500} anomalies.

correlations, and there were new positive correlation centres over the Arabian Sea and Siberia, the latter of which could be linked with the Hawaiian correlation centre. These features also appeared in the GCM, where the negative correlation centre also arced around the Mediterranean, but with a greater concentration over the North Atlantic, and also with the positive correlation centres in the subtropics and Siberia. In both the observations and GCM, controls were characteristically weaker in JJA, but still with moderate positive correlation centres over the Mediterranean and negative correlation centres over the north Atlantic.

All surface and mid-tropospheric $\delta^{18}O$ correlations are summarized in Table 3-3, with selected correlations plotted in Figure 3-11 with 95% confidence intervals. Following the Azores-Iceland definition of the station-based NAO index, correlations were also calculated for a simple index based on the difference in SLP at the locations with maximum and minimum correlations. When the uncertainty in the estimator is considered, there is overlap in the range of the local (T_{local}) and regional maximum temperature ($T_{regional}$) correlations for observations, but greater separation in the GCM (Figure 3-11). Circulation-wise, there was a more robust separation between the NAO index and the controls identified empirically from the SLP and Z_{500} fields. Overall, the strongest and best-separated controls were at the centre of the positive Z_{500} correlation region ($Z500_{max}$) and the SLP difference index (SLP_{diff}), both of which were consistently outside of the NAO correlation's 95% confidence interval. This was followed by the maximum regional temperature. In general, correlations were higher during DJF than JJA, and also better-constrained in terms of their confidence interval width. In most cases, correlations from the GCM were stronger than observed correlations, but not outside of the latter's confidence intervals.

Table 3-3. Correlation summary for GNIP $\delta^{18}O$ observations and the ModelE GCM for: local surface temperature (T_{local}), maximum regional surface temperature ($T_{regional}$), NAO for station data, SLP and Z_{500} at the locations of minimum and maximum correlations and for the difference of the two.

					SLP			Z_{500}	
	Months	T_{local}	$T_{regional}$	**NAO**	**Min**	**Max**	**Max-min**	**Min**	**Max**
	All	0.48	0.47	0.34	-0.47	0.55	0.58	-0.40	0.66
GNIP	**DJF**	0.57	0.67	0.56	-0.58	0.72	0.72	-0.49	0.75
	JJA	0.39	0.51	0.21	-0.32	0.38	0.43	-0.37	0.55
	All	0.54	0.56	0.46	-0.52	0.59	0.63	-0.47	0.68
ModelE	**DJF**	0.58	0.74	0.59	-0.67	0.69	0.78	-0.58	0.72
	JJA	0.43	0.63	0.37	-0.38	0.36	0.52	-0.34	0.64

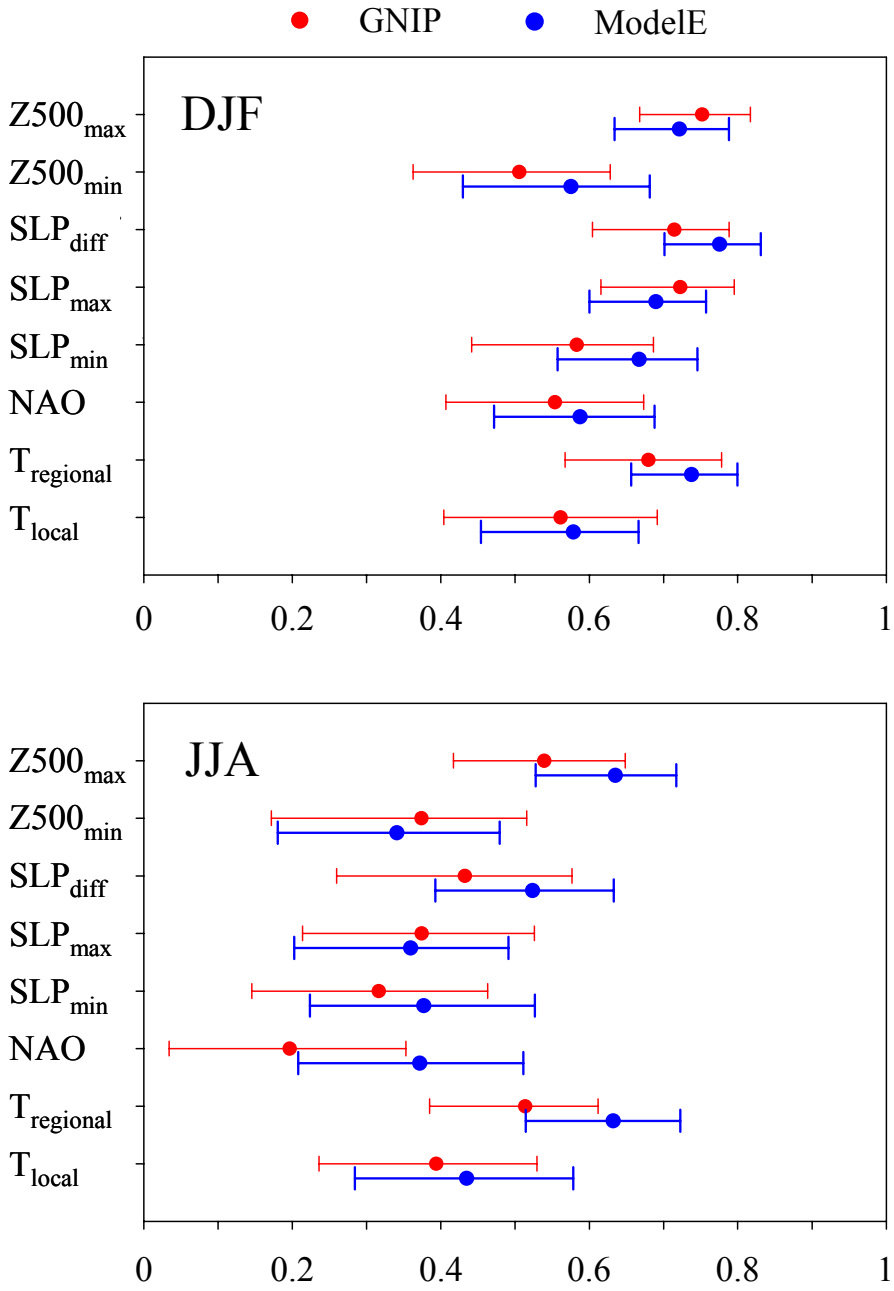

Figure 3-11. Correlation between precipitation $\delta^{18}O$ over Europe and selected variables from Table 3-3. Error bars are bootstrap-estimated 95% confidence intervals. The signs for $Z500_{min}$ and SLP_{min} have been reversed for comparison to the other correlations.

3.4 Discussion

3.4.1 Temperature controls

The local T-$\delta^{18}O$ correlations over Europe identified here have been well observed in previous observational studies [*Rozanski et al.*, 1992], and consistently identified at mid-latitudes in global-scale GCM analyses [*Hoffmann et al.*, 1998; *Cole et al.*, 1999; *Noone and Simmonds*, 2002; *Schmidt et al.*, 2007]. The correlations computed from the GNIP observations were weaker than previous studies, which was due to the use here of monthly anomalies in place of DJFM averages [*Baldini et al.*, 2008], and without the smoothing of *Rozanski et al.* [1992].

There were significant regional and seasonal variations in the T-$\delta^{18}O$ correlations computed across Europe. In general, annual T-$\delta^{18}O$ correlations (not shown) were the combination of a strong winter pattern and a weak summer pattern (Figure 3-5), with the exception of the high-elevation regions, where strong summer correlations persisted, and further inland at Vienna and Krakow, where weaker, but statistically significant, correlations persisted. The presence of JJA correlations in these regions is likely due to Rayleigh distillation in the Alps due to the orographic 'altitude effect' [*Araguas-Araguas et al.*, 2000; *Gat*, 2000] and in Vienna and Krakow due to their more distant location from the Atlantic Ocean, considered the dominant moisture source over central Europe [*Rozanski et al.*, 1982; *Numaguti*, 1999].

The weaker JJA T-$\delta^{18}O$ correlations are well-known at mid-latitudes, and have been attributed almost universally to the influence of evapotranspiration, which acts as a non-fractionating moisture source that obscures the depleting effects of Rayleigh distillation [*Jacob and Sonntag*, 1991; *Fricke and O'Neil*, 1999; *Kurita et al.*, 2004; *Peng et al.*, 2004; *Lee et al.*, 2007]. Estimates of moisture recycling vary depending on the data and approach used, but over Europe, consistently show a significant increase in the ratio of moisture recycled over land during summer compared to winter [*Dirmeyer and Brubaker*, 2007]. This is likely an important contributor to the more enriched summer $\delta^{18}O$ over Europe and to the weakened T-$\delta^{18}O$ correlations seen here. Related to this, it is also possible that within-atmosphere post-condensation exchange between precipitation and vapor modifies or even erases initial $\delta^{18}O$ signatures [*Gat*, 2000; *Worden et al.*, 2007], particularly for liquid-phase precipitation that will be more prevalent during the summer and lends itself more strongly to condensate-vapor exchange than solid-phase precipitation [*Friedman et al.*, 2002]. Statistically, the effect of these

two processes is to reduce the variability of precipitation $\delta^{18}O$ during the summer. This can be seen in Figure 3-6, where the ranges of temperature and $\delta^{18}O$ anomalies are much smaller during JJA than DJF, contributing to the weaker JJA correlation.

The GCM captured the basic range and seasonality of T-$\delta^{18}O$ correlations across Europe, but did only a modest job of capturing their spatial variation. This agreement in the overall range but disagreement in the spatial pattern between model and observations over Europe is similar to previous GCM results [*Hoffmann et al.*, 1998; *Noone and Simmonds*, 2002]. During DJF, the correlations over Germany were underestimated by the GCM, which, conversely, seemed to overestimate the temperature effect further inland. During JJA, the GCM over-estimated the temperature correlations over Germany, and underestimated them further inland. A possible factor for this difference is the GCM's JJA bias towards higher $\delta^{18}O$ seen in Figure 3-4. This warm summer bias was observed in more detail for the entire annual cycles in Groningen and Vienna [*Schmidt et al.*, 2005], and is likely related to the GCM's ~3 °C summer JJA bias over Europe, seen in a more comprehensive model-observation comparison [*Schmidt et al.*, 2006]. One feature that was captured, despite the GCM's low topographic resolution, was the persistent JJA temperature correlation over the Alps. While care should be taken in interpreting GCM results over such a small region, this does illustrate the GCM's ability to capture isotopic relationships over regions with a single strong control, in this case orographic rainout, which is consistent with the absence of strong NAO controls over the Alps during JJA.

These local temperature correlations were part of a broader pattern of positive temperature correlation (Figure 3-7), which was better captured by the GCM than the within-Europe variation in controls. The positive correlation centres extending outside of Europe reflect a Rayleigh-like temperature control over condensation and $\delta^{18}O$ distillation, and also, more simply, the spatial covariation of temperature at synoptic scales. This covariation was exclusively the case for the negative correlation centres positioned over eastern North Africa, weaker downstream positive correlation centre over Siberia, and weak upstream negative correlation centre over Greenland. *Werner and Heimann* [2002] identified a positive temperature correlation pattern over central Greenland $\delta^{18}O$, but not as part of a multi-centred teleconnection like that seen here. That study considered annual $\delta^{18}O$, however, and broad temperature patterns associated with Greenland $\delta^{18}O$ might be identified with seasonal separation.

3.4.2 Circulation controls

Following *Baldini et al.* [2008], a strong NAO control on $\delta^{18}O$ was identified during DJF (Figure 3-8), and the analysis here helped to elucidate its physical structure. The strength of the surface circulation controls was comparable to that of regional temperature, and was in fact stronger than local temperature in both observations and the GCM. The correlation vectors at the surface (Figure 3-9) also help to explain the *T*-$\delta^{18}O$ correlations in Figure 3-7. Higher $\delta^{18}O$ was associated with enhanced southwesterly flow to the north of the analysis region, which would be associated with warmer temperatures, and less moisture distillation, resulting in higher $\delta^{18}O$ during precipitation events over central Europe. An additional factor could be that the moisture is coming from more proximate sources than when transported over the high North Atlantic, and therefore undergoes less depletion during transport. This interpretation follows from the Rayleigh distillation model discussed in Section 1.4. But, as will be discussed in Chapter 5, the actual mechanism relating the circulation controls to the temperature effect is likely related more strongly to the effects of post-condensation exchange, and ultimately to the proportion of precipitation falling as snow compared to that falling as rain. The circulation controls also help to explain the strong dipole in temperature correlations in Figure 3-7. The elevated $\delta^{18}O$ values over Europe were associated with cooler temperatures over North Africa, which, in turn, were associated with stronger northerly flow to the east of the Mediterranean centre of positive correlation (Figure 3-9).

Despite the uncertainty in the estimated correlations, the strength of the anticyclonic circulation over the Mediterranean was as strong a predictor of European $\delta^{18}O$ as regional temperature, which is perhaps surprising given the traditional focus on local temperature as the main extratropical control over $\delta^{18}O$. Although the physical reasons for this require further investigation, this could reflect the fact that circulation variability strongly captures transport pathways, and therefore distillation distance, consistent with the argument of *Schmidt et al.* [2007] that isotopic archives may be better interpreted in a non-local sense.

As was the case for local temperature, atmospheric circulation controls were stronger for DJF than JJA, with the annual controls representing a strong winter signal muted by summertime noise. This is almost universally the case for the extratropical teleconnection patterns themselves, which are stronger during winter than summer, due to enhanced temperature gradients zonally and between land and sea. This certainly applies to the NAO which, although unique among

extratropical teleconnection patterns in being present during all seasons, is much stronger in winter than summer [*Hurrell et al.*, 2003]. It is argued that this seasonal difference in circulation controls contributes to the reduced summer variability in, and correlation between, temperature and $\delta^{18}O$ over Europe, in addition to the buffering effects of continental moisture recycling.

3.4.3 Teleconnection signatures

The teleconnection signatures in the circulation correlation maps correspond to well-known modes of NH variability. At the surface, the Mediterranean-North Atlantic dipole (Figure 3-9) was NAO-like, and the distinct correlation centres for the Bermuda and Hawaiian high pressure systems in the sub-tropics have also been associated with this leading NH mode of variability [*Wallace and Gutzler*, 1981]. This is also the case for the negative correlation pattern spanning the Arctic and extending over Canada. In combination, the signatures in the correlation maps are in fact similar to those of the AO or NAM, a more general mode of NH variability of which the NAO has been described as a regional expression [*Thompson and Wallace*, 1998; *Thompson et al.*, 2003]. Further evidence of a broader NH signature was seen in the mid-tropospheric circulation controls. The transition from an NAO-like north-south dipole at the surface (Figure 3-9) to a more wave-like structure in the mid-troposphere (Figure 3-10) is remarkably similar to the same vertical change seen between surface and mid-troposphere correlation maps between the geopotential height and AO/NAM [*Thompson and Wallace*, 1998; *Baldwin and Dunkerton*, 1999]. This is also the case for the mid-tropospheric emergence of positive correlation centres over Siberia and the Arabian Sea. Remarkably, European $\delta^{18}O$ variability would appear to reflect a complete spatial expression of the NAM, extending well beyond the Atlantic sector. This is perhaps relevant in the context of the debate between whether the NAO is an independent mode of climate variability, or a regional expression of the hemisphere-wide NAM [*Wallace*, 2000].

This analysis focused on the controls over $\delta^{18}O$ for a specific region. From the opposite perspective, *Schmidt et al.* [2007] identified the isotopic signature of the NAM by constructing correlation maps between an SLP-based NAM index and precipitation $\delta^{18}O$. In that study, moderate positive correlations were observed across Europe, indicating an association between higher $\delta^{18}O$ and positive phase of their empirical orthogonal function (EOF)-defined mode. This, in turn, is consistent with the positive phase of the NAO-like dipole in Figure 3-9. Similarly, *Yoshimura et al.* [2008] considered the isotopic signature of the AO across the NH for the GNIP observations and several isotopic GCMs, finding essentially the same signature. In both of these

studies, the correlations were comparable to annual analyses (not shown), and weaker than for our DJF analyses.

Despite the similarities to well-known teleconnection patterns, it should be emphasized that the centres of action in the correlation maps here were different from those in standard definitions. The SLP centres of action in Figure 3-9, for example, were well to the east of the standard *Jones et al.* [1997] NAO index, which is based on the difference between sea-level pressure over the Azores and Iceland. The EOF-based index of *Trenberth and Paolino* [1980], described in *Hurrell et al.* [2003], shows a northern centre of negative correlation corresponding generally to those identified here, but with the southern positive correlation centre located well to the west of the positive centre over the Mediterranean in Figure 3-9. Furthermore, no improvements were gained by using the Climate Prediction Centre NAO index based on the EOF-based approach of *Barnston and Livezey* [1987].

3.4.4 Implications for paleoclimate reconstruction

The results of this study have implications for traditional interpretations of $\delta^{18}O$ based on local temperature, or on hemispheric modes of variability. First, the improvements in considering regionally-averaged $\delta^{18}O$ from GNIP rather than those at individual stations illustrates the utility of combining multiple, targeted, isotopic archives across a given region. This technique has been applied for Greenland ice cores [*White et al.*, 1997; *Rogers et al.*, 1998] and for tree cellulose [*Treydte et al.*, 2007; *Saurer et al.*, 2008] in reconstructing short-term climatic variability; further $\delta^{18}O$ calibration and reconstruction efforts should emphasize this approach. With regional averaging and seasonal separation, higher $\delta^{18}O$ over Europe was associated with warmer temperatures, more southerly flow, and the positive phase of a hemisphere-wide mode of variability very similar in structure to the NAM. These controls could be considered when interpreting $\delta^{18}O$ archives, such as tree-ring cellulose and speleothems, which are strongly controlled by precipitation $\delta^{18}O$.

The NAM-like expression was identified through an empirical analysis of the controls, rather than with a single circulation index and *a priori* assumption of the dominant control. Indeed, as *Hurrell et al.* [2003] state, there is no single way of defining the NAO, and in general, isotopic calibrations based on predefined circulation indices may, in a statistical sense, miss their target. The spatial analysis here guards against any sensitivity to one particular definition, and illustrates

the improvements that can be gained from allowing the controls over a region's $\delta^{18}O$ to emerge empirically, and for the possibility of non-local controls [*Schmidt et al.*, 2007], which in this case were consistently stronger than the local controls. Further, it has been suggested that paleoclimatic reconstructions emphasize specific spatial patterns of temperature variability in place of hemisphere-wide averages and spatial modes of atmospheric circulation in place of single circulation indices [*Jones et al.*, 2009], and the controls identified here contribute towards such reconstructions. Isotopic archives in strongly correlated or anti-correlated regions could be combined in a targeted fashion for reconstructions of hemisphere-wide modes of variability, similar to what has been proposed in the tropics for the Andean and Himalayan ice cores [*Schmidt et al.*, 2007]. This could also be used to distinguish periods of hemisphere-wide temperature change from more internally-driven re-organizations of circulation, or to examine the temporal stability of a given teleconnection.

There were strong seasonal differences for both observations and the GCM in the temperature and circulation controls, with both being strong in the winter and weak in the summer. This underscores the improvements that can be gained by calibrating isotopic archives for different seasons due to the varying strength of atmospheric circulation controls on precipitation $\delta^{18}O$, in addition to the seasonally-varying influence of precipitation $\delta^{18}O$ on the particular archive. This is possible with high-resolution sampling for select speleothems [*Mattey et al.*, 2008] and tree-rings [*McCarroll and Loader*, 2004], although the more complex fractionation processes in both make climatic interpretation more difficult [*Fairchild et al.*, 2006]. But, conversely, given that sub-annual resolution will not always be available, or summer precipitation $\delta^{18}O$ may dominate the archive's signal in the case of tree-ring cellulose, the best possible annual controls on $\delta^{18}O$ can be identified through the empirical approach used in this study.

3.5 Conclusions

In this study, an attempt was made to better understand the controls on European precipitation $\delta^{18}O$ using GNIP observations and an isotopically-equipped GCM, motivated by interests in improving interpretation of paleoclimatic proxies in the region and validating the GCM's ability to identify atmospheric circulation controls. The main findings of this study were as follows:

1. Stronger temperature and circulation controls were identified for regional European $\delta^{18}O$ compared to individual sites, illustrating the potential gains from considering multiple isotopic archives.

2. Higher $\delta^{18}O$ over Europe is associated with warmer temperatures, southerly flow, deep anticyclonic circulation over the Mediterranean, and the positive phase of an NAM-like mode of NH variability. Statistically, the regional temperature and large-scale circulation controls were stronger than local temperature controls.

3. The annual controls over $\delta^{18}O$ are combinations of strong winter and weak summer controls. In addition to continental moisture recycling, the weaker summer controls are due to reduced variability in the summer circulation.

The GCM performed well in capturing the large-scale controls on European $\delta^{18}O$ observed in the GNIP data, most significantly the structure of the NAM through the depth of the troposphere, and the weaker controls on $\delta^{18}O$ during the summer. In general, the performance of the GCM in capturing these large-scale controls over Europe from observations should give us confidence in using it to identify controls over less data-rich regions at mid-latitudes. Also, the GCM could in theory be used to more mechanistically separate underlying controls on $\delta^{18}O$. In future studies, for example, it would be interesting to separate the effects of evapotranspiration and atmospheric moisture recycling from those associated with 'pure' Rayleigh distillation and changing circulation through a series of source-tagging and sensitivity experiments. The local temperature controls were not as well captured by the GCM due to its coarse resolution, and indeed, GCMs are better suited to studies of large-scale controls on $\delta^{18}O$ [*Vuille et al.*, 2005b]. It would be worth examining the performance of the isotopically-equipped version of the regional circulation model REMO [*Sturm et al.*, 2005] in modeling the variation of local $\delta^{18}O$ controls within Europe, or elsewhere.

Chapter 4
A GCM-based analysis of circulation controls on $\delta^{18}O$ in the southwest Yukon, Canada: implications for climate reconstructions in the region

4.1 Introduction

The objective of this chapter was to better understand isotopic records from the southwest (SW) Yukon region and any information they might contain about past atmospheric circulation. In particular, a significant drop in mean $\delta^{18}O$ occurred during the middle of the 19th century in two separate ice cores extracted from Mt. Logan in the southwest Yukon, immediately to the east of the Gulf of Alaska [*Holdsworth et al.*, 1992; *Fisher et al.*, 2004], and in sediment carbonate $\delta^{18}O$ recovered from a lake also in the SW Yukon [*Anderson et al.*, 2005]. The $\delta^{18}O$ record from the Northwest Col at 5340 m a.s.l. shows this shift as a 2-3 ‰ depletion during the late 1840s (Figure 4-1). Using an analytical model, *Fisher et al.* [2004] interpreted this shift as being caused by a stronger Aleutian Low (AL) pressure system (I've re-defined the acronym, which I think is useful), which brought moisture originating from more distant, southerly sources, and owing to this greater distance, enhanced isotopic depletion. Stronger southerly moisture transport was associated with increased snow accumulation at Mt. Logan [*Moore et al.*, 2002; *Rupper et al.*, 2004], but whether this corresponds to a similar control on $\delta^{18}O$ will depend strongly on the degree of isotopic distillation during transport.

It is also difficult to reconcile this interpretation of the $\delta^{18}O$ shift with climate reconstructions in the region during the 19th century. *D'Arrigo et al.* [2005], for example, used tree-ring samples ringing the North Pacific to reconstruct the strength of the AL since the 17th century, identifying a significant mid-19th century weakening of the AL, in disagreement with the interpretation of *Fisher et al.* [2004]. In this study we used an isotopically-equipped GCM to better understand controls on the $\delta^{18}O$ composition of precipitation in the SW Yukon, in order to better interpret isotopic archives in the region.

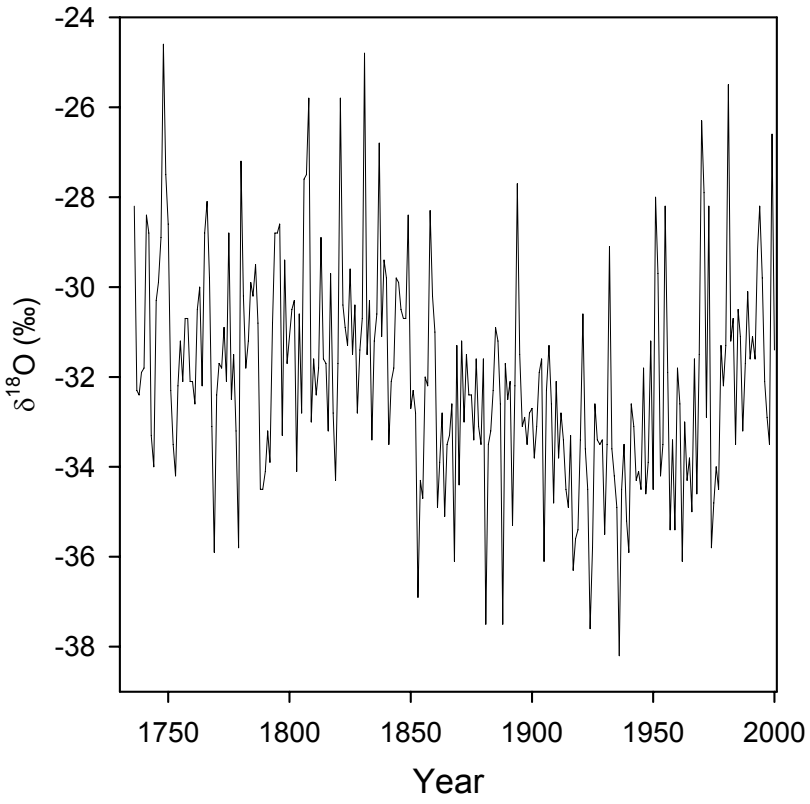

Figure 4-1. The Mt. Logan Northwest Col annual $\delta^{18}O$ record from *Holdsworth et al.* [1992].

4.2 Data and methods

Isotopically-equipped GCMs have been used to better understand controls on $\delta^{18}O$ over the polar ice sheets and other major ice-coring sites [*Werner and Heimann*, 2002; *Vuille et al.*, 2003a], and in Chapter 3, GISS ModelE was shown to accurately capture circulation controls over Europe. In this study, the same GISS ModelE configuration as described in Section 2.2 was used. The choice of simulation period was arbitrary and, as such, ours is an analogue study, similar to that of *Edwards et al.* [2001], where we assume that any contemporary meteorological controls on precipitation $\delta^{18}O$ are persistent across time. Unlike the GCM, steady-state models such as that used in *Fisher et al.* [2004] rely upon the balance between zonal and meridional transport being prescribed in order to produce a realistic present-day climatology.

Correlation maps were created between precipitation $\delta^{18}O$ over the SW Yukon and sea-level pressure and moisture flux in the spatial domain, similar to those in Chapter 3. Moisture flux between 974 hPa and 909 hPa was computed as a vertically-integrated quantity following *Peixoto and Oort* [1992]. As in *Werner and Heimann* [2002], we considered the $\delta^{18}O$ values spanning several grid points (58 to 64°N, 142 to 132°W) rather than a single grid point. In calculating $\delta^{18}O$ averages, monthly values were weighted by precipitation amount, and we allowed for different seasonal controls by also constructing correlation maps separately for the warm season (March through August) and cool season (September through February). We also substituted surface temperature and precipitation amount for precipitation $\delta^{18}O$ over the SW Yukon, to understand circulation controls on basic climate parameters.

Finally, we constructed correlation maps between mid-tropospheric moisture circulation and vapor $\delta^{18}O$ over the SW Yukon analysis region. Identifying controls on vapor $\delta^{18}O$ provided an additional check on controls on the moisture reservoir above the ice core site, whose surrounding topography is only very coarsely resolved by the GCM. Moisture-weighted, mean vapor $\delta^{18}O$ was calculated between 760 and 470 hPa over the analysis region, and correlated against the fields of moisture circulation between 760 and 470 hPa and geopotential height at 630 hPa. For all meteorological fields, only correlations significant at a 95% level are shown.

4.3 Results

Observed $\delta^{18}O$ values at GNIP stations in the region were generally well-simulated by the GCM (Table 4-1). At Barrow on Alaska's North Slopes, the modeled DJF and JJA $\delta^{18}O$ means of -22.7 ‰ and -15.8 ‰, respectively, were close to the observed means of -21.1 ‰ and -14.7 ‰. Modeled and observed values were also in good agreement for Bethel, in the southwest corner of Alaska. The model did not capture the cold season depletion in Whitehorse, or at the plateau of the two Logan drill sites (~ -32 ‰), where the sharp orographic rainout cannot be captured by the low topographic resolution of the GCM. Further inland at Yellowknife in the NWT, however, the modeled DJF and JJA $\delta^{18}O$ means of -24.2 ‰ and -14.9 ‰ are in good agreement with the observed means of

-25.1 ‰ and -16.8 ‰. We emphasize that any controls identified reflect those over the SW Yukon in general, and not for a specific proxy site.

Table 4-1. Precipitation $\delta^{18}O$ (‰) observed at GNIP stations and modeled with GISS ModelE.

			GNIP		ModelE	
Location	Lat	Lon	DJF	JJA	DJF	JJA
Barrow, AK	71°17N	156°45W	-21.1	-14.7	-22.7	-15.8
Bethel, AK	60°47N	161°45W	-15.1	-11.0	-15.7	-12.1
Whitehorse, YK	60°43N	135°03W	-23.8	-18.7	-18.3	-18.2
Yellowknife, NWT	62°27N	114°24W	-25.1	-16.8	-24.2	-14.9

Annually, there is some evidence of control on SW Yukon precipitation $\delta^{18}O$ by atmospheric circulation in the North Pacific (Figure 4-2a), with an indication of higher $\delta^{18}O$ being associated with southerly flow and a negative SLP correlation over southwestern Alaska. There is stronger evidence of control over vapor $\delta^{18}O$ (Figure 4-2b), with an additional center of positive 630 hPa geopotential height correlation east of the analysis region, which is associated with anticyclonic circulation and, given its position, southeasterly flow into the analysis region. The strongest annual controls are on precipitation amount (Figure 4-2c) and temperature (Figure 4-2d). The negative correlation pattern centered over the Gulf of Alaska associates a deeper AL with enhanced precipitation and warmer temperatures over the analysis region. During the warm season (Figure 4-3), the circulation controls are generally weaker than for the annually-averaged cases.

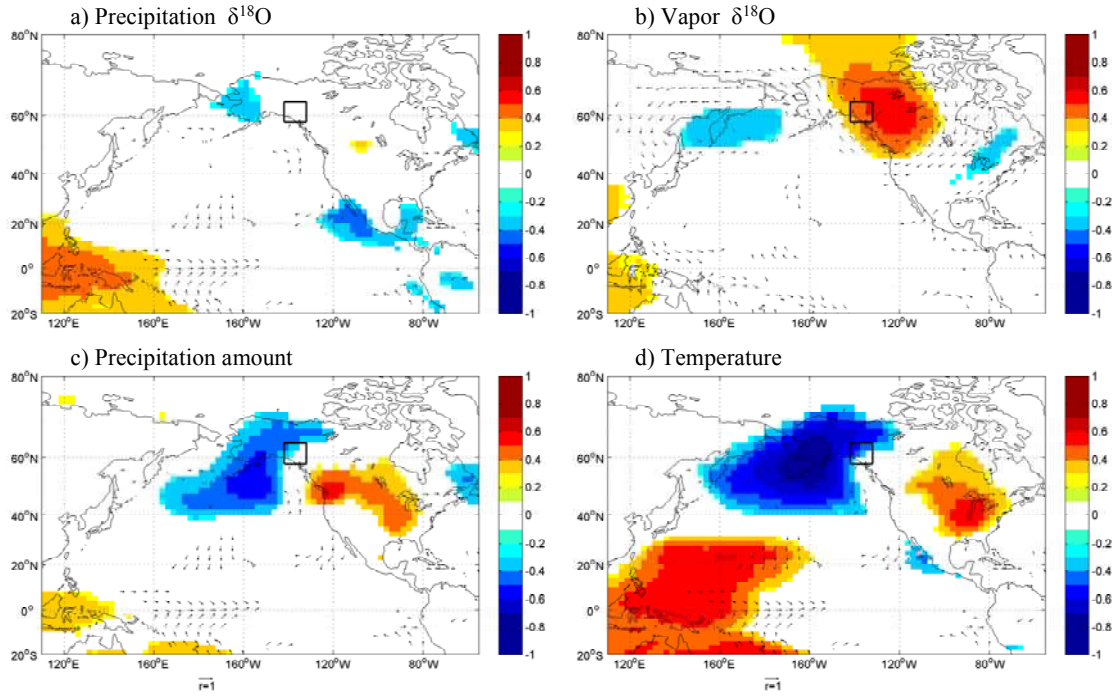

Figure 4-2. Annual circulation and moisture-flux correlation maps for: a) precipitation $\delta^{18}O$ b) mid-tropospheric vapor $\delta^{18}O$ c) precipitation amount and d) surface temperature over the SW Yukon, bounded by the black box. The colored shading indicates the correlation between the climate parameter over the SW Yukon and SLP (panels a, c, d) and geopotential height at 630 hPa (panel b). Vector lengths indicate the correlation between the climate parameters over the SW Yukon and moisture flux in each of the *u* and *v* direction, for surface (panels a, c, d) and mid-tropospheric (panel b) moisture flux.

The circulation controls on precipitation $\delta^{18}O$ over the SW Yukon are much stronger during the cool season (Figure 4-4a), with a strong association between higher precipitation $\delta^{18}O$ and more southerly moisture flux around a deeper AL. The same relationship appears for vapor $\delta^{18}O$ in the mid-troposphere (Figure 4-4b), but as part of a tripole, with a positive, anti-cyclonic center over western North America and a negative, cyclonic centre over the eastern US. To varying degree across seasons, tropical Pacific signatures appear in the SLP correlations, with higher $\delta^{18}O$, and wetter and warmer conditions over the SW Yukon, associated with positive pressure anomalies over the western Pacific.

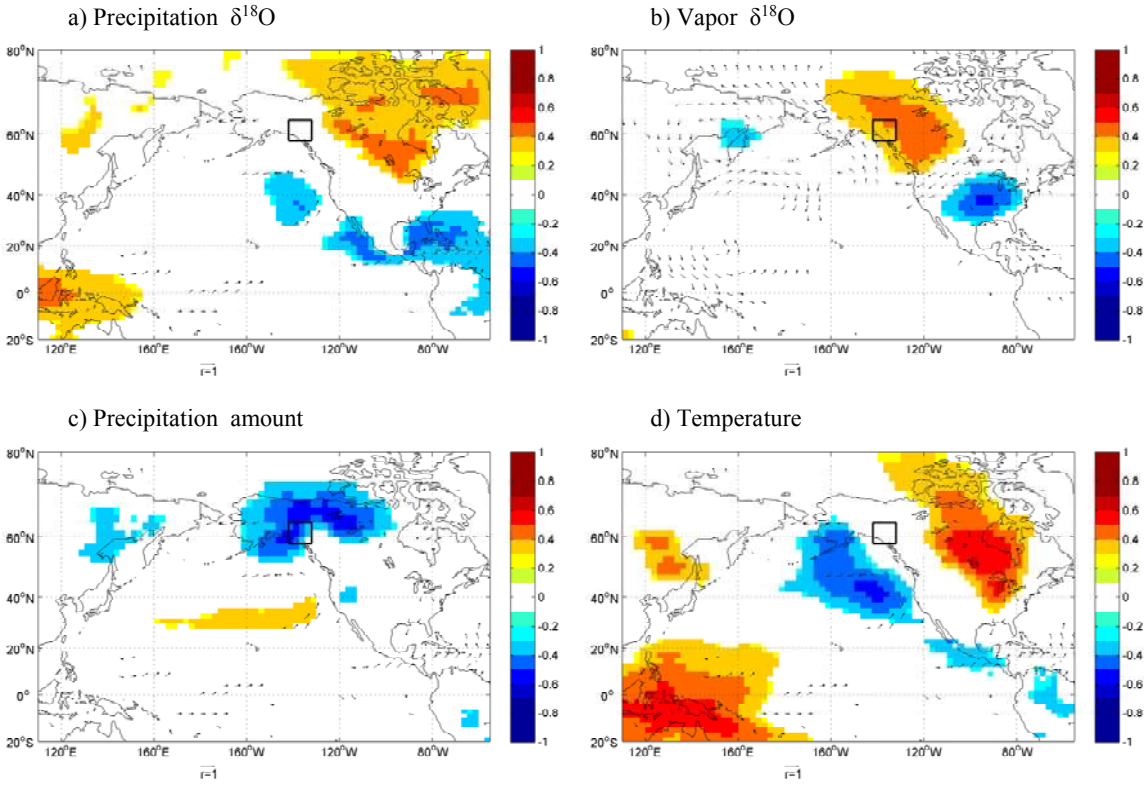

Figure 4-3. Same as Figure 4-2, but for warm-season (March to August).

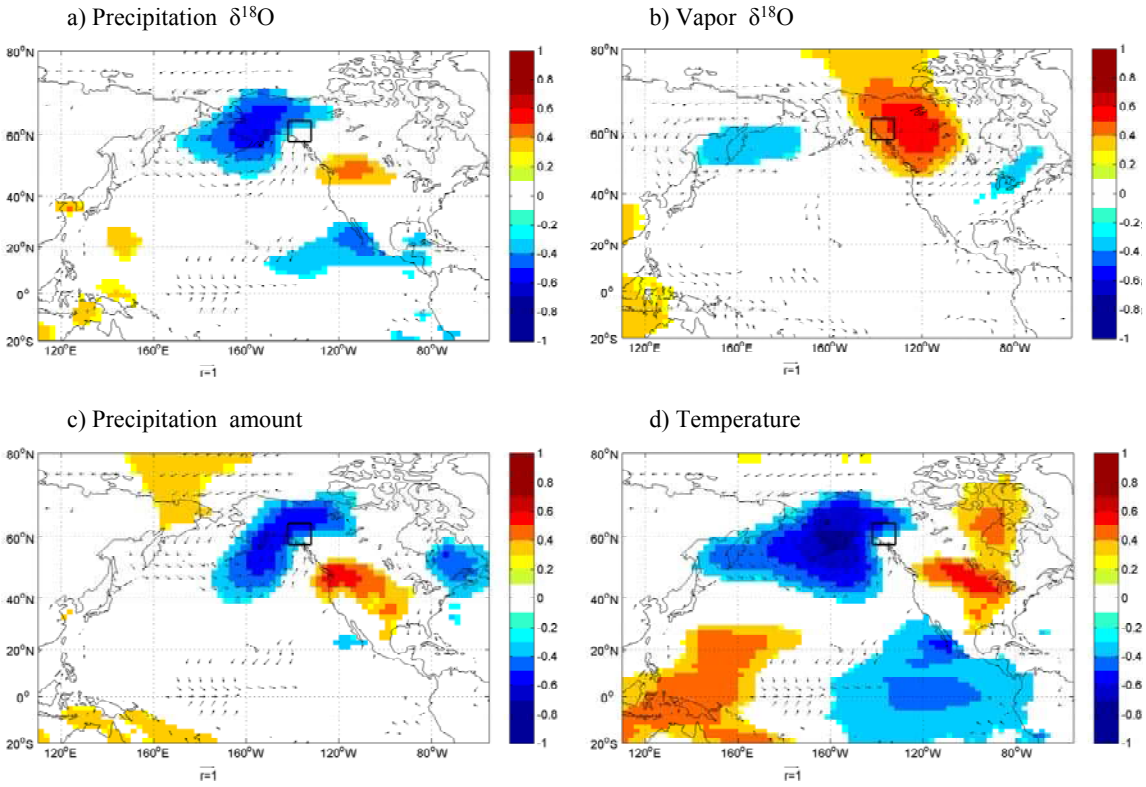

Figure 4-4. Same as Figure 4-2, but for cool-season (September to February).

We note that similar cool-season controls on $\delta^{18}O$ were identified using composite maps (not shown). These composites were associated with a ~1.5 ‰ difference in low and high $\delta^{18}O$ years over the SW Yukon, slightly less than the observed mid-19th century shift in the ice core.

4.4 Discussion

Our results indicate that higher $\delta^{18}O$ over the SW Yukon is associated with southerly moisture flux into the region. This moisture flux, in turn, is associated with enhanced cyclonic circulation around a deeper AL. In the mid-troposphere, our results indicate the presence of the tripole-like control on vapor $\delta^{18}O$ (Figure 4-4b) as well as a surface feature related to the AL (Figure 4-4a). These features are similar to the PNA teleconnection identified by *Wallace and Gutzler* [1981] whose surface expression is the AL. Furthermore, the PNA-like structure of the correlation maps is consistent with the controls identified by *Birks and Edwards* [*Birks and Edwards*, 2009] over Western Canada. The positive SLP correlations across the western equatorial Pacific, although less robust across seasons, are indicative of warm ENSO conditions. This relationship between warm ENSO, a deeper AL and positive PNA is consistent with observational studies [*Trenberth and Hurrell*, 1994] and controls on Mt. Logan snow accumulation [*Moore et al.*, 2002].

Seasonality is important in controlling $\delta^{18}O$, due mainly to persistent features such as the AL often being wintertime-only phenomena [*Trenberth and Hurrell*, 1994]. The effects of seasonality on $\delta^{18}O$ controls was seen clearly over Europe in Chapter 3, and also for Greenland, where a strong NAO signature was seen in winter months, but only weakly during summer months [*Rogers et al.*, 1998], due to the relative summer weakness of North Atlantic features such as the Icelandic Low. Stronger wintertime circulation controls were also observed in the Mt. Logan snow accumulation [*Moore et al.*, 2002; *Rupper et al.*, 2004].

These seasonal differences have important implications for the analysis of ice core $\delta^{18}O$, which, in most studies, are conducted using annually-averaged data. In the case of the Mt. Logan ice cores, the inclusion of weakly-controlled summer values in taking an annual

average could mute any strong controls present during the winter. Use of a winter-only $\delta^{18}O$ record from the ice core may lead to more consistent relationships between the isotopic records and paleoclimate reconstructions from other sources such as AL strength from tree-rings, and enhance reconstructions of winter-only teleconnections such as the PNA using the ice core record.

In interpreting these circulation controls in a paleoclimatic context, we therefore found no evidence that the 1840s to 1850s shift towards lower $\delta^{18}O$ values observed at Mt. Logan and Jellybean Lake was associated with a strengthening of the AL. Rather, our results suggest that the dominant effect of a deepened AL is to reduce isotopic depletion during transport to the SW Yukon. Physically, the higher precipitation $\delta^{18}O$ in the SW Yukon under these conditions could be attributed to several processes, namely: enhanced evaporative recharge or reduced rainout along a more southern path, increased mixing with less isotopically-depleted air masses [*Alley and Cuffey*, 2001], or weaker isotopic fractionation under warmer conditions. Although there is likely some entrainment of sub-tropical moisture, the observational analysis of *Zhu et al.* [2007], for example, showed no cyclones originating south of 30°N; the *Fisher et al.* [2004] association between stronger AL with lower $\delta^{18}O$ is possibly due to an unrealistically large contribution of tropical moisture.

There is also the possibility that the mid-19th century shift can be explained not by a change in the AL strength, but rather by a change in precipitation seasonality. While we can not fully exclude this, we do note that the controls identified here are consistent with the north Pacific circulation reconstruction of *D'Arrigo et al.* [2005], and other types of evidence during the mid 19th century. Observational analyses during the instrumental period have shown that a stronger AL is also associated with warmer temperatures over Alaska [*Mock et al.*, 1998] and northwestern North America in general [*Trenberth and Hurrell*, 1994], which was observed consistently in controls on temperature and precipitation inferred from our GCM analysis. If a mid-19th century deepening of the AL had occurred, it would have presumably been accompanied by warmer regional temperatures, but independent paleoclimate records exist in the region which show no such shift. Land-based glaciers in the Gulf of Alaska region underwent a period of

advance during the last half of the 19th century in Southern Alaska, thought to indicate persistently cooler temperatures [*Calkin et al.*, 2001; *Wiles et al.*, 2004]. In addition, tree-ring based reconstructions of January-September temperature across the entire Gulf of Alaska region showed a significant cold shift in the 1840s [*Wilson et al.*, 2007]. Furthermore, there is an apparent increasing trend in the Logan $\delta^{18}O$ since the mid 20th century, which, under the controls identified here, would be consistent with the trend towards a deeper wintertime AL observed over the same period [*Bograd et al.*, 2002].

4.5 Conclusions

Our GCM analysis of circulation controls on the SW Yukon $\delta^{18}O$, when considered alongside other paleoclimatic evidence, suggests that the observed shift in the middle of the 19th century was associated with a weakening of the AL and weakened southerly moisture transport. An associated cooling in the Gulf of Alaska region would contrast with the shift towards warmer conditions seen across much of the rest of the Arctic [*Smol et al.*, 2005], illustrating the importance of considering regional changes in paleoclimatic reconstructions [*Jones and Mann*, 2004]. A similar phenomenon was found in modeling the temperature difference between the late 17th and 18th centuries, when emergence from the Maunder Minimum corresponded to a widespread winter-warming across the Northern Hemisphere, with the exception of the Gulf of Alaska and North Atlantic regions, which exhibited significant cooling [*Shindell et al.*, 2001]. The Gulf of Alaska, in particular, would appear to be a region where inter-decadal temperature changes are frequently out of phase with those across the North American and Eurasian land masses.

Chapter 5
The effects of post-condensation exchange on the isotopic composition of water in the atmosphere

5.1 Introduction

Dansgaard [1954] identified three controls on the isotopic composition of atmospheric moisture: the temperature of surface evaporation, the origin of the vapor, and the amount of previous rainfall from the air mass. As discussed in Section 1.4, the subsequent Rayleigh distillation model of *Dansgaard* [1964] is the most important concept in isotope hydrometeorology, and explains much of the observed spatial variation in the isotopic composition of precipitation. Rayleigh models have been widely used to interpret isotopic observations, but regardless of their complexity, these models assume the immediate removal of condensate once it has formed [*Jouzel et al.*, 1997], locking in the isotopic composition of precipitation. One factor complicating this assumption is the post-condensation exchange (PCE) that occurs between condensate and vapor, as described in Sections 1.5 and 1.8.2. Re-evaporation and atmospheric moisture recycling are often invoked to explain deviations between $\delta^{18}O$ observations and simple Rayleigh-type model predictions [*Brown et al.*, 2008; *Feng et al.*, 2009], or to explain uncertainty in a relationship between a climatic variable of interest and $\delta^{18}O$ [*Etien et al.*, 2008]. Furthermore, through the detailed diagnosis of an isotopically-equipped single column convective model, *Risi et al.* [2008] identified PCE as the most important factor contributing to the rainfall 'amount effect', the negative relationship between precipitation amount and its isotopic composition [*Rozanski et al.*, 1993].

The importance of PCE on the isotopic composition of precipitation at a global scale has not been assessed, but significant steps have been made recently in understanding its role on vapor isotopes, with analyses of vapor δD measurements from satellites and experiments using isotopically-equipped general circulation models (GCMs). *Worden et al.* [2007] found that over the tropical lower troposphere, δD measurements from the Tropospheric Emissions Spectrometer (TES) satellite instrument were lower than would

be expected from Rayleigh distillation. Using an idealized model of vapor isotopic composition, *Worden et al.* [2007] were able to explain these observations using different rates of rainfall re-evaporation. *Brown et al.* [2008] subsequently examined tropical continental convection regions in detail, and suggested that the occurrence of overly depleted δD observations was attributable to intensive upstream moisture recycling. Using experiments with an atmospheric GCM equipped with stable water isotope tracers, *Wright et al*. [2009] found that with condensate evaporation and equilibration removed, the δD composition of vapor was enriched by up to 50 ‰, constituting a non-negligible proportion of vapor depletion attributable not to Rayleigh depletion, but rather to PCE, consistent with the vapor recycling hypotheses used to explain the depleted TES measurements.

Following these studies, the goal of this work was to further quantify the effects of PCE on precipitation and vapor isotopes using the isotopically-equipped GISS ModelE GCM. Many GCM-based studies have examined the relationship between $\delta^{18}O$ and different meteorological parameters, such as local temperature [*Hoffmann et al.*, 1998; *Cole et al.*; *Noone and Simmonds*, 2002; *Vuille and Werner*, 2005; *Schmidt et al.*, 2007], regional moisture balance [*Lee et al.*, 2007], or atmospheric circulation [*Werner and Heimann*, 2002; *Vuille and Werner*, 2005; *Schmidt et al.*, 2007; *Field*, 2010]. Although GCM-based, these studies are similar to observational analyses in diagnosing controls on isotopic composition from a control simulation, and not experimental in the sense of systematically manipulating certain processes within the model, or by varying external forcings.

5.2 Experimental design

The control run (CTRL) was that from Chapters 3 and 4, with all isotopic processes enabled, and was comparable to the ModelE control runs of *Schmidt et al.* [2005] and *Wright et al.* [2009]. The INIT run was an experimental simulation with atmospheric fractionation occurring during initial condensation only, and without any fractionation during PCE, namely equilibration or condensate evaporation, analogous to the "large-scale with super-saturation" (LSC-SS) run of *Wright et al.* [2009]. As in that study, we interpret the INIT run as a Rayleigh distillation model, but with realistic advection and

mixing of moisture. We took a slightly different approach than the *Wright et al.* [2009] experiments, where all tracer from re-evaporation was eliminated. In the INIT experiment, tracers are transferred between reservoirs, and therefore conserved, but with no fractionation and consequently with no isotopic signature left by PCE processes. As in *Wright et al.* [2009], the changes are limited to off-line tracers, and core prognostic quantities are identical across experiments, unlike 'on-line' re-evaporation experiments [*Bacmeister et al.*, 2006; *Maloney*, 2009] where changes to re-evaporation were applied to the core prognostic processes and can affect the model's dynamics through heat exchange as water changes phase.

The analysis was limited to first-order isotopic quantities, and excluded the second-order deuterium excess, which is not as well-simulated in ModelE. The analysis was focused on $\delta^{18}O$, but modeled δD was examined when comparing results to recent observational analyses of vapor δD. Direct comparison of the GCM results was made to precipitation $\delta^{18}O$ observations from GNIP. From the GNIP stations, only stations with 5 or more years worth of isotope data were used in the analysis. This GNIP data were supplemented with other data for under-sampled regions which had sub-annual resolution. Over Russia, recently available precipitation $\delta^{18}O$ data for 12 stations from *Kurita et al.* were included. Data were also included for Greenland, at the Summit [*Hastings et al.*, 2004] and NGRIP [*Shuman et al.*, 2001] sites, and for Antarctica at South Pole [*Aldaz and Deutsch*, 1967], Vostok [*Ekaykin*, 2003] and Law Dome [*van Ommen and Morgan*, 1997]. In total, there were data for 234 locations, 216 of which were from GNIP.

5.3 Results

5.3.1 Basic features of CTRL

The seasonal distributions of temperature and precipitation for CTRL are shown in Figure 5-1, both of which, as expected, were in good agreement with the moderate-resolution, 20-level (M20) simulations of *Schmidt et al.* [2006]. The annual mean surface air temperature was 14.3 °C (14.4 °C in their M20), the precipitation rate was 3.0 mm/day (2.96 mm/day in their M20), and the 847 hPa specific humidity q was 6.3 g kg^{-1} (6.5 g kg^{-}

[1]for their 850 hPa q). The mean annual precipitation $\delta^{18}O$ was -7.3 ‰, compared to their -7.5 ‰.

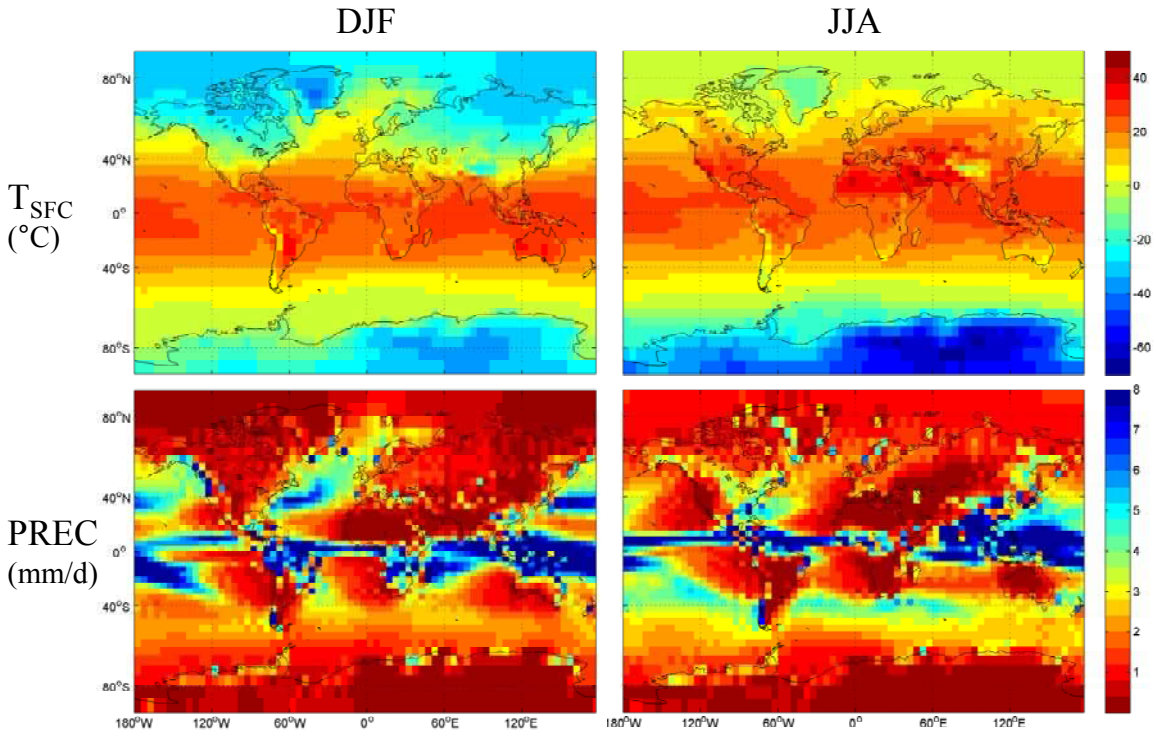

Figure 5-1. Seasonal surface air temperature and precipitation for CTRL.

Figure 5-2 shows the seasonal distribution of precipitation $\delta^{18}O$ for CTRL. The least depleted precipitation $\delta^{18}O$ occurs over the dry subtropical anticyclones, with values close to 0. At low latitudes, the most depleted precipitation $\delta^{18}O$ is associated with heavy rainfall (Figure 5-1), most notably the continental convective regions of northern South America and southern Africa during the DJF wet season. In absolute terms, the most depleted values occur over the polar ice caps, with a minimum of -61 ‰ over East Antarctica during JJA, and -37 ‰ over Greenland during DJF. The greatest precipitation $\delta^{18}O$ seasonality is observed over Greenland, Antarctica and the Eurasian and North American continental interiors, where the seasonal changes follow those in surface temperature (Figure 5-1). An exception to this seasonality is the Asian Monsoon region, which is 6 ‰ lower during JJA than DJF, despite being 10°C warmer.

Seasonal vapor $\delta^{18}O$ at the surface and in the mid-troposphere at 470 hPa are shown in Figure 5-3. The gradients in surface vapor $\delta^{18}O$ generally follow those of precipitation

$\delta^{18}O$, but the precipitation is greater by an average of 10 ‰, corresponding to the enrichment that occurs as the vapor condenses. The mid-tropospheric vapor $\delta^{18}O$ shows a further depletion from the surface vapor, and sharper low-latitude gradients between dry and humid regions. Throughout the troposphere, the vapor $\delta^{18}O$ exhibits a similar seasonal shift to that of precipitation $\delta^{18}O$, with increased depletion during the winter in each hemisphere (Figure 5-4).

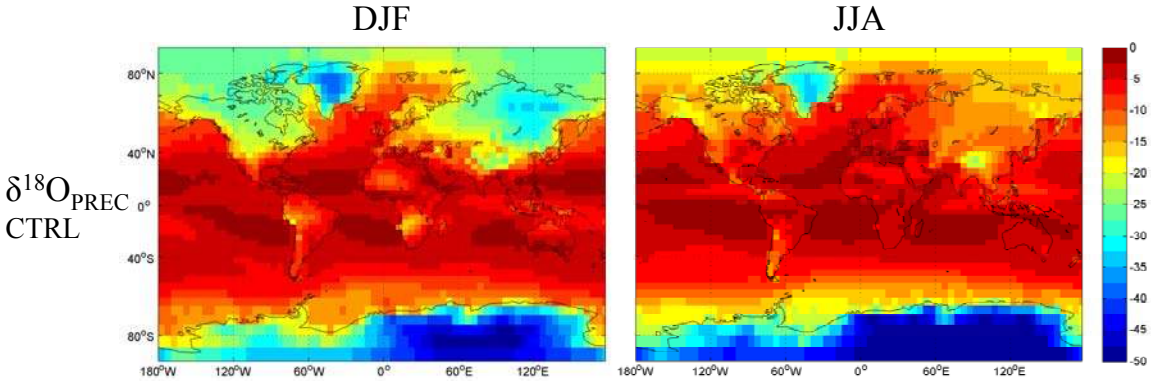

Figure 5-2. Seasonal $\delta^{18}O$ composition (‰) of precipitation for CTRL.

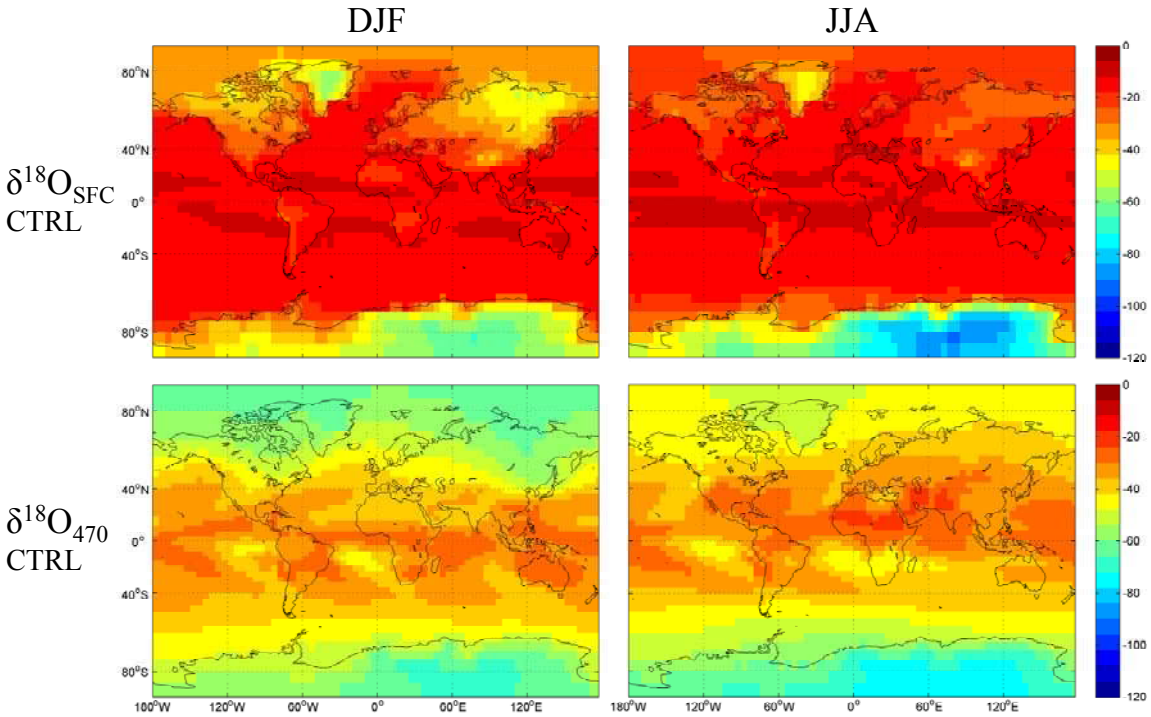

Figure 5-3. Seasonal $\delta^{18}O$ composition (‰) of surface (SFC) vapor and vapor at 470 hPa for CTRL.

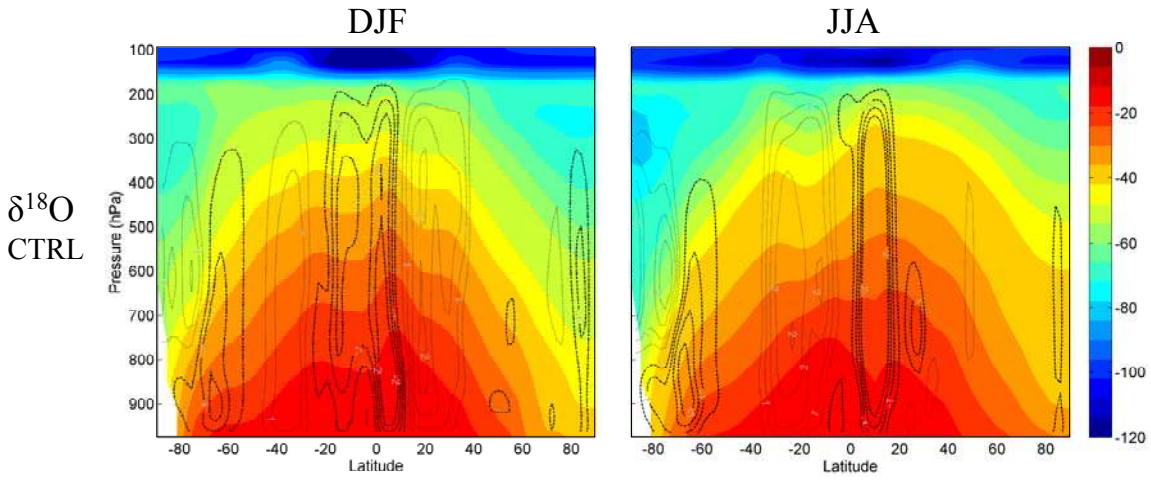

Figure 5-4. Mean zonal $\delta^{18}O$ of vapor (‰) for CTRL. Contours show vertical velocity ω (10^{-4} hPa/s), with dashed contours for upward motion (ω < 0), and dotted contours for downward motion (ω > 0).

5.3.2 Changes in $\delta^{18}O$ in the absence of PCE

Figure 5-5 shows the difference in precipitation $\delta^{18}O$ between INIT and CTRL. For DJF, in the absence of PCE, there is an increase in precipitation $\delta^{18}O$ over land at higher latitudes and over ice-covered ocean, and a net decrease over open-ocean and low-latitude land. Over land, the increases are relatively constant, reaching 7 ‰ over the North American interior and 5 ‰ over the Eurasian interior. At low latitudes, there is an inverse relationship between the magnitude of the decrease for INIT and precipitation amount (Figure 5-1). The strongest decreases of up to 8 ‰ occurred over the dry, subtropical anticyclones, and the weakest decreases over regions of heavy precipitation, reasons for which are discussed in detail in Section 4.4.

For surface vapor $\delta^{18}O$ (Figure 5-6) in INIT during DJF, there is an increase over land in the extra-tropics, and a weaker increase over ocean. At low latitudes, there are stronger increases in surface vapor $\delta^{18}O$ in regions of heavy precipitation, which over land extend into the mid-troposphere. In the mid-troposphere there is also a greater overall increase in SH than in NH, and the weakest increase for INIT is across the northern subtropics centred at 20°N.

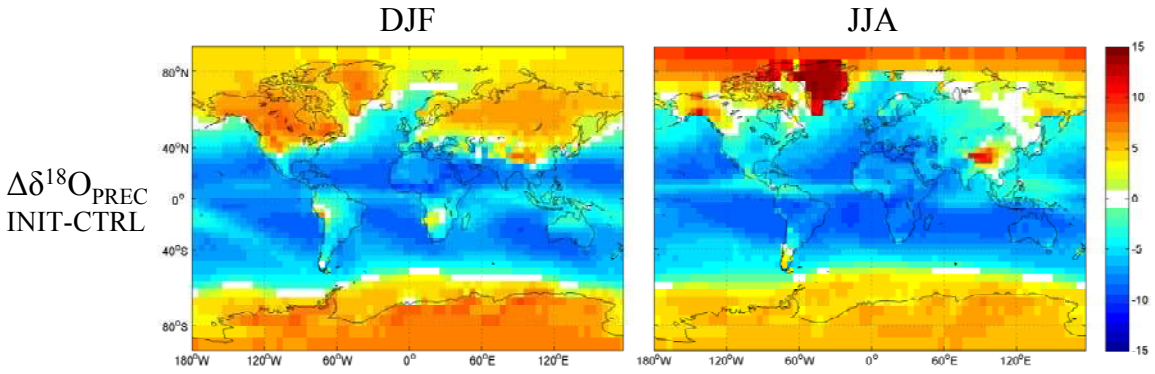

Figure 5-5. Change in $\delta^{18}O$ composition (‰) of precipitation for INIT from CTRL.

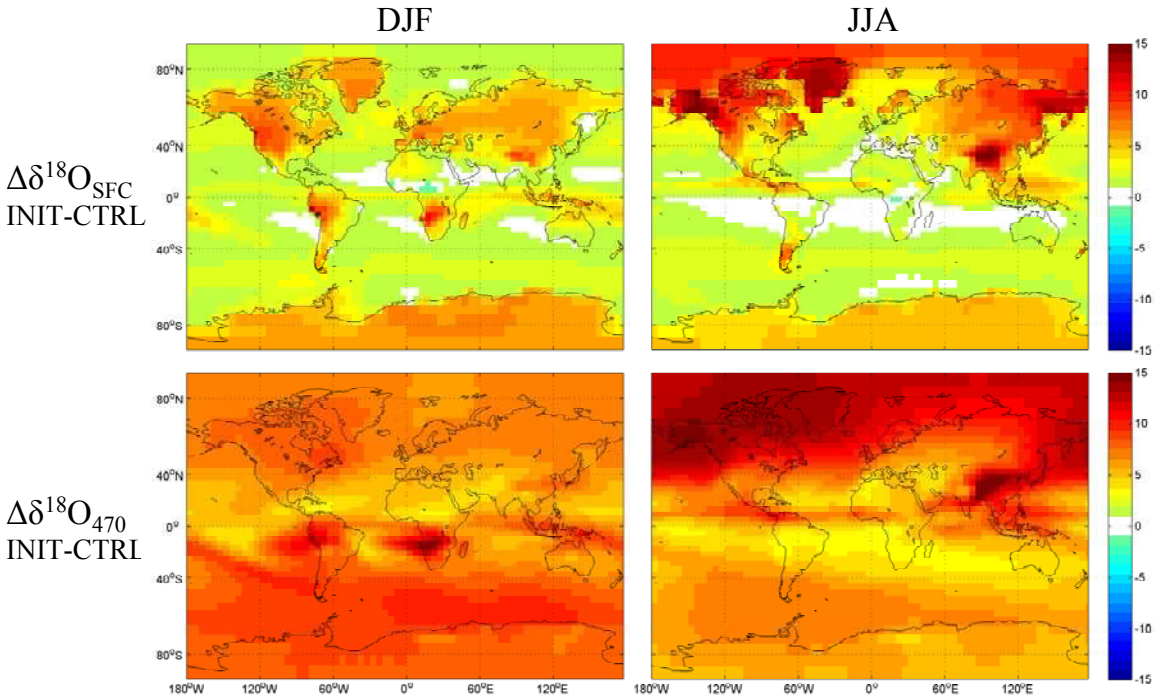

Figure 5-6. Change in vapor $\delta^{18}O$ composition (‰) for surface vapor and vapor at 470 hPa for INIT from CTRL.

For JJA, the high-latitude precipitation $\delta^{18}O$ increase in the NH has retreated poleward (Figure 5-5), replaced with a net decrease over much of Eurasia and North America. In several regions, however, the increase has become more pronounced. Over Greenland, for example, the JJA increase is 14 ‰, about twice the increase seen in DJF. The precipitation $\delta^{18}O$ increases in these regions are also seen in the $\delta^{18}O$ for surface vapor, and in the case of the Tibetan Plateau, the increase extends into the mid-troposphere (Figure 5-6). In the mid-troposphere in general, the mean vapor $\delta^{18}O$ increase for INIT in

the NH during JJA (8 ‰) is stronger than the southern hemisphere (SH) increase in DJF (6 ‰).

Figure 5-7 shows the zonal mean change in vapor $\delta^{18}O$ for INIT. The strongest increases in vapor $\delta^{18}O$ are in the extratropics, and shift seasonally with the warm season. The smallest increases for INIT are in regions of strongest seasonal descent (20°N during DJF, 20°S during JJA), low precipitation (Figure 5-1), and low relative humidity (RH) (Figure 5-8) in the subtropics. This was seen in the mid-tropospheric $\delta^{18}O$ difference (Figure 5-6), and the zonal mean plots show how these zonal minima extend through the troposphere and correspond to regions of subsidence.

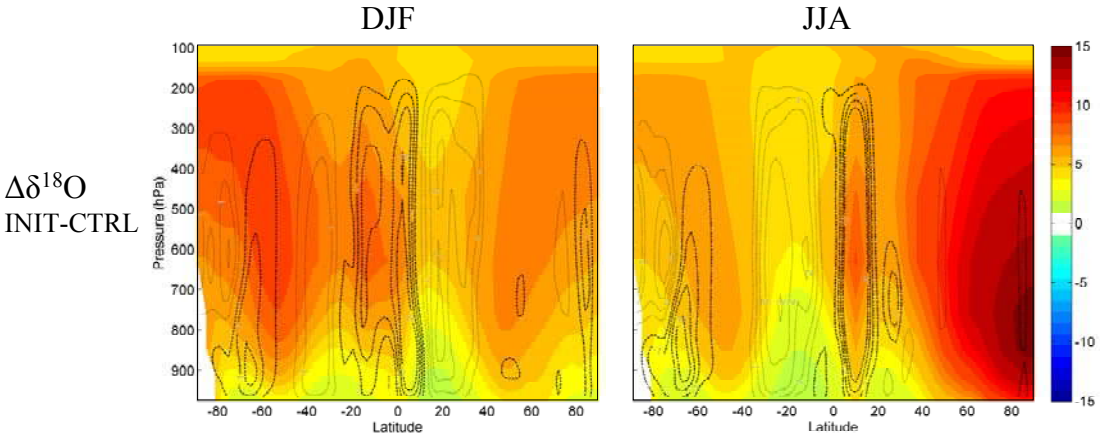

Figure 5-7. Zonal change in vapor $\delta^{18}O$ (‰) for INIT from CTRL. Contours are as in Figure 5-4.

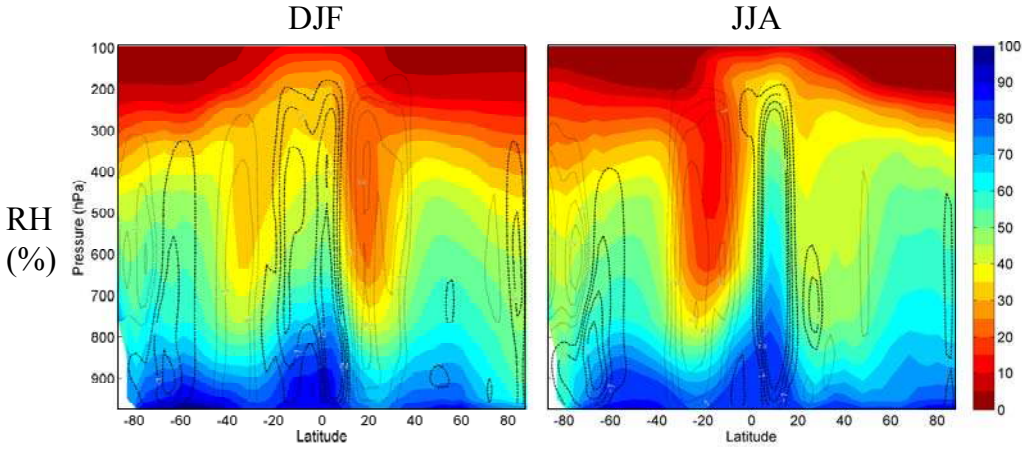

Figure 5-8. Zonal relative humidity (RH in %) for CTRL. Contours are as in Figure 5-4.

There were also large differences between modeled and observed precipitation $\delta^{18}O$ (Table 5-1, Figure 5-9) for the two experiments. For the CTRL run during DJF, there was a strong correlation of $r = 0.93$ between the precipitation $\delta^{18}O$ observations and that from the nearest grid cell in ModelE, with an overall model bias of -1.0 ‰ towards lower values, and a root-mean squared error (*RMSE*) of 3.2 ‰. For INIT, the correlation was reduced to $r = 0.81$, the bias increased to -2.5 ‰, and, most notably, the *RMSE* increased to 5.9 ‰. Similar changes were observed during JJA. During both seasons, the overall bias reflects a strong negative bias for precipitation $\delta^{18}O$ higher than -20 ‰, offset by the opposite bias for lower values. The correlations for CTRL and INIT were highly sensitive to the supplemental inclusion of cold region observations to the GNIP observations (Table 5-1), discussed in Section 5.2.

Table 5-1. Correlation (*r*), bias (*b*) and root-mean square error (*RMSE*) for the $\delta^{18}O$ observations and GCM experiments. The statistics across all observations include data for Antarctica, Greenland and Russia to supplement data from the 216 GNIP stations.

		All observations			GNIP only		
		r	***b* (‰)**	***RMSE* (‰)**	***r***	***b* (‰)**	***RMSE* (‰)**
DJF	**CTRL**	0.93	-1.0	3.2	0.89	-1.1	3.2
	INIT	0.81	-2.5	5.9	0.65	-2.9	5.8
JJA	**CTRL**	0.92	0.2	3.1	0.72	0.1	2.9
	INIT	0.88	-4.6	6.4	0.37	-5.1	6.2

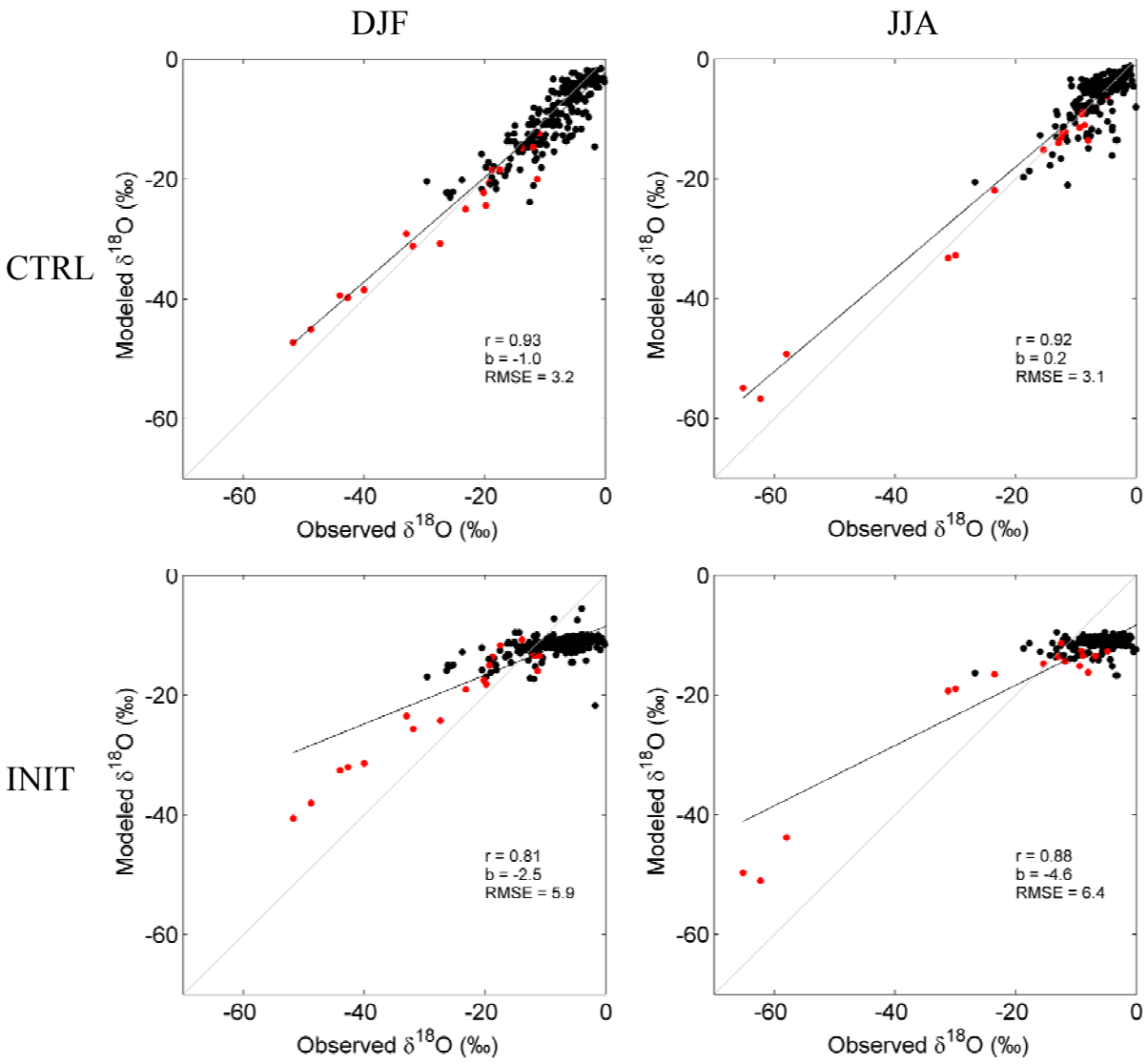

Figure 5-9. Correlation between observed and modeled precipitation $\delta^{18}O$ for CTRL and INIT. Observations are for 216 stations in the GNIP database (black circles), with supplemental data (red circles) from Antarctica, Greenland and Russia, as described in the text.

5.3.3 The temperature effect

Figure 5-10 shows the local correlation between anomalies of surface temperature (T) and precipitation $\delta^{18}O$ for all months of the year for CTRL, similar to many previous GCM studies. Only correlations with $|r| > 0.2$ and significant at the 95% level are plotted. There is a positive temperature correlation over extra-tropical land, and over some regions of equatorial South America and Africa. Absent from previous modeling studies at a global

scale [*Hoffmann et al.*, 1998; *Cole et al.*; *Noone and Simmonds*, 2002; *Vuille and Werner*, 2005; *Schmidt et al.*, 2007] is any seasonal separation of the temperature effect; much of the annual correlation map in Figure 5-10 is in fact the combination of a strong cold-season relationship and weak warm-season relationship (Figure 5-11). During DJF, the correlations are strong in the NH but weak in the SH over Antarctica. Over central Russia (50-60°N, 75-95 °E), for example, the median T-$\delta^{18}O$ anomaly correlation across grid cells was r = 0.37 for all months of the year, which increased to r = 0.60 during DJF, but weakened to r = 0.05 during JJA. For the INIT run (Figure 5-11), much of the NH DJF correlation is unchanged, with persistently strong correlations over the cold NH regions, with the exception of Europe and the US. During JJA, the weak positive temperature correlation over the continents seen for CTRL is absent for INIT. A band of negative correlation emerges around the Arctic, similar to that seen over the north Pacific and north Atlantic storm tracks during DJF, and over the southern Ocean during both seasons.

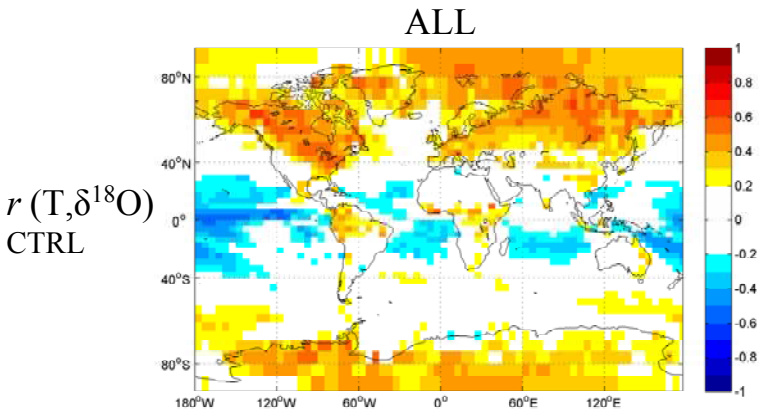

Figure 5-10. Correlation between surface temperature and precipitation $\delta^{18}O$ anomalies for CTRL, during all months of the year.

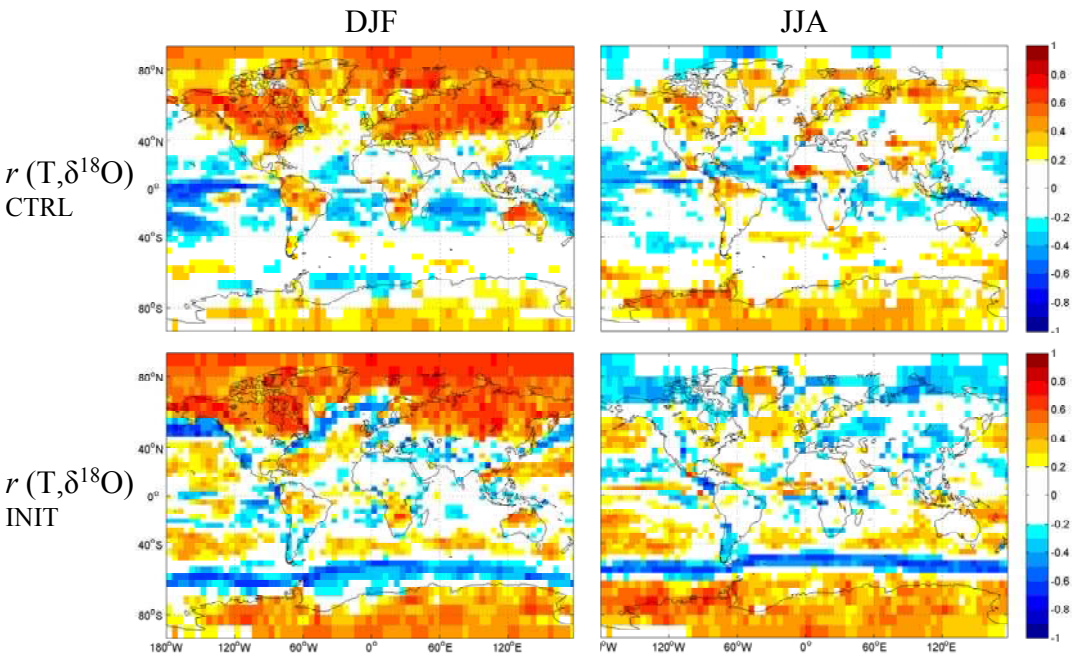

Figure 5-11. Correlation between surface temperature and precipitation $\delta^{18}O$ anomalies for CTRL and INIT, for different seasons.

5.4 Discussion

5.4.1 Global overview

The primary global feature of the precipitation $\delta^{18}O$ difference maps in INIT is the separation between regions of net increase and decrease in the absence of PCE (Figure 5-5). The increases at high-latitudes in INIT show where PCE has a net depleting effect, and the decreases at low latitudes show where PCE has a net enriching effect. A mechanistic explanation follows from *Gedzelman and Arnold* [1994] and *Risi et al.* [2008]. Partial re-evaporation of raindrops will enrich the raindrops, but transfer depleted vapor into the surrounding air. The situation is similar for raindrops equilibrating with vapor which is higher than that from which precipitation originally formed. If either type of PCE has occurred, subsequent condensate forming from this vapor reservoir will be lower than if PCE had not occurred. At a given precipitation site, therefore, condensate can be enriched by local PCE, but that may be exceeded by the depleted vapor reservoir from upstream PCE. What the INIT experiment does is separate the regions where any local enrichment from PCE is exceeded by upstream depletion from PCE.

In this regard, the phase of precipitation is critical: PCE occurs between vapor and liquid condensate but not between vapor and ice [*Friedman et al.*, 1962; *Rozanski et al.*, 1993; *Ciais and Jouzel*, 1994; *Pierrehumbert*, 1999; *Gonfiantini et al.*, 2001; *Friedman et al.*, 2002; *Tian et al.*, 2003; *Celle-Jeanton et al.*, 2004; *Sturm et al.*, 2010]. When solid condensate forms and falls as precipitation, there is no enrichment from local PCE, only the vapor-depleting effects from any PCE for upstream precipitation that occurred as liquid. To see the importance of the phase of precipitation, Figure 5-12 shows the fraction of precipitation that falls as snow for DJF and JJA. Particularly for DJF, the transition from rain- to snow-dominated precipitation across 40°N provides a strong demarcation in the INIT run between regions of low-latitude net precipitation $\delta^{18}O$ decrease and high-latitude net increase (Figure 5-5). Equatorward of this transition zone, rainfall will exchange isotopically with freshly evaporated ocean water, whereas poleward of this transition zone, the depleting effects of PCE on vapor $\delta^{18}O$ have been locked in.

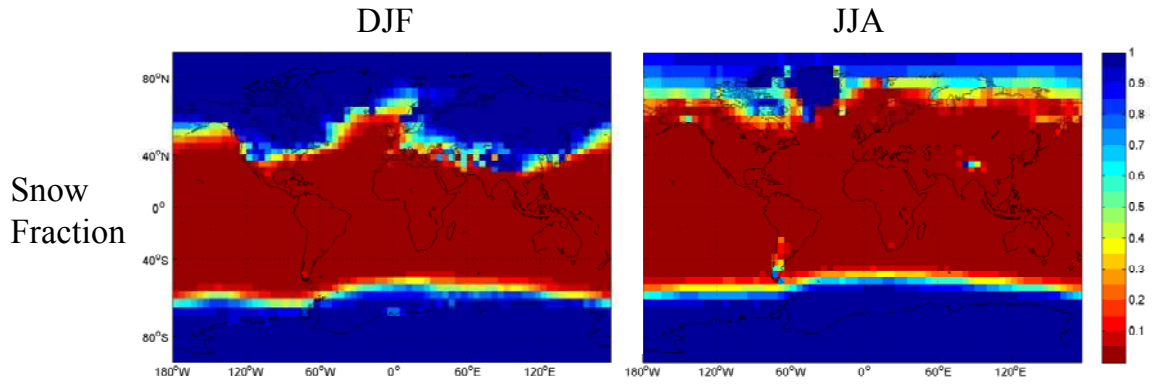

Figure 5-12. Fraction of precipitation which falls as snow for CTRL.

Unlike precipitation $\delta^{18}O$, vapor $\delta^{18}O$ always increased for INIT (Figure 5-6), as was seen in *Wright et al.* [2009] for δD. The zonal structure of the vapor $\delta^{18}O$ increases for INIT reflect basic features of the mean zonal circulation during different seasons (Figure 5-7) and also precipitation phase. The strongest vapor $\delta^{18}O$ increase for INIT during DJF is in the southern extra-tropical free-troposphere, with an increase of ~10 ‰ between 300 and 400 hPa poleward of 40°S. In the NH, the positive $\delta^{18}O$ anomaly for INIT is largely constant poleward of 40°N, and weaker than in the SH. At these latitudes in the NH, vapor depletion from PCE has occurred during liquid phase precipitation in the low-mid latitudes, and becomes locked in at the transition to snow-dominated precipitation, resulting in little zonal gradient poleward of 40°N. Over the tropics, the maximum in the mid-troposphere increase for INIT in the ascending region between 0° and 20°S is associated with the vigorous moisture exchange of the tropical rainfall belts. In the descending region centred on 20°N, the increase in vapor $\delta^{18}O$ for INIT is weakest near the surface, where the air is humid (Figure 5-8) and dominated by isotopically fresh evaporate from the ocean surface. This difference increases above the boundary layer to ~5 ‰ at 500 hPa, which reflects the mixing of air into the subtropics from subsidence, equatorward return flow, and convective detrainment [*Pierrehumbert*, 1998], which has undergone more upstream post-condensation vapor depletion.

During JJA, the structure of the zonal mean change for INIT mirrors that during DJF. At low latitudes, the increase in vapor $\delta^{18}O$ for INIT in the convective region is of the same magnitude, but has shifted to 10°N and is more zonally concentrated, corresponding to the more narrow band of tropical precipitation (Figure 5-1). The region of weak $\delta^{18}O$

increase in the lower troposphere for INIT is now centred near 20°S under the descending branch of the circulation. There is a much stronger JJA increase in the NH extratropics than seen in the SH during DJF, due to the more poleward shift in the snowline (Figure 5-12), and consequent increase in PCE over the NH. In this respect, we note that the peak of the annual-mean NH increase in *Wright et al.* [2009] over the North Pole in their LSC-SS experiment was a muted version of the JJA increase in Figure 5-7.

For CTRL, the agreement between the GCM and observations of precipitation $\delta^{18}O$ is excellent (Figure 5-9). For less depleted observations (> -20 ‰), there is an even distribution about the 1:1 line, indicating little systematic bias (-1.3 ‰ for DJF, 0.1 ‰ for JJA) in the GCM. Common to both seasons, however, is bias towards too-high values(4.3 ‰ for DJF and 8.2 ‰ for JJA) over Antarctica. This could reflect the paucity of cold-region observations, but is likely genuine, having been detected in previous isotopically-equipped GCM analyses over Antarctica [*Jouzel et al.*, 1997] and attributed to the general warm bias of the GCMs [*Masson-Delmotte et al.*, 2008]. For INIT, the separation of regions dominated by Rayleigh distillation and PCE emerges. For observed precipitation $\delta^{18}O$ values > -15 ‰, modeled precipitation $\delta^{18}O$ is too low, with only a weak slope. For observed precipitation $\delta^{18}O$ values < -20 ‰ , there is a constant under-depletion bias in the GCM, but a strong Rayleigh-driven slope. As in Figure 5-5, the difference for INIT has been locked in poleward of the snowline (Figure 5-12), represented by the positive offset and absence of a decreasing gradient below the snow line.

The strong correlations between the GCM and observations were highly dependent on the inclusion of the Antarctic and Greenland data, particularly during the boreal summer (Table 5-1). Without these observations, the JJA correlation was reduced to $r = 0.72$ for CTRL, and $r = 0.37$ for INIT: in the absence of data from strong Rayleigh depletion regimes, the contributions of PCE are much more important in explaining the observed variation of precipitation $\delta^{18}O$. Furthermore, and as *Vuille et al.* [2005b] stated, such a comparison should be taken cautiously given the uneven spatial distribution of GNIP stations, differences in the period and length of reporting, and mix of observation types between snow gauges, snow pits, and shallow cores.

The changes for INIT varied strongly across different climate regimes and seasons, and are examined in the following sections for the wet tropics, the dry sub-tropics, the Asian monsoon region and the extra-tropics.

5.4.2 Regional comparisons

5.4.2.1 Wet tropics

At low latitudes, the spatial variation of the decrease in precipitation $\delta^{18}O$ (Figure 5-5) results from differing effects of PCE aloft and at the surface. In the convective column, PCE will tend to deplete precipitation through recycling of re-evaporated and equilibrated vapor, as described in the detailed single-column analysis of *Risi et al.* [2008]. At the surface, by contrast, PCE will tend to enrich precipitation via exchange with fresh, less depleted vapor than that aloft. The uniform decrease in precipitation $\delta^{18}O$ for INIT reflects the PCE with this relatively undepleted surface vapor, but is offset to some degree in heavy precipitation regions by vapor recycling. The weaker effect of PCE for heavy precipitation is also consistent with the suggestion [*Lee et al.*, 2007; *Scholl et al.*, 2009] that heavy precipitation, with its larger-diameter raindrops, will undergo less exchange than lighter raindrops, and therefore undergo less enrichment via PCE with surface evaporate. Furthermore, we can see that the weak increase in precipitation $\delta^{18}O$ for INIT occurs over land over southern Africa and northwestern South America during DJF, where the surface evaporate $\delta^{18}O$ is lower than that over the ocean, limiting the enriching effects of PCE on condensate. In these regions, there are, in fact, isolated grid cells for which a net decrease in precipitation $\delta^{18}O$ occurs for INIT, reflecting the dominance of depletion from recycling in the column over enrichment near the surface.

The depleting effects of PCE in the column are seen more clearly in the changes to vapor $\delta^{18}O$ for INIT, particularly over southern Africa and northwestern South America during DJF (Figure 5-6). In these regions, the increase in vapor $\delta^{18}O$ extended through to the mid-troposphere over the continental 'tropical chimneys', and reflects the intensity of deep convection and recycling in those regions. We note also that when the 470 hPa vapor $\delta^{18}O$ difference maps of Figure 5-6 are averaged annually (not shown) (tom suggested including these, but they can be easily inferred from the seasoal maps), the

peaks in vapor $\delta^{18}O$ increases over northwestern South America and equatorial Africa in the mid-troposphere were similar to the locations of air parcel dehydration identified in the upper troposphere by *Dessler and Minschwaner* [2007].

The changes in vapor isotopes over the tropics can also be compared to interpretations of δD measurements from TES in the lower free troposphere. Across the tropics, *Worden et al.* [2007] observed that δD observations under moist conditions were lower than would be expected from strict Rayleigh distillation. Figure 5-13 shows a q-δD plot for the tropics for all months of the year for data from CTRL, analogous to the q-δD plots and re-evaporation-enabled model curves of *Worden et al.* [2007]. For CTRL, there are two branches to the distribution. For $q < 5$ g/kg, there is Rayleigh-like depletion with decreasing q, but for $q > 5$ g/kg, the opposite relationship appears: δD becomes lower with increasing q. *Worden et al.* [2007] observed a similar distribution, albeit with the two branches less apparent presumably due to their use of instantaneous observations rather than the monthly means examined here. In their analysis, the high-q, non-Rayleigh branch was explained by incorporating a condensate re-evaporation term into their analytical model, and the lower δD values were attributed to intensive within-atmosphere moisture recycling.

The q-δD distribution for the INIT experiment in Figure 5-13 is similar to the bounds set by the study of *Worden et al.* [2007], which included atmospheric mixing and Rayleigh distillation. On average, the δD values were 48 ‰ higher for INIT than for CTRL. More notable was the tighter fit to a Rayleigh-like q-δD curve for INIT. That is, in the absence of PCE, the extra-Rayleigh branch of the distribution associated with the more humid values and intensive moisture recycling is absent. This provides GCM-based support to the interpretation of *Worden et al.* [2007], which was based on an idealized box model with re-evaporation.

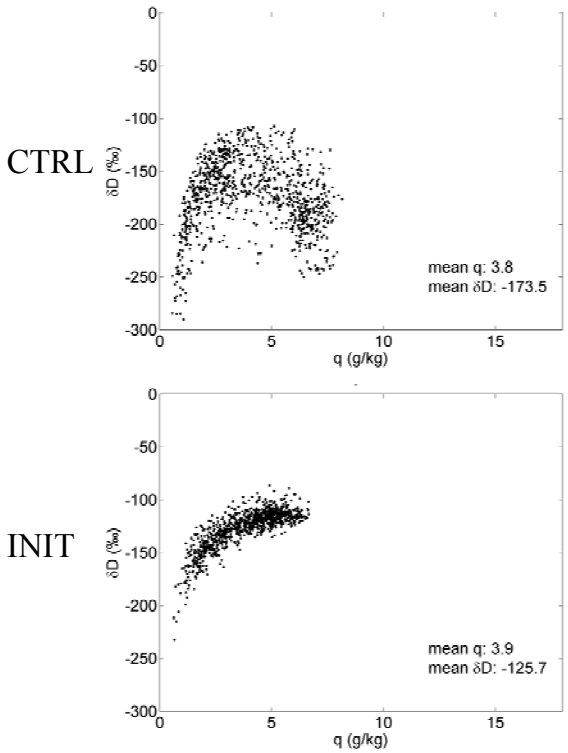

Figure 5-13. *q*-δD plots for the tropics, defined as between 20°S and 20°N, for CTRL and INIT during all months of the year, following *Worden et al.* [2007]. GCM data were averaged between 847 and 470 hPa, with mass-weighting.

5.4.2.2 Dry subtropics

At low latitudes, the largest precipitation $\delta^{18}O$ decrease, of ~8 ‰, for INIT occurred over the dry-subtropical regions (Figure 5-5), representing an enriching effect of PCE on precipitation $\delta^{18}O$. This can be explained by the strong equilibration between the light, small-radius droplets falling through the humid and highly enriched surface layer, as has been previously suggested [*Lee et al.*, 2007]. Conversely, one can see that PCE has less effect on the vapor $\delta^{18}O$ at the surface (Figure 5-6); although the PCE has a strong enriching effect on the precipitation that does occur, there is simply too little condensate forming to substantially reduce the $\delta^{18}O$ of the ambient vapor, in contrast to the situation in the wet tropics.

The subtropical changes to vapor without PCE can also be compared with the vapor δD measurements over Hawaii for late July 2006 reported by *Galewsky et al.* [2007], which represent an intermediate regime between the wet and dry tropics. In that study, in-situ

vapor measurements of δD were taken between sea-level and 4205 m, and interpreted using a model (MATCH) with realistic moisture transport, condensation and isotopic fractionation, but which excluded detailed microphysical processes such as PCE. The model predictions spanned the observations, but with the model also tending toward higher δD values. Figure 5-14 shows mean modeled *q* and δD distributions over the Hawaii region for July and August, along with the Mauna Kea observations, and *q*-δD curves for the GCM experiments here. For CTRL, the GCM tended towards slightly higher δD values, particularly over the transition between the boundary layer and troposphere. This bias, however, increased significantly in the absence of PCE for the INIT run. The comparison of the mean GCM profiles to this limited set of instantaneous observations is imperfect, but the consistency with which the INIT and MATCH models produce more under-depleted vapor does support the contribution of PCE to vapor depletion. We note also that subsequent observations accounting for post-measurement isotopic exchange had values lower than reported by *Galewsky et al.* [2007], which could reduce the difference between CTRL and measured vapor δD in Figure 5-14 (J. Galewsky, pers. comm.).

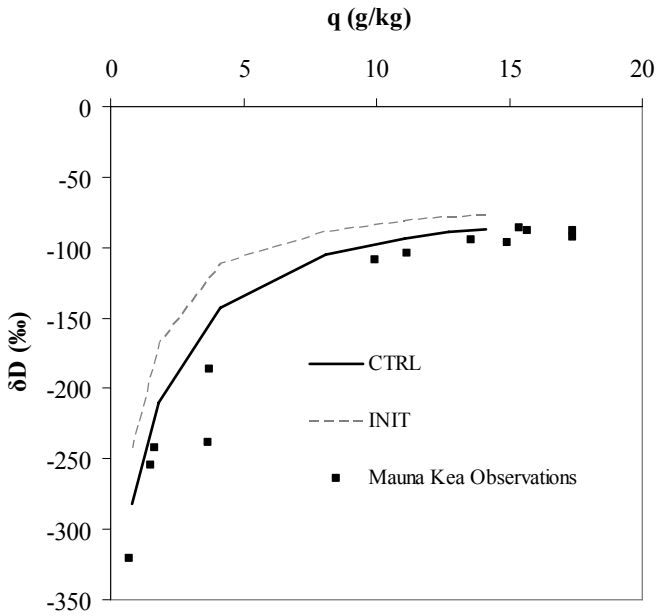

Figure 5-14. *q*-δD profiles over Hawaii for CTRL and INIT between the surface and 470 hPa, with Mauna Kea observations from *Galewsky et al.* [2007], which fell between the surface and 615 hPa.

There were also signatures of PCE in the dry, subtropical anticyclones downstream from the continental convective regions during DJF over the Amazon and southern Africa discussed in the previous section. The air detrained from the mid-tropospheric convective outflow is relatively moist, but heavily depleted, and, by mass, therefore has a substantial isotopic signature when entrained into the dry air. The total contribution of continental, convective outflow to the subtropical moisture is not well-constrained, but has been identified as one of three major atmospheric contributors to moisture in these regions, along with equatorward return flow and subsidence [*Pierrehumbert*, 1998]. Furthermore, contributions of upstream moisture recycling to dry conditions have been described in the mesoscale. *Lawrence et al.* [2004] observed highly depleted vapor $\delta^{18}O$ downwind of organized convection in a high temporal-resolution in-situ sampling downwind of individual storm events, suggesting the depletion provided strong evidence for moisture recycling within the storms.

5.4.2.3 Asian monsoon region

The Asian Monsoon region has the world's "most complex patterns of spatial and temporal distribution of stable isotope composition of precipitation" [*Araguas-Araguas et al.*, 1998]. Over mainland Southeast Asia, southern China and the southern Tibetan Plateau, a succession of studies has shown that precipitation $\delta^{18}O$ is lower during summer than winter, opposite the region's temperature seasonality, and the isotope seasonality across the rest of the NH. Under sufficiently strong monsoon conditions, this pattern can extend as far as the North China Plain [*Yamanaka et al.*, 2004], eastern Mongolia [*Sato et al.*, 2007] and the western Tibetan plateau [*Tian et al.*, 2007]. Further north, the regular seasonality resumes, with lower winter and higher summer precipitation $\delta^{18}O$ [*Yamanaka et al.*, 2007; *Yu et al.*, 2007]. The transition between these two regions is thought to represent the transition between the influence of the monsoon and mid-latitude westerlies [*Araguas-Araguas et al.*, 1998; *Tian et al.*, 2001; *Johnson and Ingram*, 2004; *Tian et al.*, 2007; *Peng et al.*, 2010].

In GCMs, the reverse seasonality across the southern region was seen at Hong Kong in ECHAM simulations [*Hoffmann and Heimann*, 1997] and in the global analyses of *Noone and Simmonds* [2002] and *Brown et al.* [2006]. Interannually, *Vuille et al.* [2005b]

found through a detailed diagnosis of monsoon circulation over the Indian Ocean that the JJA precipitation $\delta^{18}O$ declined with the strength of the monsoon circulation, which was attributed to stronger upstream convection and rainout.

This characteristic seasonality can be explained in a more mechanistic sense by the INIT experiment. For CTRL, the reverse seasonality is present (Figure 5-15), with a mean DJF-JJA difference of 5.9 ‰ in the southeast (SE) China domain, compared to –6.2 ‰ in the northwest (NW) China domain (Table 5-2), which are within the range of differences observed from GNIP data by *Araguas-Araguas et al.* [1998]. We note that this seasonality was not apparent over land in simulations using the initial isotopically-equipped version of the GISS model [*Jouzel et al.*, 1987], reflecting continual improvements in model resolution and cloud physics parameterization. Relevant changes for isotopes are the improved model resolution ($4° \times 5°$ and 20 vertical levels compared to $8° \times 10°$ and 9 vertical levels in *Jouzel et al.*), the use of second-order moments in calculating tracer advection [*Prather*, 1986] compared to the earlier use of linear-slopes only [*Russell and Lerner*, 1981], and the partial equilibration of convective precipitation compared to earlier full equilibration.

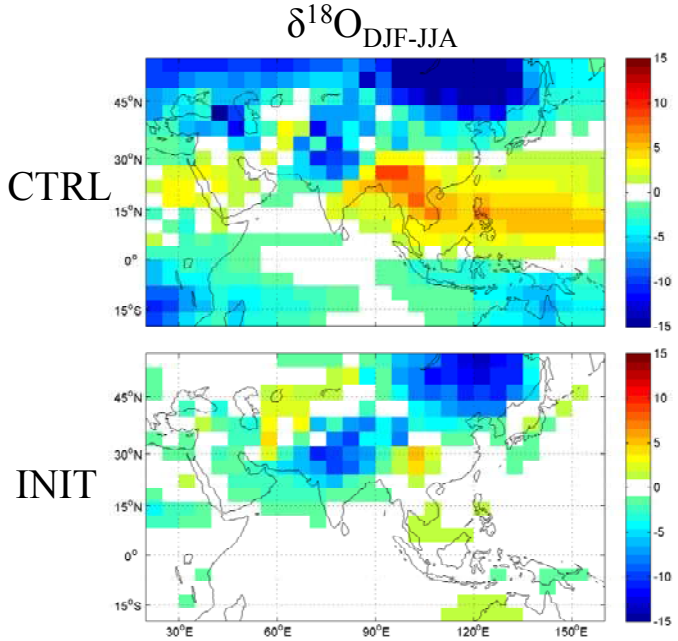

Figure 5-15. DJF – JJA precipitation $\delta^{18}O$ (‰), following *Araguas-Araguas et al.* [1998] and *Vuille et al.* [2005b], for CTRL and INIT.

Table 5-2. Seasonal changes in precipitation $\delta^{18}O$ (‰) for SE China (15-30 °N, 90-105 °E) and NW China (30-45 °N, 75-90 °E)

	CTRL			INIT		
	DJF	**JJA**	**DJF-JJA**	**DJF**	**JJA**	**DJF-JJA**
SE China	-7.0	-12.8	5.9	-10.4	-11.0	0.6
NW China	-20.5	-14.3	-6.2	-18.4	-12.8	-5.6

For INIT, the precipitation seasonality is largely absent across the SE China domain, with a DJF-JJA difference of only 0.6 ‰. That is, we can attribute this region's reverse isotopic seasonality to PCE, associated with vigorous moisture recycling in the intensive convection regions upstream. Over the NW China domain, by contrast, the absence of PCE for INIT had a much smaller effect, still with a DJF-JJA difference of -5.6 ‰, reflecting a weak monsoon influence over that region.

The isotopic features of the Asian monsoon region were examined for vapor δD from TES by *Brown et al.* [2008]. The instantaneous observations from their Asian Monsoon study region (15-30 °N, 80-100 °E) are shown in Figure 5-16 along with the monthly mean GCM data for the CTRL and INIT experiments over the same region. During the dry DJF season, there is a tendency toward lower δD with decreasing *q* in the TES δD. In *Brown et al.* [2008] the DJF observations were well-constrained by predictions from simple atmospheric mixing and idealized Rayleigh distillation, similar to those used in *Worden et al.* [2007]. This was not the case during the JJA monsoon season, where the moist observations fell below the Rayleigh curves, and in fact exhibited a weak tendency toward lower δD with increasing *q*. *Brown et al.* [2008] proposed that this extra-Rayleigh depletion was the result of upstream moisture recycling. We note also that *Herbin et al.* [2009] observed similar extra-Rayleigh depletion using satellite-based vapor δD measurements of a single major typhoon event in 2007 due east of the Asian Monsoon study region considered by *Brown et al.* [2008].

For the CTRL run during DJF (Figure 5-16), the modeled *q*-δD distribution is Rayleigh-like, with sharply depleting δD with decreasing *q*, consistent with the analytical model constraints of the observations in *Brown et al.* [2008]. The modeled values are less humid than the TES measurements, but with excellent agreement in the isotopic composition. During JJA, there is an opposite distribution, where δD decreases with increasing *q*. While this distribution is consistent with TES observations, the extra-Rayleigh depletion is more pronounced, and could indicate excessive vapor recycling in the GCM. During DJF in the INIT simulation, the *q*-δD values have a similar distribution as CTRL, but the mean δD is 32 ‰ higher than CTRL, indicating some contribution from PCE. During the wet JJA, however, the δD was 81 ‰ higher, and with no extra-Rayleigh branch. This indicates that moisture recycling indeed has an important role in isotopic depletion of vapor, but will require further investigation and comparisons against other satellite retrievals of vapor δD. *Lee et al.* [2009] found, for example, that the NCAR CAM3 GCM had lower vapor δD in the lower troposphere than the TES measurements, but absent in their study was the -5 % correction applied to HDO concentration by *Worden et al.* [2007] and *Brown et al.* [2008] to account for bias in the TES data. We note also that because of the coarse vertical resolution of the TES retrievals, the measurements reflect a free-tropospheric average rather than a true tropospheric profile. Therefore, in our analysis we vertically average the modeled fields between 470 and 847 hPa.

5.4.2.4 Extratropics

Strong seasonal effects of PCE were seen in the extra-tropics, and were strongly influenced by the transition from rain to snow-dominated precipitation. During DJF, there was an average increase of ~5 ‰ in precipitation $\delta^{18}O$ over NH land for INIT compared to CTRL (Figure 5-5). Spatially, the increase was relatively constant compared to the strong decrease towards the continental interiors for CTRL, which can be attributed to Rayleigh distillation. As the snow line moved northward during JJA (Figure 5-12), so did the transition from net decrease to net increase in precipitation $\delta^{18}O$ for INIT. Another contributing factor to the seasonal changes in effects of PCE is evapotranspiration from the land surface. Transpiration from vegetation acts as an unfractionated, and highly

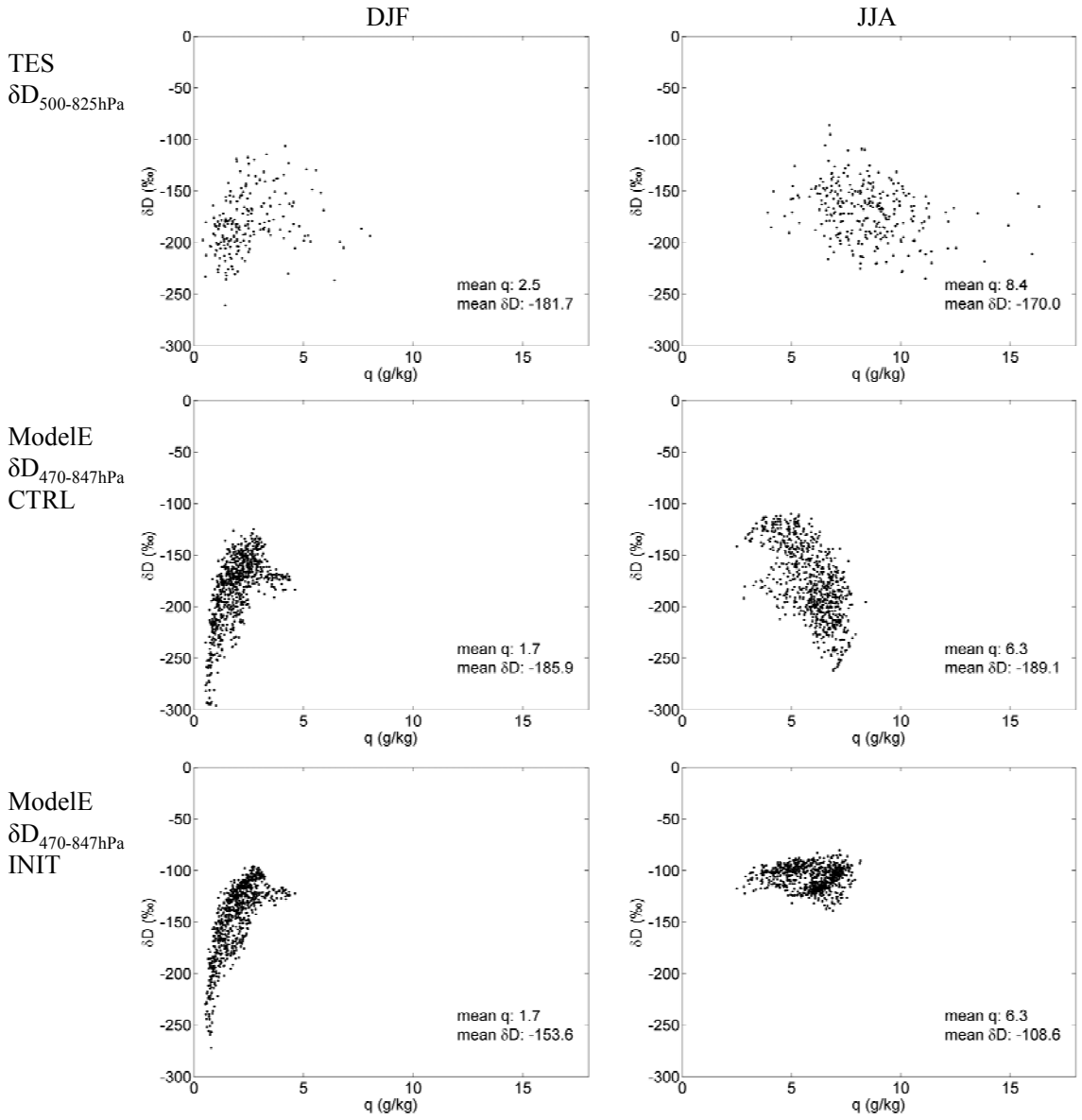

Figure 5-16. *q*-δD plots over *Brown et al.* [2008]'s Asian Monsoon region (15-30°N, 80-100°E) for TES, CTRL, and INIT. GCM data were averaged between 847 and 470 hPa, with mass-weighting.

enriched source of vapor [*Gat and Matsui*, 1991], and PCE with this vapor will highly enrich precipitation. Precipitation $\delta^{18}O$ for INIT undergoes a net decrease over much of North America and Eurasia during JJA when plant transpiration is active, but not during DJF.

Over Eurasia, up to 5 ‰ of the DJF precipitation $\delta^{18}O$ depletion was attributed to PCE (Figure 5-5), in addition to that from Rayleigh distillation. *Kurita et al.* [2004], however, found good agreement between a strict Rayleigh-based model of isotopic distillation similar to Eq. 1-4, with no significant under-depletion despite the model's lack of PCE. This can be explained by the fact that their model was initialized with observed isotopic values in western Russia where DJF precipitation predominantly occurs as snow [*Dai*, 2001]. That is, their initial values from observations were within the snowline and would have reflected any depletion that resulted from PCE from upstream liquid precipitation, over the Atlantic Ocean from which the moisture ultimately originates [*Kurita et al.*, 2004].

Sodemann et al. [2008] recently analyzed NAO controls on Greenland precipitation $\delta^{18}O$ using a trajectory-based model accounting for mixed-phase precipitation, but not PCE. They identified strong NAO controls on the precipitation $\delta^{18}O$, but also found that modeled values were 13-14 ‰ too high relative to observations from ice core data in southern central Greenland, which ranged from -35 to -38 ‰ during the winter months. They attributed the over-estimation to possible factors such as the delayed onset of condensation along a trajectory and insufficient orographic distillation. For CTRL, the GCM mean precipitation $\delta^{18}O$ during DJF of -37 ‰ accurately captured the observed values. For INIT, the DJF precipitation $\delta^{18}O$ over their site was 7 ‰ higher; half of their bias towards too-high $\delta^{18}O$ could possibly be explained by the absence of PCE in their model. During JJA, there was an increase in the INIT difference to 14 ‰ , which can be explained by the northward shift in the snowline (Figure 5-12). There is an increase in the amount of nearby upstream precipitation occurring as liquid, but the precipitation over the Greenland interior still occurs as snow. The increase in the amount of upstream liquid precipitation results in greater PCE-related $\delta^{18}O$ depletion of the vapor reservoir, with no local PCE-related enrichment.

5.4.2.5 Temperature effect

The most important isotopic phenomenon in the extra-tropics is the positive relationship between precipitation $\delta^{18}O$ and temperature, which forms the basis for paleo-isotopic reconstructions of temperature [*Dansgaard*, 1964] (tom had a point here that I didn't

quite agree with). Local correlation between temperature and precipitation $\delta^{18}O$ was first modeled by *Hoffman et al.* [1998], and subsequently by others over specific regions and using various isotopically-equipped GCMs [*Cole et al.*; *Noone and Simmonds*, 2002; *Vuille and Werner*, 2005; *Schmidt et al.*, 2007; *Risi et al.*, 2010]. We note first that the correlations between temperature and precipitation $\delta^{18}O$ anomalies during all months of the year in Figure 5-10 and in all previous studies can be viewed as the combination of a strong winter correlation and a weak summer correlation (Figure 5-11), extending the similar seasonal differences seen over Europe in Chapter 3 (Figure 3-5). This difference has not been identified in GCM studies, but has been in observational studies. Using observations pooled across Russia, for example, *Kurita et al.* identified a T-$\delta^{18}O$ correlation of $r = 0.48$ during DJF, which decreased to $r = 0.26$ during JJA.

The INIT experiment provides an additional mechanistic, and perhaps surprising, partitioning of the temperature effect during DJF. Over much of the extra-tropical NH, the temperature effect was unaffected by the absence of PCE (Figure 5-11). In these regions, the Rayleigh-distillation interpretation of the temperature effect would apply. Over central Russia for example, the DJF correlation for CTRL was $r = 0.60$, compared to $r = 0.54$ for INIT, consistent with, for example, *Kurita et al.*'s attribution of T-$\delta^{18}O$ anomaly correlations to Rayleigh distillation for seasons other than JJA.

This was not the case, however, over the US and Europe. Over central Europe (45°-55°N, 5°-20°E) the median DJF correlation across all grid cells was $r = 0.50$ for CTRL, consistent with the positive local correlations from previous studies [*Rozanski et al.*, 1992; *Baldini et al.*, 2008; *Field*, 2010]. For INIT, by contrast, the DJF correlation reduced to a statistically insignificant $r = -0.11$. We suggest that over these regions, the temperature effect is attributable to PCE, rather than Rayleigh distillation. The physical mechanism can be understood by noticing that the regions where the temperature effect is absent for INIT correspond to transition between liquid and solid-phase precipitation (Figure 5-12) which separated regions of net increase and net decrease in precipitation $\delta^{18}O$ for INIT. Warmer temperatures are associated with an increase in the proportion of precipitation falling as rainfall, which is locally enriched through PCE and will have higher $\delta^{18}O$ values. Colder temperatures are associated with more precipitation falling as

snow, which will not be locally enriched through PCE and have lower $\delta^{18}O$ values. That is, temperature controls the phase of precipitation, which, in turn, controls whether local enrichment through PCE occurs. This control exists only in regions where there is variability in the proportion of precipitation that falls as snow, seen in Figure 5-12.

Curiously, there was also the emergence of a band of significant negative T-$\delta^{18}O$ correlation for INIT over the oceans, particularly over the southern Ocean (Figure 5-11). That is, in the absence of PCE with highly enriched surface evaporate, pure Rayleigh distillation results in a negative temperature effect. This is because the fractionation factor for vapor to solid deposition is greater than that for vapor to liquid [*Majoube*, 1971a; b]. As a precipitating air mass transitions from rainfall to snowfall, the precipitation $\delta^{18}O$ undergoes a ~2 ‰ increase simply due this transition in phase (Figure 1-2). This acts as a discrete, step-wise influence over the condensation $\delta^{18}O$ at the point where rain turns to snow, with an increase in condensate $\delta^{18}O$ incurred simply via the temperature-controlled transition to snowfall. For CTRL, where PCE is present, this effect is masked by the opposite depleting effect of the lack of PCE enrichment during snowfall.

Given the importance of the transition from rain- to snow-dominated precipitation, we conducted follow-up diagnoses to determine the extent to which $\delta^{18}O$ variability could be explained, more directly, by the phase of precipitation. Figure 5-17 shows the DJF correlation between precipitation $\delta^{18}O$ and the fraction of snow falling as precipitation. For CTRL, there is indeed a strong negative correlation between the proportion of precipitation falling as snow and precipitation $\delta^{18}O$; higher snow fraction is associated with less enrichment from PCE and, as a result, lower $\delta^{18}O$. For INIT, this effect is absent, and regions of positive correlation emerge, which are associated with the higher fractionation factor for the vapor-snow change of phase relative to the vapor-liquid change of phase.

Thus, the broad extra-tropical bands of positive temperature correlation seen during DJF in Figure 5-11 are in fact the superposition of two correlation patterns with distinct underlying mechanisms: Rayleigh distillation, and PCE. The European case is interesting

because of the availability of high-quality precipitation $\delta^{18}O$ data from the GNIP network,

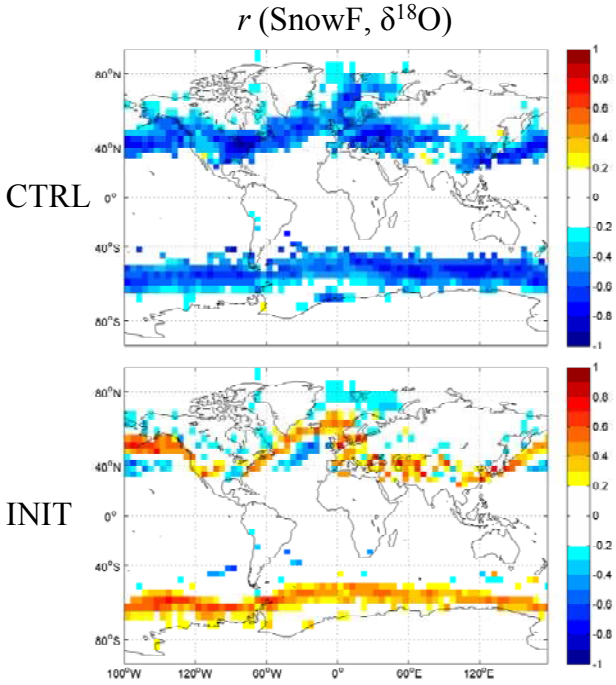

Figure 5-17. DJF correlation between anomalies of precipitation $\delta^{18}O$ and fraction of precipitation which falls as snow for CTRL and INIT.

which has resulted in a succession of studies over the region, as discussed and examined in Chapter 3. Implicit in these studies was an assumption that the observed temperature effects were the result of Rayleigh distillation; higher $\delta^{18}O$ was associated with less upstream Rayleigh distillation, which was in turn influenced by characteristic patterns of atmospheric circulation. The results of the INIT experiment suggest an alternative mechanism: during DJF the temperature effect is governed by variability of precipitation falling as rain or snow, via the occurrence or not of PCE.

5.5 Conclusions

In this study, we have quantified the effects of post-condensation exchange on precipitation and vapor isotopes using a GCM. PCE is universally acknowledged as an important influence on precipitation $\delta^{18}O$, but this was the first study to quantify its contributions on a global scale.

The key findings of the study were:

1. PCE will deplete vapor $\delta^{18}O$, as was seen in *Wright et al.* [2009], and this depletion is greater in regions of heavy precipitation.
2. At low latitudes, PCE tends to increase precipitation $\delta^{18}O$ via exchange with fresh surface evaporate, but can be offset by vapor depletion associated with intensive atmospheric recycling, following *Risi et al.* [2008]. At high latitudes, any local precipitation enrichment can be exceeded by upstream depletion of the vapor reservoir.
3. The low and high latitude regimes are separated by the transition from rain- to snow-dominated precipitation. Precipitation falling as snow is subject to upstream depletion via PCE, but undergoes no local enrichment.
4. The reverse isotopic seasonality associated with the 'amount effect' observed in the Asian Monsoon region can be attributed to PCE, presumably via intensive upstream recycling. The suggestion that extra-Rayleigh distillation seen in the TES δD observations in *Worden et al.* [2007] and *Brown et al.* [2008] is the result of upstream moisture recycling is supported by the GCM experiments.
5. The cold-season temperature effect is the superposition of Rayleigh distillation where it snows, and phase-dependent PCE where precipitation falls as a mix of rain and snow, most notably over Europe.

The experiments conducted in this analysis illustrate a potential approach for future interpretation studies of vapor isotope measurements. Satellite profile retrievals in the troposphere would be especially useful, as these measurements are considered an exciting new means through which to understand moist processes in the atmosphere [*Sherwood et al.*, 2010], and early studies using these data with box and trajectory models have shown

great promise. There remains much investigation to be done along these lines with isotopically-equipped GCMs. Indeed, this study was comprised of a single, global-scale GCM experiment, describing the effects of PCE from the tropics to the poles. It would be interesting in the future to conduct more detailed mechanistic studies for specific regions, partitioning, for example, the effects of condensate re-evaporation from equilibration at low latitudes, as distinguished by *Risi et al.* [2008], or the effects of equilibrium and kinetic deposition to ice in cold regions. It would also be useful to conduct such studies across additional isotopically-equipped GCMs, to determine the sensitivity to particular cloud physics parameterizations.

Chapter 6
Conclusions

6.1 Summary of results

This dissertation was motivated by an interest in developing a better understanding of two types of controls on the isotopic composition of water in the atmosphere: the large-scale atmospheric circulation in the extra-tropics, and, globally, the effects of post-condensation exchange (PCE). The NASA GISS ModelE isotopically-equipped GCM was used to examine these controls, using both diagnoses of control simulations and also by conducting experimental runs, the latter being methodologically distinct from most previous GCM analyses. Throughout the dissertation, a particular effort has gone into comparing the GCM to observations, resulting in what is, arguably, the most quantitative evaluation of an isotopically-equipped GCM conducted to-date.

In Chapter 3, different controls on precipitation $\delta^{18}O$ over Europe were compared between GNIP observations and the GCM. Europe has the world's most dense network of long-term precipitation $\delta^{18}O$ data, providing the best possible opportunity for validation of controls identified in the GCM. In both observations and the GCM, the local temperature effect was identified, and extended outside of Europe. This temperature control, in turn, was related to a NAO-like dipole, but with centres of action different than in the standard NAO definitions. An examination of mid-tropospheric circulation controls showed that European $\delta^{18}O$ in fact reflects hemisphere-wide teleconnections associated with the NAM. Seasonal differences were found in the strength of all controls on $\delta^{18}O$, with the annual controls being the combination of strong winter and weak summer controls. The weaker temperature effect in summer is well known and has been universally attributed to the effects of continental moisture recycling, but the results of this study show that an additional factor is the reduced variability in summer-time atmospheric circulation. The strong agreement between observed and modeled circulation controls on precipitation $\delta^{18}O$ over Europe should give confidence in using the GCM to identify such controls in other, less data-rich regions at mid-latitudes.

In Chapter 4, atmospheric circulation controls over precipitation $\delta^{18}O$ in the SW Yukon were examined with the GCM. The results showed that, particularly during the cool season, elevated $\delta^{18}O$ is associated with a deeper AL and stronger southerly moisture flow, while lower $\delta^{18}O$ is associated with the opposite meteorological conditions. These results suggest that the large mid-19th century shift towards lower $\delta^{18}O$ values seen in paleoclimate records from the region was associated with a shift towards a weaker AL. While in disagreement with a previous interpretation of this shift, it is consistent with records of glacial advance and tree-ring growth during the same period, and observational studies of AL controls on temperature and precipitation in the region.

In Chapter 5, a modeling experiment was conducted to determine the effects of PCE on the isotopic composition of water in the atmosphere. PCE was found to universally deplete vapor in heavy isotopes, but had differential effects on precipitation. At low latitudes, local PCE with fresh vapor at the surface enriches precipitation, particularly when rainfall is light. When rainfall is heavy, PCE tends to deplete vapor and precipitation in heavy isotopes via atmospheric moisture recycling, strongly supporting recent interpretations of vapor isotope measurements from satellites. In the extratropics, local PCE-related enrichment can be offset by upstream PCE-related depletion of the vapor reservoir in heavy isotopes, and result in a net isotopic depletion. The transition from net enrichment to net depletion is controlled by the transition from rain to snow-dominated precipitation. In most regions, the temperature effect was unaffected by the absence of PCE. But, somewhat surprisingly, in regions with a strong seasonal mix of rain and snow such as Europe, the temperature effect appears to be controlled by phase-dependent PCE, rather than Rayleigh distillation, and ultimately, to the influence of temperature on the phase of precipitation. The absence of a temperature effect over Europe without PCE suggests a different underlying mechanism than was described in Chapter 3. There, the temperature effect was attributed to variability in moisture transport and circulation, via an underlying Rayleigh depletion. The results of Chapter 5 indicate that this is not the case. An alternative mechanism is that more southerly transport is associated with a greater proportion of rain-dominated precipitation, which is enriched

isotopically by PCE. This finding is a significant departure from the numerous Rayleigh-based interpretations of the temperature effect over Europe.

A common theme emerging across the three chapters is the importance of seasonality in the strength of controls on precipitation $\delta^{18}O$. In both Europe and the SW Yukon, circulation controls are much stronger during winter than summer. This simply corresponds to the seasonal strength of features such as the Aleutian and Icelandic Lows, but is a mechanism needing more attention in interpreting paleo-isotopic archives. Seasonality is considered in interpreting the different deposition mechanisms for particular archives, for example, summer tree-growth in interpreting cellulose $\delta^{18}O$, but is not as well appreciated in the context of atmospheric circulation. Seasonality was also important in modeling the temperature effect in Chapter 5. All previous global GCM analyses of the temperature effect have focused on annual means or on anomalies for all months of the year. The results of Chapter 5, irrespective of the importance of PCE, showed that the modeled temperature effect is largely a winter time phenomenon.

The results of Chapters 3 and 5 contribute to validation of isotopically-equipped GCMs against observations. The comparison of circulation controls on $\delta^{18}O$ for GCM and observations over Europe was the first such analysis for mid-latitudes, following the extensive low-latitude comparisons of *Vuille and Werner* [2005] and *Vuille et al.* [2005]. The strong agreement over Europe should increase confidence in using the GCM to identify circulation controls on precipitation isotopes for other, less-data rich regions in the mid-latitudes such as the SW Yukon. In Chapter 5, the quantitative comparison against GNIP data provides an error constraint on the GCM's ability to simulate precipitation $\delta^{18}O$. While many other GCMs have qualitatively compared mean seasonal precipitation $\delta^{18}O$ between GCMs and observations, this study was the first to quantify that relationship in terms of spatial correlation, bias and RMSE, along with underlying contributions from PCE.

6.2 Suggestions for future work

This dissertation originated in trying to improve our understanding of the Mt. Logan $\delta^{18}O$ record, and a main finding of the GCM analysis was the importance of seasonality in the

existence of strong circulation controls on precipitation $\delta^{18}O$ in the SW Yukon. Consequently, efforts are currently underway to retrieve a seasonally-decomposed $\delta^{18}O$ for the PR Col (G. Holdsworth, pers. comm.), to identify such controls in the actual ice core record. New ice cores are also being extracted for Mt. Bona-Churchill and Mt. Denali in Alaska, and from Mt. Waddington in southwestern British Columbia. This will form an arc of high-accumulation ice cores with which pre-instrumental climate variability in the north Pacific can be better understood. For such analyses, the importance of seasonal separation of the ice core record should be emphasized. The availability of these new cores should also motivate further modeling studies. Chief among these should be simulations with the high-resolution regional climate model of *Sturm et al.* [2005], particularly for the sake of better-capturing the region's complex topography, and tagged moisture source experiments that have only recently become available with the GISS ModelE.

The GCM analysis described in Chapter 4 was an analogue study, which assumed that present-day circulation controls were applicable in interpreting pre-instrumental shifts in the ice core record. Alternatively, it would be informative to conduct time-slice equilibrium simulations using the fully coupled, isotopically-equipped GISS ModelE-R atmosphere-ocean model [*Schmidt et al.*, 2007]. *LeGrande and Schmidt* [2009] recently conducted 1000-year time-slice runs through the Holocene with ModelE-R, forced by changing orbital parameters, greenhouse gas concentrations and ice sheet extent, successfully capturing, for example, observed isotopic changes in calcite from Asian speleothems. This approach has the key advantage of not relying upon empirical transfer functions between isotopes and temperature, instead modeling the proxy composition directly, and then attributing observed changes using diagnosis with the internally-consistent model-generated climate. During the early Holocene, *LeGrande and Schmidt* [2009] attributed lower precipitation $\delta^{18}O$ in the Asian interior to intensified land moisture export from the tropics, and not changes in local precipitation, for example. The anticipated availability of a broad ice core $\delta^{18}O$ network ringing the north Pacific would be an ideal region for which to conduct a similar analysis, to better understand low-frequency shifts such as that observed at Mt. Logan in the mid 19th century, should they appear consistently across the ice core network.

In addition to ice core interpretation, the analysis of European precipitation $\delta^{18}O$ in Chapter 3 demonstrated the potential for mid-latitude, paleo-isotopic reconstructions of atmospheric circulation from non-ice core sources such as tree-rings. This approach to tree-ring $\delta^{18}O$ interpretation is not well-established, however, despite its potential utility as a high-resolution proxy with extensive spatial availability [*McCarroll and Loader*, 2004]. With continually improving sampling techniques [*Robertson et al.*, 2008], understanding of the physiological controls on cellulose $\delta^{18}O$ [*Roden et al.*, 2000], and improving data archives [*Csank*, 2009], there will be tremendous potential for isotopic reconstructions of large-scale climate patterns. *Treydte et al.* [2007] have developed a multi-species tree-ring $\delta^{18}O$ record for Europe, spanning sites from Morocco to northern Sweden. Preliminary analysis shows that the first principal component from the record has a surface circulation expression remarkably similar to the observed and modeled precipitation $\delta^{18}O$ and SLP correlation patterns in Figure 3-9 (K. Treydte, pers. comm.).

In Chapter 5, selected comparisons were made between the modeled vapor isotopes and TES measurements from previous studies. It was shown with GCM experiments that, as had been previously suggested, the extra-Rayleigh depletion associated with intensive convection could be explained by PCE. This analysis hinted at the potential for vapor isotope measurements to be used in further constraining moist processes in the atmosphere, such as rainfall evaporation. Rainfall evaporation has long been recognized as an important mechanism of moisture and energy transfer in the atmosphere [*Bony and Emanuel*, 2005; *Pauluis*], and parameterizations of rainfall evaporation have been incorporated into most GCMs [*Gaffen et al.*, 1997; *Risi et al.*, 2008]. Actual rainfall evaporation strength remains poorly constrained, however, and the Madden Julian Oscillation (MJO) variation and Inter-Tropical Convergence Zone (ITCZ) in particular are sensitive to this uncertainty [*Bacmeister et al.*, 2006; *Maloney*, 2009]. That the strength of rainfall evaporation is poorly known is in part because modeled rainfall evaporation can be compared only indirectly against measurements of humidity and precipitation.

Because the isotopic composition of atmospheric moisture in part reflects the strength of rainfall evaporation, it acts as an intermediate parameter against which to compare model

predictions. Until recently, there have been too few measurements of vapor isotope data to conduct a systematic comparison between model parameterizations of rainfall evaporation and isotopic observation, but this has changed with the availability of vapor δD retrievals in the lower troposphere from TES, the Scanning Imaging Absorption Spectrometer for Atmospheric Chartography (SCIAMACHY) instrument on board the European Space Agency's Envisat satellite [*Frankenberg et al.*, 2009] and anticipated retrievals from the Japan Aerospace Exploration Agency's Greenhouse gases Observing SATellite (GOSAT) (J. Worden, pers. comm.).

It would be interesting in the future to extend the offline PCE experiments of Chapter 5 to the on-line prognostic moisture, and include comparison against the satellite vapor isotope data. This would follow previous rainfall evaporation experiments with GCMs [*Bacmeister et al.*, 2006; *Maloney*, 2009], but which lacked isotopic quantities. In addition to changes in the precipitation rates and humidity fields examined in those studies, modeled δD fields under the different experiments would be compared against satellite δD measurements, to identify the rainfall evaporation strength most consistent with observations. In combination with the passive tracer experiments of the type conducted in Chapter 5, we can in principle determine, for example, the degree to which rainfall evaporation strength influences the MJO and ITCZ in terms of both the immediate microphysical processes, and secondary changes to dynamics. This should contribute to improved parameterizations of condensate evaporation in GCMs and more reliable prediction of changing atmospheric moisture under future forcings and feedbacks.

References

Aggarwal, P. K., K. Froehlich, R. Gonfiantini, and J. R. Gat (2005), Isotope Hydrology: A Historical Perspective from the IAEA, in *Isotopes in the Water Cycle: Past, Present and Future of a Developing Science*, edited by P. K. Aggarwal, et al., pp. 3-8, Springer, Dordrecht, Netherlands.

Aldaz, L., and S. Deutsch (1967), On a Relationship Between Air Temperature and Oxygen Isotope Ratio of Snow and Firn in South Pole Region, *Earth and Planetary Science Letters*, *3*(3), 267-274.

Alley, R. B., and K. M. Cuffey (2001), Oxygen- and hydrogen-isotopic ratios of water in precipitation: Beyond paleothermometry, *Stable Isotope Geochemistry*, *43*, 527-553.

Anderson, L., M. B. Abbott, B. P. Finney, and S. J. Burns (2005), Regional Atmospheric Circulation Change in the North Pacific During the Holocene Inferred From Lacustrine Carbonate Oxygen Isotopes, Yukon Territory, Canada, *Quaternary Research*, *64*(1), 21-35.

Araguas-Araguas, L., K. Froehlich, and K. Rozanski (1998), Stable Isotope Composition of Precipitation Over Southeast Asia, *Journal of Geophysical Research-Atmospheres*, *103*(D22), 28721-28742.

Araguas-Araguas, L., K. Froehlich, and K. Rozanski (2000), Deuterium and Oxygen-18 Isotope Composition of Precipitation and Atmospheric Moisture, *Hydrological Processes*, *14*(8), 1341-1355.

Bacmeister, J. T., M. J. Suarez, and F. R. Robertson (2006), Rain reevaporation, boundary layer-convection interactions, and Pacific rainfall patterns in an AGCM, *Journal of the Atmospheric Sciences*, *63*(12), 3383-3403.

Baldini, L. M., F. McDermott, A. M. Foley, and J. U. L. Baldini (2008), Spatial variability in the European winter precipitation delta O-18-NAO relationship: Implications for reconstructing NAO-mode climate variability in the Holocene, *Geophysical Research Letters*, *35*(4), L04709, doi:10.1029/2007gl032027.

Baldwin, M. P., and T. J. Dunkerton (1999), Propagation of the Arctic Oscillation from the stratosphere to the troposphere, *Journal of Geophysical Research-Atmospheres*, *104*(D24), 30937-30946.

Barlow, L. K., J. W. C. White, R. G. Barry, J. C. Rogers, and P. M. Grootes (1993), The North-Atlantic Oscillation Signature in Deuterium and Deuterium Excess Signals in the Greenland Ice-Sheet Project-2 Ice Core, 1840-1970, *Geophysical Research Letters*, *20*(24), 2901-2904.

Barnston, A. G., and R. E. Livezey (1987), Classification, Seasonality and Persistence of Low-Frequency Atmospheric Circulation Patterns, *Monthly Weather Review*, *115*(6), 1083-1126.

Beer, R., T. A. Glavich, and D. M. Rider (2001), Tropospheric emission spectrometer for the Earth Observing System's Aura Satellite, *Applied Optics*, *40*(15), 2356-2367.

Birks, S. J., and T. W. D. Edwards (2009), Atmospheric circulation controls on precipitation isotope-climate relations in western Canada, *Tellus Series B-Chemical and Physical Meteorology*, *61*(3), 566-576, doi:10.1111/j.1600-0889.2009.00423.x.

Blunier, T., and E. J. Brook (2001), Timing of Millennial-Scale Climate Change in Antarctica and Greenland During the Last Glacial Period, *Science*, *291*(5501), 109-112.

Bograd, S., F. Schwing, R. Mendelssohn, and P. Green-Jessen (2002), On the changing seasonality over the North Pacific, *Geophysical Research Letters*, *29*(9), Artn 1333 doi: 10.1029/2001gl013790.

Bony, S., and K. A. Emanuel (2005), On the role of moist processes in tropical intraseasonal variability: Cloud-radiation and moisture-convection feedbacks, *Journal of the Atmospheric Sciences*, *62*(8), 2770-2789.

Brown, D., J. Worden, and D. Noone (2008), Comparison of atmospheric hydrology over convective continental regions using water vapor isotope measurements from space, *Journal of Geophysical Research-Atmospheres*, *113*(D15), D15124,doi :10.1029/2007jd009676.

Brown, J., I. Simmonds, and D. Noone (2006), Modeling delta O-18 in tropical precipitation and the surface ocean for present-day climate, *Journal of Geophysical Research-Atmospheres*, *111*(D5), Artn D05105, Doi 10.1029/2004jd005611.

Brutsaert, W. (1975), Theory for Local Evaporation (or Heat-Transfer) from Rough and Smooth Surfaces at Ground Level, *Water Resources Research*, *11*(4), 543-550.

Calkin, P. E., G. C. Wiles, and D. J. Barclay (2001), Holocene coastal glaciation of Alaska, *Quaternary Science Reviews*, *20*(1-3), 449-461.

Celle-Jeanton, H., R. Gonfiantini, Y. Travi, and B. Sol (2004), Oxygen-18 Variations of Rainwater During Precipitation: Application of the Rayleigh Model to Selected Rainfalls in Southern France, *Journal of Hydrology*, *289*(1-4), 165-177.

Charles, C. D., D. Rind, J. Jouzel, R. D. Koster, and R. G. Fairbanks (1994), Glacial-Interglacial Changes in Moisture Sources for Greenland - Influences on the Ice Core Record of Climate, *Science*, *263*(5146), 508-511.

Ciais, P., and J. Jouzel (1994), Deuterium and Oxygen-18 in Precipitation - Isotopic Model, Including Mixed Cloud Processes, *Journal of Geophysical Research-Atmospheres*, *99*(D8), 16793-16803.

Clark, I., and P. Fritz (1997), *Environmental Isotopes in Hydrogeology*, 311 pp., Lewis Publishers, New York.

Cole, J. E., D. Rind, R. S. Webb, J. Jouzel, and R. Healy (1999), Climatic Controls on Interannual Variability of Precipitation Delta O-18: Simulated Influence of Temperature, Precipitation Amount, and Vapor Source Region, *Journal of Geophysical Research-Atmospheres*, *104*(D12), 14223-14235.

Cook, E. R., R. D. D'Arrigo, and M. E. Mann (2002), A well-verified, multiproxy reconstruction of the winter North Atlantic Oscillation index since AD 1400, *Journal of Climate*, *15*(13), 1754-1764.

Craig, H. (1961), Isotopic Variations in Meteoric Waters, *Science*, *133*(346), 1702-1703.

Craig, H., and L. I. Gordon (1965), Deuterium and oxygen 18 variations in the ocean and marine atmosphere, in *Stable Isotopes in Oceanographic Studies and Paleotemperatures*, edited by E. Tongiorgi, pp. 9-130, Consiglio Nazionale Delle Ricerche Laboratorio Di Geologia Nucleare - PISA, Spoleto.

Csank, A. Z. (2009), An International Tree-Ring Isotope Data Bank-a Proposed Repository for Tree-Ring Isotopic Data, *Tree-Ring Research*, *65*(2), 163-164.

D'Arrigo, R., R. Wilson, C. Deser, G. Wiles, E. Cook, R. Villalba, A. Tudhope, J. Cole, and B. Linsley (2005), Tropical-North Pacific Climate Linkages Over the Past Four Centuries, *Journal of Climate*, *18*(24), 5253-5265.

Dai, A. (2001), Global precipitation and thunderstorm frequencies. Part I: Seasonal and interannual variations, *Journal of Climate*, *14*(6), 1092-1111.

Danis, P. A., V. Masson-Delmotte, M. Stievenard, M. T. Guillemim, V. Daux, P. Naveau, and U. von Grafenstein (2006), Reconstruction of past precipitation beta O-18 using tree-ring cellulose delta O-18 and delta C-13: A calibration study near Lac d'Annecy, France, *Earth and Planetary Science Letters*, *243*(3-4), 439-448, 10.1016/j.epsl.2006.01.023.

Dansgaard, W. (1954), The O-18-Abundance in Fresh Water, *Geochimica Et Cosmochimica Acta*, *6*(5-6), 241-260.

Dansgaard, W. (1964), Stable Isotopes in Precipitation, *Tellus*, *16*(4), 436-468.

Dansgaard, W., S. J. Johnsen, J. Moller, and C. C. Langway (1969), One Thousand Centuries of Climatic Record from Camp Century on Greenland Ice Sheet, *Science*, *166*(3903), 377-381.

Del Genio, A. D., and M. S. Yao (1993), Efficient cumulus parameterization for long-term climate studies: The GISS scheme, in *The Representation of Cumulus Convection in Numerical Models*, edited, pp. 181-184, American Meteorological Society.

Del Genio, A. D., M. S. Yao, W. Kovari, and K. K. W. Lo (1996), A Prognostic Cloud Water Parameterization for Global Climate Models, *Journal of Climate*, *9*(2), 270-304.

Del Genio, A. D., W. Kovari, M. S. Yao, and J. Jonas (2005), Cumulus Microphysics and Climate Sensitivity, *Journal of Climate*, *18*(13), 2376-2387.

DeNiro, M. J., and S. Epstein (1979), Relationship between the Oxygen Isotope Ratios of Terrestrial Plant Cellulose, Carbon-Dioxide, and Water, *Science*, *204*(4388), 51-53.

Dessler, A. E., and K. Minschwaner (2007), An analysis of the regulation of tropical tropospheric water vapor, *Journal of Geophysical Research-Atmospheres*, *112*(D10), Artn D10120, Doi 10.1029/2006jd007683.

Dirmeyer, P. A., and K. L. Brubaker (2007), Characterization of the global hydrologic cycle from a back-trajectory analysis of atmospheric water vapor, *Journal of Hydrometeorology*, *8*(1), 20-37, doi:10.1175/Jhm557.1.

Edwards, M. E., C. J. Mock, B. P. Finney, V. A. Barber, and P. J. Bartlein (2001), Potential Analogues for Paleoclimatic Variations in Eastern Interior Alaska During the Past 14,000 Yr: Atmospheric-Circulation Controls of Regional Temperature and Moisture Responses, *Quaternary Science Reviews*, *20*(1-3), 189-202.

Efron, B., and G. Gong (1983), A Leisurely Look at the Bootstrap, the Jackknife, and Cross-Validation, *American Statistician*, *37*(1), 36-48.

Ehhalt, D. H., and L. E. Heidt (1974), Vertical Profiles of Molecular H2 and CH4 in Stratosphere, *Aiaa Journal*, *12*(6), 822-825.

Ekaykin, A. A. (2003), Meteorological regime of central Antarctica and its role in the formation of isotope composition of snow thickness, 122pp pp, University Joseph Fourier, Grenoble, France.

EPICA (2006), One-to-One Coupling of Glacial Climate Variability in Greenland and Antarctica, *Nature*, *444*(7116), 195-198.

Epstein, S., and C. J. Yapp (1976), Climatic Implications of D-H Ratio of Hydrogen in C-H Groups in Tree Cellulose, *Earth and Planetary Science Letters*, *30*(2), 252-261.

Etien, N., V. Daux, V. Masson-Delmotte, M. Stievenard, V. Bernard, S. Durost, M. T. Guillemin, O. Mestre, and M. Pierre (2008), A bi-proxy reconstruction of Fontainebleau (France) growing season temperature from AD 1596 to 2000, *Climate of the Past*, *4*(2), 91-106.

Fairchild, I. J., C. L. Smith, A. Baker, L. Fuller, C. Spotl, D. Mattey, F. McDermott, and Eimp (2006), Modification and preservation of environmental signals in speleothems, *Earth-Science Reviews*, *75*(1-4), 105-153, doi:10.1016/j.earscirev.2005.08.003.

Faure, G., and T. M. Mensing (Eds.) (2005), *Isotopes: Principles and Applications*, 3rd ed., 897 pp., John Wiley and Sons, Hoboken, NJ.

Feng, X. H., A. M. Faiia, and E. S. Posmentier (2009), Seasonality of isotopes in precipitation: A global perspective, *Journal of Geophysical Research-Atmospheres*, *114*, D08116, doi:10.1029/2008jd011279.

Field, R. D. (2010), Observed and modeled controls on precipitation δ18O over Europe: from local temperature to the Northern Annular Mode, *Journal of Geophysical Research-Atmospheres*, *115*(D12101), doi:10.1029/2009JD013370.

Field, R. D., G. W. K. Moore, G. Holdsworth, and G. A. Schmidt (2010), A GCM-based analysis of circulation controls on delta O-18 in the southwest Yukon, Canada: Implications for climate reconstructions in the region, *Geophysical Research Letters*, *37*, Artn L05706, doi 10.1029/2009gl041408.

Field, R. D., D. B. A. Jones, and D. P. Brown (in press), The effects of post-condensation exchange on the isotopic composition of water in the atmosphere, *Journal of Geophysical Research-Atmospheres*.

Fisher, D. A., C. Wake, K. Kreutz, K. Yalcin, E. Steig, P. Mayewski, L. Anderson, J. Zheng, S. Rupper, C. Zdanowicz, M. Demuth, M. Waszkiewicz, D. Dahl-Jensen, K. Goto-Azuma, J. B. Bourgeois, R. M. Koerner, J. Sekerka, E. Osterberg, M. P. Abbott, B. P. Finney, and S. J. Burns (2004), Stable isotope records from Mount Logan, Eclipse ice cores and nearby Jellybean Lake. Water cycle of the North Pacific over 2000 years and over five vertical kilometres: sudden shifts and tropical connections, *Geographie physique et Quaternaire*, *58*(2-3), 337-352.

Frankenberg, C., K. Yoshimura, T. Warneke, I. Aben, A. Butz, N. Deutscher, D. Griffith, F. Hase, J. Notholt, M. Schneider, H. Schrijver, and T. Rockmann (2009), Dynamic Processes Governing Lower-Tropospheric HDO/H2O Ratios as Observed from Space and Ground, *Science*, *325*(5946), 1374-1377, DOI 10.1126/science.1173791.

Fricke, H. C., and J. R. O'Neil (1999), The Correlation Between O-18/O-16 Ratios of Meteoric Water and Surface Temperature: Its Use in Investigating Terrestrial Climate Change Over Geologic Time, *Earth and Planetary Science Letters*, *170*(3), 181-196.

Friedman, I. (1953), Deuterium Content of Natural Waters and Other Substances, *Geochimica Et Cosmochimica Acta*, *4*(1-2), 89-103.

Friedman, I., L. Machta, and R. Soller (1962), Water-Vapor Exchange between a Water Droplet and Its Environment, *Journal of Geophysical Research*, *67*(7), 2761-2766.

Friedman, I., J. M. Harris, G. I. Smith, and C. A. Johnson (2002), Stable isotope composition of waters in the Great Basin, United States - 1. Air-mass trajectories, *Journal of Geophysical Research-Atmospheres*, *107*(D19), 4400, doi: 10.1029/2001jd000565.

Gaffen, D. J., R. D. Rosen, D. A. Salstein, and J. S. Boyle (1997), Evaluation of tropospheric water vapor simulations from the atmospheric model intercomparison project, *Journal of Climate*, *10*(7), 1648-1661.

Galewsky, J., M. Strong, and Z. D. Sharp (2007), Measurements of water vapor D/H ratios from Mauna Kea, Hawaii, and implications for subtropical humidity dynamics, *Geophysical Research Letters*, *34*(22), L22808,:10.1029/2007gl031330.

Gat, J. R., and E. Matsui (1991), Atmospheric Water-Balance in the Amazon Basin - an Isotopic Evapotranspiration Model, *Journal of Geophysical Research-Atmospheres*, *96*(D7), 13179-13188.

Gat, J. R. (1996), Oxygen and Hydrogen Isotopes in the Hydrologic Cycle, *Annual Review of Earth and Planetary Sciences*, *24*, 225-262.

Gat, J. R. (2000), Atmospheric Water Balance - the Isotopic Perspective, *Hydrological Processes*, *14*(8), 1357-1369.

Gedzelman, S., J. Lawrence, J. Gamache, M. Black, E. Hindman, R. Black, J. Dunion, H. Willoughby, and X. P. Zhang (2003), Probing Hurricanes With Stable Isotopes of Rain and Water Vapor, *Monthly Weather Review*, *131*(6), 1112-1127.

Gedzelman, S. D., and R. Arnold (1994), Modeling the Isotopic Composition of Precipitation, *Journal of Geophysical Research-Atmospheres*, *99*(D5), 10455-10471.

Gonfiantini, R., M. A. Roche, J. C. Olivry, J. C. Fontes, and G. M. Zuppi (2001), The Altitude Effect on the Isotopic Composition of Tropical Rains, *Chemical Geology*, *181*(1-4), 147-167.

Gray, J., and P. Thompson (1976), Climatic Information from 18o/16o Ratios of Cellulose in Tree Rings, *Nature*, *262*(5568), 481-482.

Hansen, J., G. Russell, D. Rind, P. Stone, A. Lacis, S. Lebedeff, R. Ruedy, and L. Travis (1983), Efficient 3-Dimensional Global-Models for Climate Studies - Model-I and Model-Ii, *Monthly Weather Review*, *111*(4), 609-662.

Hastings, M. G., E. J. Steig, and D. M. Sigman (2004), Seasonal variations in N and O isotopes of nitrate in snow at Summit, Greenland: Implications for the study of nitrate in snow and ice cores, *Journal of Geophysical Research-Atmospheres*, *109*(D20), Artn D20306, Doi 10.1029/2004jd004991.

Helsen, M. M., R. S. W. Van De Wal, M. R. Van Den Broeke, E. R. T. Kerstel, V. Masson-Delmotte, H. A. J. Meijer, C. H. Reijmer, and M. P. Scheele (2004), Modelling the Isotopic Composition of Snow Using Backward Trajectories: a Particular Precipitation Event in Dronning Maud Land, Antarctica, *Annals of Glaciology*, *39*, 293-299.

Helsen, M. M., R. S. W. Van De Wal, and M. R. Van Den Broeke (2007), The Isotopic Composition of Present-Day Antarctic Snow in a Lagrangian Atmospheric Simulation, *Journal of Climate*, *20*(4), 739-756.

Hendy, C. H., and A. T. Wilson (1968), Palaeoclimatic Data from Speleothems, *Nature*, *219*(5149), 48-51.

Herbin, H., D. Hurtmans, C. Clerbaux, L. Clarisse, and P. F. Coheur (2009), (H2O)-O-16 and HDO measurements with IASI/MetOp, *Atmospheric Chemistry and Physics*, *9*(24), 9433-9447.

Hoffmann, G., and M. Heimann (1997), Water Isotope Modeling in the Asian Monsoon Region, *Quaternary International*, *37*, 115-128.

Hoffmann, G., M. Werner, and M. Heimann (1998), Water Isotope Module of the ECHAM Atmospheric General Circulation Model: a Study on Timescales From Days to Several Years, *Journal of Geophysical Research-Atmospheres*, *103*(D14), 16871-16896.

Hoffmann, G., J. Jouzel, and V. Masson (2000), Stable Water Isotopes in Atmospheric General Circulation Models, *Hydrological Processes*, *14*(8), 1385-1406.

Hoffmann, G., M. Cuntz, J. Jouzel, and M. Werner (2006), How much climatic information do water isotopes contain? A systematic comparison between the IAEA/GNIP isotope network and the ECHAM 4 atmospheric general circulation model, in *Isotopes in the Water Cycle - Past, Present and Future of a Developing Science*, edited by P. K. Aggarwal, et al., p. 381, Springer, Berlin.

Holdsworth, G., H. R. Krouse, and M. Nosal (1992), Ice core climate signals from Mount Logan, Yukon, A.D. 1700-1897, in *Climate since A.D. 1500*, edited by R. S. Bradley and P. D. Jones, pp. 483-504, Routledge, London.

Horita, J., K. Rozanski, and S. Cohen (2008), Isotope effects in the evaporation of water: a status report of the Craig-Gordon model, *Isotopes in Environmental and Health Studies*, *44*(1), 23-49, Doi 10.1080/10256010801887174.

Hurrell, J. W., Y. Kushnir, G. Ottersen, and M. Visbeck (2003), An overview of the North Atlantic Oscillation, in *The North Atlantic Oscillation: Climatic Signficance and Environmental Impact*, edited by J. W. Hurrell, et al., pp. 1-36, American Geophysical Union, Washington, D.C.

IAEA (2006), Statistical Treatment of Isotope Data in Precipitation, 8 pp.

Jacob, H., and C. Sonntag (1991), An 8-Year Record of the Seasonal-Variation of H-2 and O-18 in Atmospheric Water-Vapor and Precipitation at Heidelberg, Germany, *Tellus Series B-Chemical and Physical Meteorology*, *43*(3), 291-300.

Johnsen, S. J., H. B. Clausen, Dansgaar.W, and C. C. Langway (1972), Oxygen Isotope Profiles through Antarctic and Greenland Ice Sheets, *Nature*, *235*(5339), 429-434.

Johnson, K. R., and B. L. Ingram (2004), Spatial and Temporal Variability in the Stable Isotope Systematics of Modern Precipitation in China: Implications for Paleoclimate Reconstructions, *Earth and Planetary Science Letters*, *220*(3-4), 365-377.

Jones, P. D., T. Jonsson, and D. Wheeler (1997), Extension to the North Atlantic Oscillation using early instrumental pressure observations from Gibraltar and south-west Iceland, *International Journal of Climatology*, *17*(13), 1433-1450.

Jones, P. D., and M. E. Mann (2004), Climate Over Past Millennia, *Reviews of Geophysics*, *42*(2).

Jones, P. D., K. R. Briffa, T. J. Osborn, J. M. Lough, T. D. van Ommen, B. M. Vinther, J. Lutherbacher, E. R. Wahl, F. W. Zwiers, M. E. Mann, G. A. Schmidt, C. M. Ammann, B. M. Buckley, K. M. Cobb, J. Esper, H. Goosse, N. Graham, E. Jansen, T. Kiefer, C. Kull, M. Kuttel, E. Mosley-Thompson, J. T. Overpeck, N. Riedwyl, M. Schulz, A. W. Tudhope, R. Villalba, H. Wanner, E. Wolff, and E. Xoplaki (2009), High-resolution palaeoclimatology of the last millennium: a review of current status and future prospects, *Holocene*, *19*(1), 3-49, doi:10.1177/0959683608098952.

Joussaume, S., R. Sadourny, and J. Jouzel (1984), A General-Circulation Model of Water Isotope Cycles in the Atmosphere, *Nature*, *311*(5981), 24-29.

Joussaume, S., and J. Jouzel (1993), Paleoclimatic Tracers - an Investigation Using an Atmospheric General-Circulation Model Under Ice-Age Conditions .2. Water Isotopes, *Journal of Geophysical Research-Atmospheres*, *98*(D2), 2807-2830.

Jouzel, J., and L. Merlivat (1984), Deuterium and O-18 in Precipitation - Modeling of the Isotopic Effects During Snow Formation, *Journal of Geophysical Research-Atmospheres*, *89*(ND7), 1749-1757.

Jouzel, J., G. L. Russell, R. J. Suozzo, R. D. Koster, J. W. C. White, and W. S. Broecker (1987), Simulations of the HDO and H2 O-18 Atmospheric Cycles Using the NASA GISS General-Circulation Model - the Seasonal Cycle for Present-Day Conditions, *Journal of Geophysical Research-Atmospheres*, *92*(D12), 14739-14760.

Jouzel, J., R. D. Koster, R. J. Suozzo, and G. L. Russell (1994), Stable Water Isotope Behavior During the Last Glacial Maximum - a General-Circulation Model Analysis, *Journal of Geophysical Research-Atmospheres*, *99*(D12), 25791-25801.

Jouzel, J., R. B. Alley, K. M. Cuffey, W. Dansgaard, P. Grootes, G. Hoffmann, S. J. Johnsen, R. D. Koster, D. Peel, C. A. Shuman, M. Stievenard, M. Stuiver, and J. White (1997), Validity of the Temperature Reconstruction From Water Isotopes in Ice Cores, *Journal of Geophysical Research-Oceans*, *102*(C12), 26471-26487.

Jouzel, J., V. Masson-Delmotte, O. Cattani, G. Dreyfus, S. Falourd, G. Hoffmann, B. Minster, J. Nouet, J. M. Barnola, J. Chappellaz, H. Fischer, J. C. Gallet, S. Johnsen, M. Leuenberger, L. Loulergue, D. Luethi, H. Oerter, F. Parrenin, G. Raisbeck, D. Raynaud, A. Schilt, J. Schwander, E. Selmo, R. Souchez, R. Spahni, B. Stauffer, J. P. Steffensen,

B. Stenni, T. F. Stocker, J. L. Tison, M. Werner, and E. W. Wolff (2007), Orbital and Millennial Antarctic Climate Variability Over the Past 800,000 Years, *Science*, *317*(5839), 793-796.

Kalnay, E., M. Kanamitsu, R. Kistler, W. Collins, D. Deaven, L. Gandin, M. Iredell, S. Saha, G. White, J. Woollen, Y. Zhu, M. Chelliah, W. Ebisuzaki, W. Higgins, J. Janowiak, K. C. Mo, C. Ropelewski, J. Wang, A. Leetmaa, R. Reynolds, R. Jenne, and D. Joseph (1996), The NCEP/NCAR 40-Year Reanalysis Project, *Bulletin of the American Meteorological Society*, *77*(3), 437-471.

Kavanaugh, J. L., and K. M. Cuffey (2003), Space and time variation of delta O-18 and delta D in Antarctic precipitation revisited, *Global Biogeochemical Cycles*, *17*(1), Artn 1017, Doi 10.1029/2002gb001910.

Kuang, Z. M., G. C. Toon, P. O. Wennberg, and Y. L. Yung (2003), Measured HDO/H2O ratios across the tropical tropopause, *Geophysical Research Letters*, *30*(7), 1372, doi: 10.1029/2003gl017023.

Kurita, N., N. Yoshida, G. Inoue, and E. A. Chayanova (2004), Modern isotope climatology of Russia: A first assessment, *Journal of Geophysical Research-Atmospheres*, *109*(D3), 15, D03102, doi:10.1029/2003jd003404.

Lachniet, M. S. (2009), Climatic and environmental controls on speleothem oxygen-isotope values, *Quaternary Science Reviews*, *28*(5-6), 412-432, doi:10.1016/j.quascirev.2008.10.021.

Lawrence, J. R., S. D. Gedzelman, D. Dexheimer, H. K. Cho, G. D. Carrie, R. Gasparini, C. R. Anderson, K. P. Bowman, and M. I. Biggerstaff (2004), Stable isotopic composition of water vapor in the tropics, *Journal of Geophysical Research-Atmospheres*, *109*(D6), Artn D06115, Doi 10.1029/2003jd004046.

Lee, J. E., I. Fung, D. J. DePaolo, and C. C. Henning (2007), Analysis of the global distribution of water isotopes using the NCAR atmospheric general circulation model, *Journal of Geophysical Research-Atmospheres*, *112*(D16), D16306, doi: 10.1029/2006jd007657.

Lee, J. E., R. Pierrehumbert, A. Swann, and B. R. Lintner (2009), Sensitivity of stable water isotopic values to convective parameterization schemes, *Geophysical Research Letters*, *36*, Artn L23801, doi 10.1029/2009gl040880.

LeGrande, A. N., and G. A. Schmidt (2009), Sources of Holocene variability of oxygen isotopes in paleoclimate archives, *Climate of the Past*, *5*(3), 441-455.

Leng, M. J., and J. D. Marshall (2004), Palaeoclimate interpretation of stable isotope data from lake sediment archives, *Quaternary Science Reviews*, *23*(7-8), 811-831, doi:10.1016/j.quascirev.2003.06.012.

Liu, J. J., D. B. A. Jones, J. R. Worden, D. Noone, M. Parrington, and J. Kar (2009), Analysis of the summertime buildup of tropospheric ozone abundances over the Middle East and North Africa as observed by the Tropospheric Emission Spectrometer instrument, *Journal of Geophysical Research-Atmospheres*, *114*, D05304, doi: 10.1029/2008jd010993.

Majoube, M. (1971a), Oxygen-18 and Deuterium Fractionation Between Water and Steam, *Journal De Chimie Physique Et De Physico-Chimie Biologique*, *68*(10), 1423-1436.

Majoube, M. (1971b), Fractionation in O-18 Between Ice and Water Vapor, *Journal De Chimie Physique Et De Physico-Chimie Biologique*, *68*(4), 625-636.

Maloney, E. D. (2009), The Moist Static Energy Budget of a Composite Tropical Intraseasonal Oscillation in a Climate Model, *Journal of Climate*, *22*(3), 711-729, doi: 10.1175/2008jcli2542.1.

Masson-Delmotte, V., S. Hou, A. Ekaykin, J. Jouzel, A. Aristarain, R. T. Bernardo, D. Bromwich, O. Cattani, M. Delmotte, S. Falourd, M. Frezzotti, H. Gallee, L. Genoni, E. Isaksson, A. Landais, M. M. Helsen, G. Hoffmann, J. Lopez, V. Morgan, H. Motoyama, D. Noone, H. Oerter, J. R. Petit, A. Royer, R. Uemura, G. A. Schmidt, E. Schlosser, J. C. Simoes, E. J. Steig, B. Stenni, M. Stievenard, M. R. van den Broeke, R. S. W. V. de Wal, W. J. V. de Berg, F. Vimeux, and J. W. C. White (2008), A review of Antarctic surface snow isotopic composition: Observations, atmospheric circulation, and isotopic modeling, *Journal of Climate*, *21*(13), 3359-3387, Doi 10.1175/2007jcli2139.1.

Mathieu, R., D. Pollard, J. E. Cole, J. W. C. White, R. S. Webb, and S. L. Thompson (2002), Simulation of stable water isotope variations by the GENESIS GCM for modern conditions, *Journal of Geophysical Research-Atmospheres*, *107*(D4), 18, 4037, doi:10.1029/2001jd900255.

Mattey, D., D. Lowry, J. Duffet, R. Fisher, E. Hodge, and S. Frisia (2008), A 53 year seasonally resolved oxygen and carbon isotope record from a modem Gibraltar speleothem: Reconstructed drip water and relationship to local precipitation, *Earth and Planetary Science Letters*, *269*(1-2), 80-95, 10.1016/j.epsl.2008.01.051.

McCarroll, D., and N. J. Loader (2004), Stable isotopes in tree rings, *Quaternary Science Reviews*, *23*(7-8), 771-801, doi 10.1016/j.quascirev.2003.06.017.

McDermott, F. (2004), Palaeo-climate reconstruction from stable isotope variations in speleothems: a review, *Quaternary Science Reviews*, *23*(7-8), 901-918, doi:10.1016/j.quascirev.2003.06.021.

Merlivat, L. (1978), Molecular Diffusivities of (H2O)-O-1 6 HD16O, and (H2O)-O-18 in Gases, *Journal of Chemical Physics*, *69*(6), 2864-2871.

Merlivat, L., and J. Jouzel (1979), Global Climatic Interpretation of the Deuterium-Oxygen-18 Relationship for Precipitation, *Journal of Geophysical Research-Oceans and Atmospheres*, *84*(NC8), 5029-5033.

Misra, V. (2009), Harvesting model uncertainty for the simulation of interannual variability, *Journal of Geophysical Research-Atmospheres*, *114*, D16113, doi: 10.1029/2008jd011686.

Mock, C. J., P. J. Bartlein, and P. M. Anderson (1998), Atmospheric circulation patterns and spatial climatic variations in Beringia, *International Journal of Climatology*, *18*(10), 1085-1104.

Mook, W. G. (Ed.) (2001), *Environmental Isotopes in the Hydrological Cycle: Principles and Applications*, 280 pp., UNESCO/IAEA, Groningen, Netherlands.

Moore, G. W. K., G. Holdsworth, and K. Alverson (2002), Climate Change in the North Pacific Region Over the Past Three Centuries, *Nature*, *420*(6914), 401-403.

Nassar, R., P. F. Bernath, C. D. Boone, A. Gettelman, S. D. McLeod, and C. P. Rinsland (2007), Variability in HDO/H2O abundance ratios in the tropical tropopause layer, *Journal of Geophysical Research-Atmospheres*, *112*(D21), D21305, doi:10.1029/2007jd008417.

Noone, D., and I. Simmonds (2002), Associations Between Delta O-18 of Water and Climate Parameters in a Simulation of Atmospheric Circulation for 1979-95, *Journal of Climate*, *15*(22), 3150-3169.

Noone, D., and C. Sturm (2010), Comprehensive Dynamical Models of Global and Regional Water Isotope Distributions, in *Isoscapes: Understanding Movement, Pattern and Process on Earth Through Isotope Mapping*, edited by J. B. West, et al., pp. 195-219, Springer, Dordrecht.

Numaguti, A. (1999), Origin and recycling processes of precipitating water over the Eurasian continent: Experiments using an atmospheric general circulation model, *Journal of Geophysical Research-Atmospheres*, *104*(D2), 1957-1972.

Paterson, W. S. B., R. M. Koerner, D. Fisher, S. J. Johnsen, H. B. Clausen, W. Dansgaard, P. Bucher, and H. Oeschger (1977), An Oxygen-Isotope Climatic Record from Devon Island Ice Cap, Arctic Canada, *Nature*, *266*(5602), 508-511.

Pauluis, O. (2007), Sources and sinks of available potential energy in a moist atmosphere, *Journal of the Atmospheric Sciences*, *64*(7), 2627-2641, Doi 10.1175/Jas3937.1.

Peixoto, J. P., and A. H. Oort (1992), *Physics of Climate*, 520 pp., AIP Press, New York, NY.

Peng, H. D., B. Mayer, S. Harris, and H. R. Krouse (2004), A 10-Yr Record of Stable Isotope Ratios of Hydrogen and Oxygen in Precipitation at Calgary, Alberta, Canada, *Tellus Series B-Chemical and Physical Meteorology*, *56*(2), 147-159.

Peng, T. R., C. H. Wang, C. C. Huang, L. Y. Fei, C. T. A. Chen, and J. L. Hwong (2010), Stable isotopic characteristic of Taiwan's precipitation: A case study of western Pacific monsoon region, *Earth and Planetary Science Letters*, *289*(3-4), 357-366, DOI 10.1016/j.epsl.2009.11.024.

Pierrehumbert, R. T. (1998), Lateral mixing as a source of subtropical water vapor, *Geophysical Research Letters*, *25*(2), 151-154.

Pierrehumbert, R. T. (1999), Huascaran Delta O-18 as an Indicator of Tropical Climate During the Last Glacial Maximum, *Geophysical Research Letters*, *26*(9), 1345-1348.

Prather, M. J. (1986), Numerical Advection by Conservation of 2nd-Order Moments, *Journal of Geophysical Research-Atmospheres*, *91*(D6), 6671-6681.

Proctor, C. J., A. Baker, W. L. Barnes, and R. A. Gilmour (2000), A thousand year speleothem proxy record of North Atlantic climate from Scotland, *Climate Dynamics*, *16*(10-11), 815-820.

Rayner, N. A., D. E. Parker, E. B. Horton, C. K. Folland, L. V. Alexander, D. P. Rowell, E. C. Kent, and A. Kaplan (2003), Global analyses of sea surface temperature, sea ice, and night marine air temperature since the late nineteenth century, *Journal of Geophysical Research-Atmospheres*, *108*(D14), 4407, doi:10.1029/2002jd002670.

Risi, C., S. Bony, and F. Vimeux (2008), Influence of convective processes on the isotopic composition (delta O-18 and delta D) of precipitation and water vapor in the tropics: 2. Physical interpretation of the amount effect, *Journal of Geophysical Research-Atmospheres*, *113*(D19), D19306, doi: 10.1029/2008jd009943.

Risi, C., S. Bony, F. Vimeux, and J. Jouzel (2010), Water stable isotopes in the LMDZ4 General Circulation Model: model evaluation for present day and past climates and applications to climatic interpretations of tropical isotopic records, *J. Geophys. Res.*, doi:10.1029/2009JD013255.

Robertson, I., S. W. Leavitt, N. J. Loader, and W. Buhay (2008), Progress in isotope dendroclimatology, *Chemical Geology*, *252*(1-2), Ex1-Ex4, Doi 10.1016/S0009-2541(08)00177-0.

Roden, J. S., G. G. Lin, and J. R. Ehleringer (2000), A mechanistic model for interpretation of hydrogen and oxygen isotope ratios in tree-ring cellulose, *Geochimica Et Cosmochimica Acta*, *64*(1), 21-35.

Rodgers, C. D. (2000), *Inverse Methods for Atmospheric Sounding: Theory and Practice*, World Scientific, River Edge, NJ.

Rogers, J. C., J. F. Bolzan, and V. A. Pohjola (1998), Atmospheric Circulation Variability Associated With Shallow-Core Seasonal Isotopic Extremes Near Summit, Greenland, *Journal of Geophysical Research-Atmospheres*, *103*(D10), 11205-11219.

Rozanski, K., and C. Sonntag (1982), Vertical-Distribution of Deuterium in Atmospheric Water-Vapor, *Tellus*, *34*(2), 135-141.

Rozanski, K., C. Sonntag, and K. O. Munnich (1982), Factors Controlling Stable Isotope Composition of European Precipitation, *Tellus*, *34*(2), 142-150.

Rozanski, K., L. Araguas-Araguas, and R. Gonfiantini (1992), Relation Between Long-Term Trends of O-18 Isotope Composition of Precipitation and Climate, *Science*, *258*(5084), 981-985.

Rozanski, K., L. Araguas-Araguas, and R. Gonfiantini (1993), Isotopic Patterns in Modern Global Precipitation, in *Climate Change in Continental Isotopic Records*, edited by P. K. Swart, et al., pp. 1-36, American Geophysical Union, Washington, DC.

Rupper, S., E. J. Steig, and G. Roe (2004), The Relationship Between Snow Accumulation at Mt. Logan, Yukon, Canada, and Climate Variability in the North Pacific, *Journal of Climate*, *17*(24), 4724-4739.

Russell, G. L., and J. A. Lerner (1981), A New Finite-Differencing Scheme for the Tracer Transport-Equation, *Journal of Applied Meteorology*, *20*(12), 1483-1498.

Salati, E., A. Dallolio, E. Matsui, and J. R. Gat (1979), Recycling of Water in the Amazon Basin - Isotopic Study, *Water Resources Research*, *15*(5), 1250-1258.

Sato, T., M. Tsujimura, T. Yamanaka, H. Iwasaki, A. Sugimoto, M. Sugita, F. Kimura, G. Davaa, and D. Oyunbaatar (2007), Water sources in semiarid northeast Asia as revealed by field observations and isotope transport model, *Journal of Geophysical Research-Atmospheres*, *112*(D17), D17112,:10.1029/2006jd008321.

Saurer, M., P. Cherubini, C. E. Reynolds-Henne, K. S. Treydte, W. T. Anderson, and R. T. W. Siegwolf (2008), An investigation of the common signal in tree ring stable isotope chronologies at temperate sites, *Journal of Geophysical Research-Biogeosciences*, *113*(G4), 11, G04035, doi: 10.1029/2008jg000689.

Schmidt, G. A., G. Hoffmann, D. T. Shindell, and Y. Y. Hu (2005), Modeling Atmospheric Stable Water Isotopes and the Potential for Constraining Cloud Processes and Stratosphere-Troposphere Water Exchange, *Journal of Geophysical Research-Atmospheres*, *110*(D21), D21314, doi: 10.1029/2005jd005790.

Schmidt, G. A., R. Ruedy, J. E. Hansen, I. Aleinov, N. Bell, M. Bauer, S. Bauer, B. Cairns, V. Canuto, Y. Cheng, A. Del Genio, G. Faluvegi, A. D. Friend, T. M. Hall, Y. Y. Hu, M. Kelley, N. Y. Kiang, D. Koch, A. A. Lacis, J. Lerner, K. K. Lo, R. L. Miller, L. Nazarenko, V. Oinas, J. Perlwitz, J. Perlwitz, D. Rind, A. Romanou, G. L. Russell, M. Sato, D. T. Shindell, P. H. Stone, S. Sun, N. Tausnev, D. Thresher, and M. S. Yao (2006),

Present-Day Atmospheric Simulations Using GISS ModelE: Comparison to in Situ, Satellite, and Reanalysis Data, *Journal of Climate*, *19*(2), 153-192.

Schmidt, G. A., A. N. LeGrande, and G. Hoffmann (2007), Water isotope expressions of intrinsic and forced variability in a coupled ocean-atmosphere model, *Journal of Geophysical Research-Atmospheres*, *112*(D10), D10103,:10.1029/2006jd007781.

Scholl, M. A., J. B. Shanley, J. P. Zegarra, and T. B. Coplen (2009), The stable isotope amount effect: New insights from NEXRAD echo tops, Luquillo Mountains, Puerto Rico, *Water Resources Research*, *45*, Artn W12407, Doi 10.1029/2008wr007515.

Sharp, Z. (2007), *Principles of Stable Isotope Geochemistry*, 344 pp., Pearson Prentice Hall, Upper Saddle River, New Jersey, USA.

Sherwood, S. C., R. Roca, T. M. Weckwerth, and N. G. Andronova (2010), Tropospheric Water Vapor, Convection, and Climate, *Reviews of Geophysics*, *48*, Artn Rg2001, Doi 10.1029/2009rg000301.

Shindell, D. T., G. A. Schmidt, M. E. Mann, D. Rind, and A. Waple (2001), Solar Forcing of Regional Climate Change During the Maunder Minimum, *Science*, *294*(5549), 2149-2152.

Shuman, C. A., D. H. Bromwich, J. Kipfstuhl, and M. Schwager (2001), Multiyear Accumulation and Temperature History Near the North Greenland Ice Core Project Site, North Central Greenland, *Journal of Geophysical Research-Atmospheres*, *106*(D24), 33853-33866.

Smol, J. P., A. P. Wolfe, H. J. B. Birks, M. S. V. Douglas, V. J. Jones, A. Korhola, R. Pienitz, K. Ruhland, S. Sorvari, D. Antoniades, S. J. Brooks, M. A. Fallu, M. Hughes, B. E. Keatley, T. E. Laing, N. Michelutti, L. Nazarova, M. Nyman, A. M. Paterson, B. Perren, R. Quinlan, M. Rautio, E. Saulnier-Talbot, S. Siitoneni, N. Solovieva, and J. Weckstrom (2005), Climate-Driven Regime Shifts in the Biological Communities of Arctic Lakes, *Proceedings of the National Academy of Sciences of the United States of America*, *102*(12), 4397-4402.

Sodemann, H., V. Masson-Delmotte, C. Schwierz, B. M. Vinther, and H. Wernli (2008), Interannual variability of Greenland winter precipitation sources: 2. Effects of North Atlantic Oscillation variability on stable isotopes in precipitation, *Journal of Geophysical Research-Atmospheres*, *113*(D12), D12111,:10.1029/2007jd009416.

Sonntag, C., and H. Schoch-Fischer (1985), Deuterium and Oxygen 18 in Water Vapor and Precipitation: Application to Atmospheric Water Vapor Transport and to Paleoclimate, *Isotopes in Environmental and Health Studies*, *21*(6), 193-198.

Steinwagner, J., M. Milz, T. von Clarmann, N. Glatthor, U. Grabowski, M. Hopfner, G. P. Stiller, and T. Rockmann (2007), HDO measurements with MIPAS, *Atmospheric Chemistry and Physics*, *7*(10), 2601-2615.

Stern, L. A., and P. M. Blisniuk (2002), Stable isotope composition of precipitation across the southern Patagonian Andes, *Journal of Geophysical Research-Atmospheres*, *107*(D23), 4667, doi:10.1029/2002jd002509.

Stewart, M. K. (1975), Stable Isotope Fractionation Due to Evaporation and Isotopic-Exchange of Falling Waterdrops - Applications to Atmospheric Processes and Evaporation of Lakes, *Journal of Geophysical Research*, *80*(9), 1133-1146.

Strong, M., Z. D. Sharp, and D. S. Gutzler (2007), Diagnosing moisture transport using D/H ratios of water vapor, *Geophysical Research Letters*, *34*(3), L03404,doi :10.1029/2006gl028307.

Sturm, C., Q. Zhang, and D. Noone (2010), An introduction to stable water isotopes in climate models: benefits of forward proxy modelling for paleoclimatology, *Climate of the Past*, *6*(1), 115-129.

Sturm, K., G. Hoffmann, B. Langmann, and W. Stichler (2005), Simulation of Delta O-18 in Precipitation by the Regional Circulation Model REMOiso, *Hydrological Processes*, *19*(17), 3425-3444.

Sundqvist, H. (1978), Parameterization Scheme for Non-Convective Condensation Including Prediction of Cloud Water-Content, *Quarterly Journal of the Royal Meteorological Society*, *104*(441), 677-690.

Thompson, D. W. J., and J. M. Wallace (1998), The Arctic Oscillation Signature in the Wintertime Geopotential Height and Temperature Fields, *Geophysical Research Letters*, *25*(9), 1297-1300.

Thompson, D. W. J., S. Lee, and M. P. Baldwin (2003), Atmospheric Processes Governing the Northern Hemisphere Annular Mode/ North Atlantic Oscillation, in *The North Atlantic Oscillation: Climatic Signficance and Environmental Impact*, edited by J. W. Hurrell, et al., pp. 81-112, American Geophysical Union, Washington, D.C.

Thompson, L. G., E. Mosleythompson, and B. M. Arnao (1984), El-Nino Southern Oscillation Events Recorded in the Stratigraphy of the Tropical Quelccaya Ice Cap, Peru, *Science*, *226*(4670), 50-53.

Thompson, L. G., E. Mosleythompson, M. E. Davis, J. F. Bolzan, J. Dai, T. Yao, N. Gundestrup, X. Wu, L. Klein, and Z. Xie (1989), Holocene Late Pleistocene Climatic Ice Core Records from Qinghai-Tibetan Plateau, *Science*, *246*(4929), 474-477.

Tian, L., V. Masson-Delmotte, M. Stievenard, T. Yao, and J. Jouzel (2001), Tibetan Plateau Summer Monsoon Northward Extent Revealed by Measurements of Water Stable Isotopes, *Journal of Geophysical Research-Atmospheres*, *106*(D22), 28081-28088.

Tian, L., T. Yao, P. F. Schuster, J. W. C. White, K. Ichiyanagi, E. Pendall, J. Pu, and Y. Wu (2003), Oxygen-18 concentrations in recent precipitation and ice cores on the Tibetan

Plateau, *Journal of Geophysical Research-Atmospheres*, *108*(D9), 4293,:10.1029/2002jd002173.

Tian, L. D., T. D. Yao, K. MacClune, J. W. C. White, A. Schilla, B. Vaughn, R. Vachon, and K. Ichiyanagi (2007), Stable isotopic variations in west China: A consideration of moisture sources, *Journal of Geophysical Research-Atmospheres*, *112*(D10), Artn D10112, doi 10.1029/2006jd007718.

Tindall, J. C., P. J. Valdes, and L. C. Sime (2009), Stable water isotopes in HadCM3: Isotopic signature of El Nino Southern Oscillation and the tropical amount effect, *Journal of Geophysical Research-Atmospheres*, *114*, 12, D04111, doi: 10.1029/2008jd010825.

Trenberth, K. E., and D. A. Paolino (1980), The Northern Hemisphere Sea-Level Pressure Data Set - Trends, Errors and Discontinuities, *Monthly Weather Review*, *108*(7), 855-872.

Trenberth, K. E., and J. W. Hurrell (1994), Decadal Atmosphere-Ocean Variations in the Pacific, *Climate Dynamics*, *9*(6), 303-319.

Treydte, K., D. Frank, J. Esper, L. Andreu, Z. Bednarz, F. Berninger, T. Boettger, C. M. D'Alessandro, N. Etien, M. Filot, M. Grabner, M. T. Guillemin, E. Gutierrez, M. Haupt, G. Helle, E. Hilasvuori, H. Jungner, M. Kalela-Brundin, M. Krapiec, M. Leuenberger, N. J. Loader, V. Masson-Delmotte, A. Pazdur, S. Pawelczyk, M. Pierre, O. Planells, R. Pukiene, C. E. Reynolds-Henne, K. T. Rinne, A. Saracino, M. Saurer, E. Sonninen, M. Stievenard, V. R. Switsur, M. Szczepanek, E. Szychowska-Krapiec, L. Todaro, J. S. Waterhouse, M. Weigl, and G. H. Schleser (2007), Signal strength and climate calibration of a European tree-ring isotope network, *Geophysical Research Letters*, *34*(24), Artn L24302, Doi 10.1029/2007gl031106.

Treydte, K. S., G. H. Schleser, G. Helle, D. C. Frank, M. Winiger, G. H. Haug, and J. Esper (2006), The twentieth century was the wettest period in northern Pakistan over the past millennium, *Nature*, *440*(7088), 1179-1182, Doi 10.1038/Nature04743.

Trouet, V., J. Esper, N. E. Graham, A. Baker, J. D. Scourse, and D. C. Frank (2009), Persistent Positive North Atlantic Oscillation Mode Dominated the Medieval Climate Anomaly, *Science*, *324*(5923), 78-80, doi:10.1126/science.1166349.

van Ommen, T. D., and V. Morgan (1997), Calibrating the ice core paleothermometer using seasonality, *Journal of Geophysical Research-Atmospheres*, *102*(D8), 9351-9357.

Vimeux, F., P. Ginot, M. Schwikowski, M. Vuille, G. Hoffmann, L. G. Thompson, and U. Schotterer (2009), Climate variability during the last 1000 years inferred from Andean ice cores: A review of methodology and recent results, *Palaeogeography Palaeoclimatology Palaeoecology*, *281*(3-4), 229-241, DOI 10.1016/j.palaeo.2008.03.054.

Vinther, B. M., S. J. Johnsen, K. K. Andersen, H. B. Clausen, and A. W. Hansen (2003), NAO signal recorded in the stable isotopes of Greenland ice cores, *Geophysical Research Letters*, *30*(7), 1387, doi: 10.1029/2002gl016193.

Vuille, M., R. S. Bradley, R. Healy, M. Werner, D. R. Hardy, L. G. Thompson, and F. Keimig (2003a), Modeling delta O-18 in precipitation over the tropical Americas: 2. Simulation of the stable isotope signal in Andean ice cores, *Journal of Geophysical Research-Atmospheres*, *108*(D6), Artn 4175, doi 10.1029/2001jd002039.

Vuille, M., R. S. Bradley, M. Werner, R. Healy, and F. Keimig (2003b), Modeling delta O-18 in precipitation over the tropical Americas: 1. Interannual variability and climatic controls, *Journal of Geophysical Research-Atmospheres*, *108*(D6), 4174, doi:10.1029/2001jd002038.

Vuille, M., and M. Werner (2005), Stable isotopes in precipitation recording South American summer monsoon and ENSO variability: observations and model results, *Climate Dynamics*, *25*(4), 401-413, doi: 10.1007/s00382-005-0049-9.

Vuille, M., M. Werner, R. S. Bradley, R. Y. Chan, and F. Keimig (2005a), Stable Isotopes in East African Precipitation Record Indian Ocean Zonal Mode, *Geophysical Research Letters*, *32*(21).

Vuille, M., M. Werner, R. S. Bradley, and F. Keimig (2005b), Stable isotopes in precipitation in the Asian monsoon region, *Journal of Geophysical Research-Atmospheres*, *110*(D23), D23108, doi: 10.1029/2005jd006022.

Wallace, J. M., and D. S. Gutzler (1981), Teleconnections in the Geopotential Height Field During the Northern Hemisphere Winter, *Monthly Weather Review*, *109*(4), 784-812.

Wallace, J. M. (2000), North Atlantic Oscillation/annular mode: Two paradigms - one phenomenon, *Quarterly Journal of the Royal Meteorological Society*, *126*(564), 791-805.

Wang, Y. J., H. Cheng, R. L. Edwards, Z. S. An, J. Y. Wu, C. C. Shen, and J. A. Dorale (2001), A high-resolution absolute-dated Late Pleistocene monsoon record from Hulu Cave, China, *Science*, *294*(5550), 2345-2348.

Werner, M., U. Mikolajewicz, M. Heimann, and G. Hoffmann (2000), Borehole Versus Isotope Temperatures on Greenland: Seasonality Does Matter, *Geophysical Research Letters*, *27*(5), 723-726.

Werner, M., M. Heimann, and G. Hoffmann (2001), Isotopic Composition and Origin of Polar Precipitation in Present and Glacial Climate Simulations, *Tellus Series B-Chemical and Physical Meteorology*, *53*(1), 53-71.

Werner, M., and M. Heimann (2002), Modeling interannual variability of water isotopes in Greenland and Antarctica, *Journal of Geophysical Research-Atmospheres*, *107*(D1-D2), 4001, doi: 10.1029/2001jd900253.

White, J. W. C., L. K. Barlow, D. Fisher, P. Grootes, J. Jouzel, S. J. Johnsen, M. Stuiver, and H. Clausen (1997), The climate signal in the stable isotopes of snow from Summit, Greenland: Results of comparisons with modern climate observations, *Journal of Geophysical Research-Oceans*, *102*(C12), 26425-26439.

Wiles, G. C., R. D. D'Arrigo, R. Villalba, P. E. Calkin, and D. J. Barclay (2004), Century-scale solar variability and Alaskan temperature change over the past millennium, *Geophysical Research Letters*, *31*(15).

Wilson, R., G. Wiles, R. D'arrigo, and C. Zweck (2007), Cycles and shifts: 1,300 years of multi-decadal temperature variability in the Gulf of Alaska, *Climate Dynamics*, *28*(4), 425-440.

Worden, J., K. Bowman, D. Noone, R. Beer, S. Clough, A. Eldering, B. Fisher, A. Goldman, M. Gunson, R. Herman, S. S. Kulawik, M. Lampel, M. Luo, G. Osterman, C. Rinsland, C. Rodgers, S. Sander, M. Shephard, and H. Worden (2006), Tropospheric emission spectrometer observations of the tropospheric HDO/H2O ratio: Estimation approach and characterization, *Journal of Geophysical Research-Atmospheres*, *111*(D16), D16309, doi: 10.1029/2005jd006606.

Worden, J., D. Noone, and K. Bowman (2007), Importance of Rain Evaporation and Continental Convection in the Tropical Water Cycle, *Nature*, *445*(7127), 528-532.

Wright, J. S., A. H. Sobel, and G. A. Schmidt (2009), Influence of condensate evaporation on water vapor and its stable isotopes in a GCM, *Geophysical Research Letters*, *36*, L12804, doi 10.1029/2009gl038091.

Yamanaka, T., J. Shimada, Y. Hamada, T. Tanaka, Y. H. Yang, W. J. Zhang, and C. S. Hu (2004), Hydrogen and Oxygen Isotopes in Precipitation in the Northern Part of the North China Plain: Climatology and Inter-Storm Variability, *Hydrological Processes*, *18*(12), 2211-2222.

Yamanaka, T., M. Tsujimura, D. Oyunbaatar, and G. Davaa (2007), Isotopic variation of precipitation over eastern Mongolia and its implication for the atmospheric water cycle, *Journal of Hydrology*, *333*(1), 21-34, doi:10.1016/j.jhydrol.2006.07.022.

Yoshimura, K., M. Kanamitsu, D. Noone, and T. Oki (2008), Historical isotope simulation using Reanalysis atmospheric data, *Journal of Geophysical Research-Atmospheres*, *113*(D19), D19108, doi:10.1029/2008jd010074.

Yu, W., T. Yao, L. Tian, Y. Ma, N. Kurita, K. Ichiyanagi, Y. Wang, and W. Sun (2007), Stable isotope variations in precipitation and moisture trajectories on the western Tibetan plateau, China, *Arctic Antarctic and Alpine Research*, *39*(4), 688-693.

Zhu, X. J., J. L. K. Sun, Z. Y. Liu, Q. Y. Liu, and J. E. Martin (2007), A Synoptic Analysis of the Interannual Variability of Winter Cyclone Activity in the Aleutian Low Region, *Journal of Climate*, *20*(8), 1523-1538.

Zimmerman, U., D. Ehhalt, and K. O. Munnich (1967), Soil-water Movement and Evapotranspiration: Changes in the Isotopic Composition of the Water, paper presented at Isotopes in Hydrology: Proceedings of a Symposium, International Atomic Energy Agency, Vienna, Australia.